



1-1-2014

A Comparison Of Solar Prominence Data Between H α And EUV (he II-304Å)

Jonathan Schiralli

[How does access to this work benefit you? Let us know!](#)

Follow this and additional works at: <https://commons.und.edu/theses>

Recommended Citation

Schiralli, Jonathan, "A Comparison Of Solar Prominence Data Between H α And EUV (he II-304Å)" (2014).
Theses and Dissertations. 1592.
<https://commons.und.edu/theses/1592>

This Thesis is brought to you for free and open access by the Theses, Dissertations, and Senior Projects at UND Scholarly Commons. It has been accepted for inclusion in Theses and Dissertations by an authorized administrator of UND Scholarly Commons. For more information, please contact und.commons@library.und.edu.

A COMPARISON OF SOLAR PROMINENCE DATA BETWEEN
 $H\alpha$ AND EUV (He II-304Å)

by

Jonathan Luke Schiralli
Master of Science, University of North Dakota, 2014

A Thesis
Submitted to the Graduate Faculty
of the
University of North Dakota
in partial fulfillment of the requirements

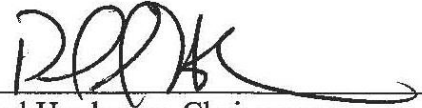
for the degree of

Master of Science

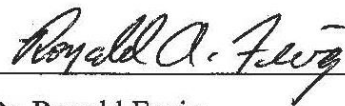
Grand Forks, North Dakota
May
2014

Copyright 2014 Jonathan Schiralli

This thesis, submitted by Jonathan L. Schiralli in partial fulfillment of the requirements for the Degree of Master of Science from the University of North Dakota, has been read by the Faculty Advisory Committee under whom the work has been done and is hereby approved.



Dr. Paul Hardersen, Chairperson

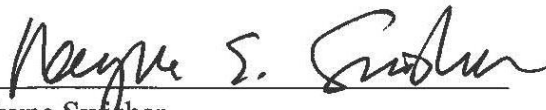


Dr. Ronald Fevig,

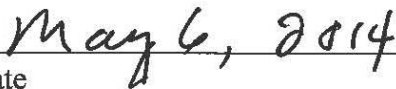


Dr. Wayne Barkhouse,

This thesis is being submitted by the appointed advisory committee as having met all of the requirements of the School of Graduate Studies at the University of North Dakota and is hereby approved.



Wayne Swisher
Dean, School of Graduate Studies



Date

PERMISSION

Title A comparison of solar prominence data between H α and EUV (He II-304Å)

Department Space Studies

Degree Master of Science

In presenting this thesis in partial fulfillment of the requirements for a graduate degree from the University of North Dakota, I agree that the library of this University shall make it freely available for inspection. I further agree that permission for extensive copying for scholarly purposes may be granted by the professor who supervised my thesis work or, in their absence, by the chairperson of the department or the dean of the School of Graduate Studies. It is understood that any copying or publication or other use of this thesis or part thereof for financial gain shall not be allowed without my written permission. It is also understood that due recognition shall be given to me and to the University of North Dakota in any scholarly use which may be made of any material in my thesis.

Name: Jonathan Luke Schiralli

Date: 05/05/2014

TABLE OF CONTENTS

LIST OF FIGURES	viii
LIST OF TABLES	x
ACKNOWLEDGEMENTS	xi
ABSTRACT	xii
I. INTRODUCTION	1
Solar Magnetism	2
The Electromagnetic Spectrum.....	4
Photosphere Features	5
Chromosphere Features	5
Solar Flares, CMEs, Sigmoids and Prominences/ Filaments.....	10
Prominence Background.....	15
Quiescent and Active Region Prominences/Filaments	16
Structure of Prominences/ Filaments	18
Filament Channels	22
Chirality Relationships.....	26
Magnetic Reconnection	31
Flux Cancellation and Counterstreaming.....	33
Disparition-Brusque and CMEs.....	35
Models of Magnetic Field Configurations.....	36

Dip Model	36
Flux Rope Model	38
Wire Model	41
Models of Prominence Mass Accumulation	43
Coronal Condensation / Levitation Model.....	46
Injection Model	49
Evaporation-Condensation /Thermal Non-Equilibrium Model	51
Prominence/ Filament Eruption	53
Some Open Issues for Future Research	55
II. METHODOLOGY	57
Purpose.....	57
Hypothesis.....	58
Observations	58
The Dutch Open Telescope	59
Cameras.....	60
DOT Data.....	60
Solar Dynamic Observatory.....	61
Calculating the dimensions of a prominence	62
Calculating the speed of mass motions	63
III. RESULTS	65
Northeast Prominence (N53E90).....	65

DOT's H α NE Prominence Analysis	66
SDO's 304Å NE Prominence Analysis.....	68
First Event- Plasma dip.....	72
Second Event- NW mass of plasma.....	74
Third Event - Curl.....	76
The North West Prominence N33W90	78
DOT H α NW Prominence.....	78
The Shape of SDO's 304Å NW Prominence.....	80
Dimensions of SDO's 304Å NW Prominence.....	84
The Evolution of the NW Prominence.....	86
 IV. DISCUSSION AND CONCLUSION	 97
Classifying prominences	97
H α vs He II 304 Å.....	101
Conclusion	104
 REFERENCES	 106

LIST OF FIGURES

Figure	Page
1. Radiative and Convection zone.	2
2. Magnetic Field Lines.	3
3. Solar Spectrum.....	4
4. Eclipse and Corona.	6
5. Helmet Streamer.....	6
6. Coronal Hole and EUV.	7
7. Polar Plumes.	8
8. Coronal Arcade	8
9. A CME Eruption	10
10. Post Flare Loop System	11
11. Soft-X-ray Sigmoids	12
12. EUV vs $H\alpha$	13
13. Prominence over the limb	14
14. $H\alpha$ filament	18
15. High resolution $H\alpha$ spine with barbs	20
16. Prominences in different wavelengths.	21
17. Filament channel with fibrils	22
18. Chirality of a filament channel	24
19. Fibrils and chirality.....	25
20. One-to-one chirality.	27
21. A Chiral System	28
22. Model of the formation of a prominence.	30
23. The build-up to Eruptive Solar Events.....	31
24. 2D model of magnetic reconnection	33
25. Prominence magnetic field structure.	36
26. Magnetic field models to support a prominence.....	38
27. Flux Rope.....	40
28. Formation of a prominence in a twisted flux rope.....	40
29. Geometry of the magnetic field of a filament.....	42
30. Martin and Echols model.	43
31. S-shaped filament.....	44
32. 3D model for the formation of filaments	44
33. Levitation of prominence plasma.....	47
34. Injection of prominence plasma.....	50

35. Evaporation-condensation model.....	52
36. Dutch Open Telescope on La Palma	59
37. How to estimate speed.	64
38. North East Prominence.	65
39. DOT NE prominence dimensions	66
40. Three directions of NE prominence	68
41. SDO dimensions of the NE prominence as seen in 304Å	69
42. NE prominence H α image overlaid 304Å.....	69
43. SDO prominence appearing on the disk.	70
44. Event paths of the NE prominence.	71
45. NE prominence event 1 H α	73
46. Mass traveled in event 1	74
47. Event 2 mass- NE prominence.....	75
48. Event 3 curl- NE prominence.	77
49. North West Prominence	78
50. DOT NW prominence dimensions.....	79
51. DOT H α speeds.....	80
52. NW prominence in 304Å at 16.42 UT.	81
53. Movement of the NW prominence	82
54. Movement of the NW prominence over time.	83
55. NW prominence dimensions in 304 Å.....	84
56. NW prominence speeds	85
57. NW prominence at the start	86
58. NW prominence H α split.	87
59. Appearance of the west prominence in the NW.....	88
60. Blue shift moving material in H α	89
61. Speeds calculated in 304Å.....	90
62. Bridge connection between pillar and west prominence.	91
63. Plasma eruption from flowing collision.....	92
64. Plasma eruption from flowing collision in H α	93
65. Eruption stops plasma flow to active region.....	94
66. Eruption speeds.....	95
67. Dip seen in in the West Prominence Formation.....	99
68. H α vs 304Å sizes NE & NW	102
69. H α vs 304Å structure comparison.	103

LIST OF TABLES

Table	Page
1. Velocity Calculations	96

ACKNOWLEDGEMENTS

I wish to express my sincere appreciation to the members of my advisory committee for their guidance and support during my time in the Space Studies master's program at the University of North Dakota. I would also like to express my gratitude to Sara Martin of Helio Research Inc. who supplied the necessary data needed for this study.

ABSTRACT

Two spectral lines are often used to observe solar prominences: $H\alpha$ and He II 304Å. Both emission lines capture the same prominence structure but at vastly different temperatures: $H\alpha$ is visible at $\sim 10,000\text{K}$ while He II 304Å at $\sim 80,000\text{K}$. The He II 304Å images provide the ability to identify the relatively hotter outer region of a prominence, although they lack the details seen in the cooler lower regions. $H\alpha$ conversely shows great detail in the cooler lower regions of a prominence but lack any detail in the hotter outer region of a prominence. Two prominences will be the subject of this paper, a low lying prominence on the northeast limb of the Sun and a larger prominence near an active region on the northwest limb of the Sun. Analysis of simultaneous images of prominences using the SDO's Atmospheric Imaging Assembly (AIA) at the He II 304Å wavelength and the Dutch Open Telescope (DOT) $H\alpha$ wavelength reveal both similar and different morphology. The challenge when comparing observations from both systems is to obtain sufficient congruence to determine the prominence properties and structure.

$H\alpha$ images tend to show the cooler core of a prominence and detail in the finer structure. 304 Å images show much more detail in the terms of higher hotter material which gives a greater sense to the structure and life of a prominence. By studying both wavelengths a more complete picture of the properties, structure and the evolution of a prominence can be learned.

CHAPTER I

INTRODUCTION

Prominence eruptions are phenomena that are caused by an instability during the evolution of magnetic lines in the solar atmosphere that expel material from the corona into the solar system. Prominences are dense clouds of relatively cool (chromospheric temperature) gas suspended above the surface of the Sun by loops of magnetic field lines that overlie a neutral line (i.e., PIL, the magnetic polarity inversion line) of an active (dynamic) region and are embedded in the much hotter coronal plasma (Aschwaden, 2006). On the solar disk, these cool dense features appear dark against the bright background, and are called filaments while the same structures appear bright above the limb where they are called prominences. Therefore, filaments and prominences are the same structures physically; their name just reflects from where they are observed - inside or outside the solar disk (Aschwaden 2006). Quiescent (quiet/inactive/static) filaments/prominences are long-lived stable structures that can last for several months, while active eruptive filaments/prominences are usually associated with flares and coronal mass ejections (CMEs) which can greatly affect Earth's space weather (Kilper, 2009, Aschwanden, 2006).

Filaments/prominences are large regions of very dense, cool gas, supported against gravity and held in place by magnetic fields. The material is surrounded by a void with an overarching arcade. Studies of prominences show the eruption process in many wavelengths (i.e., over a wide range of temperatures) and has resulted in the proposal of

several models of the formation and the initiation of the eruption of prominences (Rust and Kumar, 1994, Antiochos & Klimchuk 2000, Aulanier 2006, Martin 2012). How prominences form, how they are sustained in the corona and what causes them to erupt however is still unclear. Many theories and models have been proposed but the answers to these questions continue to be a mystery.

Solar Magnetism

All solar activity, including the formation of prominences, is a result of magnetism. The Sun is approximately three quarters hydrogen, with the rest being mostly helium and is composed of plasma, i.e. ionized gas (Aschwanden 2006). Because the Sun is not solid, but is plasma, the equatorial regions rotate faster than the Polar Regions causing differential rotation. The line (tacholine) between the radiative zone and the convection zone is where the uniform rotation of the radiative zone and the differential rotation of the convection zone connect resulting in a large shear, where each of the layers slide past one another. This magnetic dynamo located at the base of the convection zone, generates magnetic fields by rotating, convecting (transferring heat in a circulatory movement) and electrically conducting plasma at the tacholine, Figure 1 depicts the radiative and convection zones.

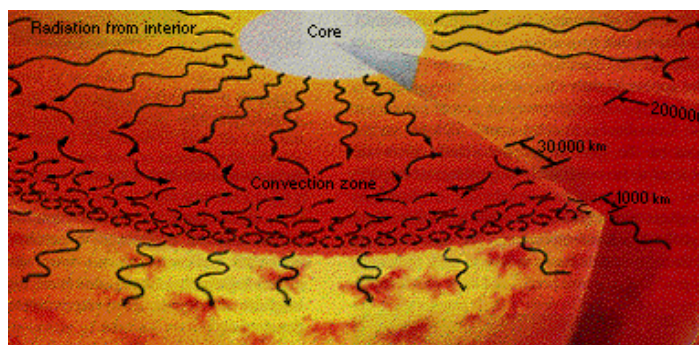


Figure 1: The tacholine is between the radiative and convective zones, this is where large shear occurs due to differential rotation (Chaisson, 1993).

The differential rotation stretches the magnetic fields winding and twisting into a toroidal field of "flux ropes" that become wrapped around the Sun. Magnetic flux refers to the magnitude of force passing perpendicularly through a specified area in a magnetic field; these series of loops as shown in Figure 2 are known as flux ropes.

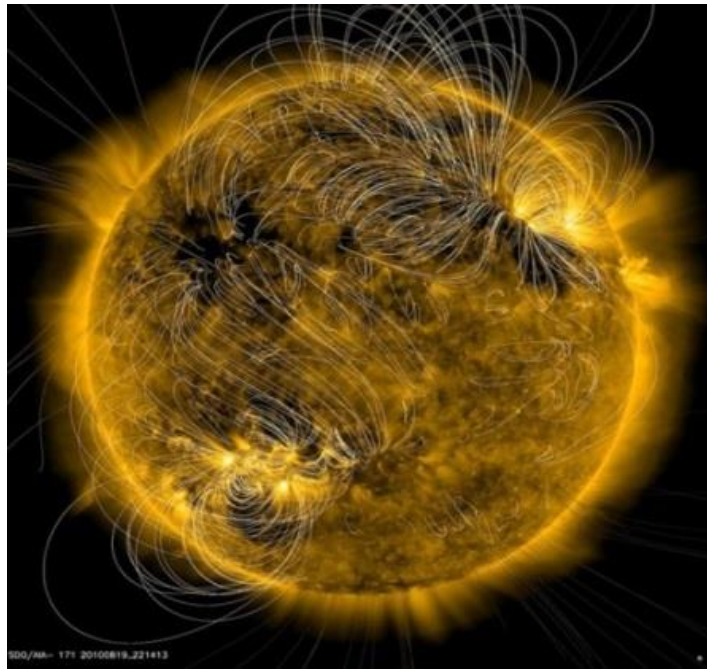


Figure 2: Magnetic field lines are seen as loops which represents the emerging flux ropes on the Sun, on August 20, 2010 (National Aeronautics and Space Administration, n.d.).

Magnetic field lines loop through the solar atmosphere and interior to form complex magnetic structures, including prominences. The prominences seen above the surface of the Sun are supported by these magnetic fields (Ballegooijen, 1989). The solar magnetic cycle is about 11 years, at which time the magnetic polarity of the global solar magnetic field reverses. A full cycle is 22 years. During a cycle, the active regions migrate from high latitudes towards lower latitudes near the equator (Babcock, 1961). During solar minimum the Sun's magnetic field has closed loops near the equator and open field lines near the poles. At solar maximum sunspots activity increases and the magnetic field begins to

change. Meridional flows, the flow of flux along meridian lines from the equator toward the poles at the surface and from the poles to the equator below the surface, affects the magnetic dynamo (Aschwanden, 2006). This oppositely directed flux grows at the Sun's poles until at solar maximum when the magnetic poles reverse polarity causing the magnetic field lines to flow in a new direction.

The Electromagnetic Spectrum

When the Sun is viewed through a spectrograph, it disperses light into a spectrum so that the intensity at different wavelengths can be measured by a detector which isolates the emission. The chromosphere is visible in the light emitted by ionized calcium, Ca II, in the violet part of the electromagnetic spectrum at the Ca II K-line and the Ca II H-line. H-alpha ($H\alpha$) is a specific spectral line visible in the red part of the electromagnetic spectrum which describes the spectral line emissions of neutral hydrogen with a wavelength of 656.28 nm. Observing prominences in the chromosphere is via $H\alpha$ and Ca II narrow band observations. Observing prominences in the corona requires extreme ultraviolet (EUV) observations only available from spacecraft that go beyond Earth's atmosphere. Figure 3 is an illustration of the solar spectrum with the absorption lines (Fraunhofer lines) marked.

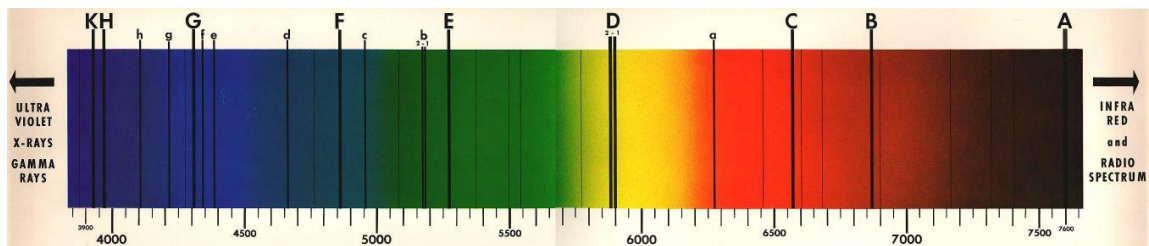


Figure 3: This figure represents the solar spectrum with Fraunhofer lines C = $H\alpha$, G = Ca, H = Ca I, and K = Ca II marked in their absorption lines. Source: <http://www.harmsy.freeuk.com/images/spectrum.jpeg>

Photosphere Features

The photosphere is the visible surface of the Sun and the location of sunspots which appear as dark areas on the surface lasting for a few days to several weeks. They appear in groups with two sets of spots; one set will have positive or north magnetic field and the other set will have a negative or south magnetic field (Aschwanden, 2006). Because of the bipolar set up (pair of equal and oppositely charged magnetized poles separated by a distance) active regions are mainly made up of closed magnetic field lines. There are two types of magnetic field lines: closed field lines that start in the solar interior, emerge from the surface and end in the solar interior, and open field lines which start at the solar surface and end in interplanetary space (Aschwanden, 2006). Quiet regions or quiet Sun have minimum solar activity and include all closed magnetic field regions, excluding the active regions and the open magnetic field regions.

Chromosphere Features

The chromosphere is a layer of the sun just above the photosphere and just below the transition region. The transition region is a thin layer that separates the hot corona from the much cooler chromosphere. Heat flows down from the corona into the chromosphere and in the process produces a transition region where the temperature changes rapidly from 1,000,000 K down to about 20,000 K (Aschwanden, 2006). The corona is the Sun's outermost layer and has temperatures greater than 1,000,000 K. It is only visible during eclipses, or by an orbiting spacecraft through specialized instruments, and appears as a pearly white crown surrounding the Sun (National Aeronautics and Space Administration, n.d.). Figure 4 is a Soft X-ray image of the extended solar corona recorded on 1992 August 26 by the Yohkoh Soft X-ray Telescope (SXT).

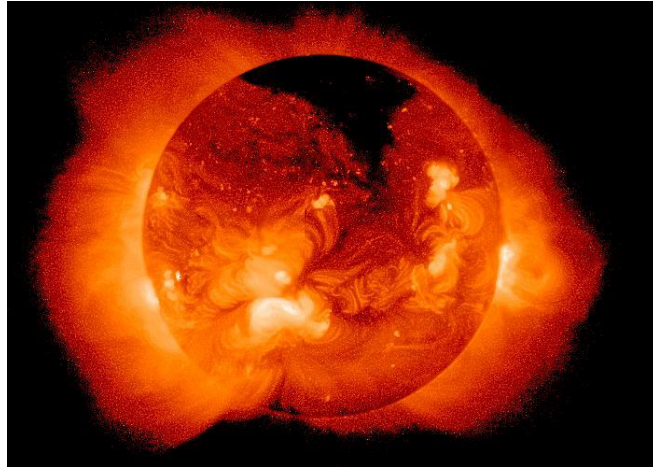


Figure 4: This image shows the corona shining brightly in x-rays due to the extremely high temperatures. Image credit: National Aeronautics and Space Administration, n.d.

Helmet streamers, polar plumes, coronal loops, and coronal holes can be seen using extreme ultraviolet images (EUV), which detect emitted radiation at wavelengths from 124 nm down to 10 nm from the Sun. Helmet streamers are connected with active regions and are centered over prominences. The lower part contains closed field lines while the upper part turns into a cusp-shaped formation, giving the appearance of a “helmet” (Aschwanden, 2006). Figure 5 is an image of a Helmet streamer.



Figure 5: A helmet streamer usually overlies an active region and prominences are usually found at the base. Image credit: National Aeronautics Space Administration, n.d.

Coronal holes were discovered to be the source of the high speed solar wind (Krieger et al., 1973) and data from Skylab and OSO-7 data confirmed that the open field coronal holes are the source of high speed wind streams (Bhatnager & Livingston 2005). Coronal holes were discovered in EUV and X-ray images taken from spacecraft (National Aeronautics and Space Administration, n.d.). Coronal holes are often located near the Sun's poles and are associated with open magnetic field lines (National Aeronautics and Space Administration, n.d.). Because of this, coronal holes are empty of plasma most of the time and appear much darker than the areas where heated plasma flows up from the chromosphere (Ashwanden, 2006). Figure 6a and Figure 6b are images of coronal holes.

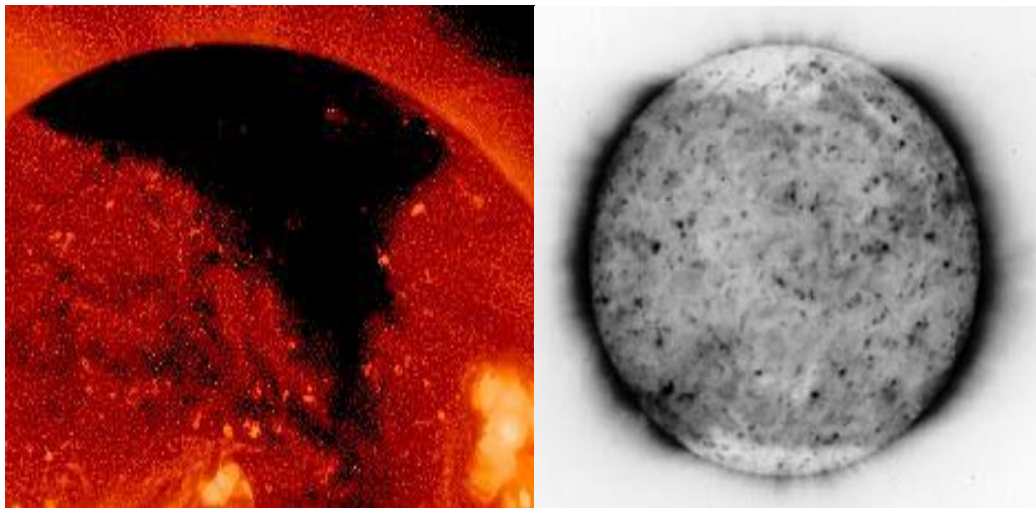


Figure 6: 6a: The left image is of a Coronal Hole taken by an x-ray telescope flown above the earth's atmosphere. 6b: The right image is an EUV image during a solar minimum, the black color indicates enhanced emissions demonstrating the coronal holes in the polar regions. Image credit: Aschwanden, 2006.

Polar plumes are long thin streamers that flow outward from the Sun's north and south poles and are also associated with the open magnetic field lines at the Sun's poles.

Figure 7 is an image of polar plumes.

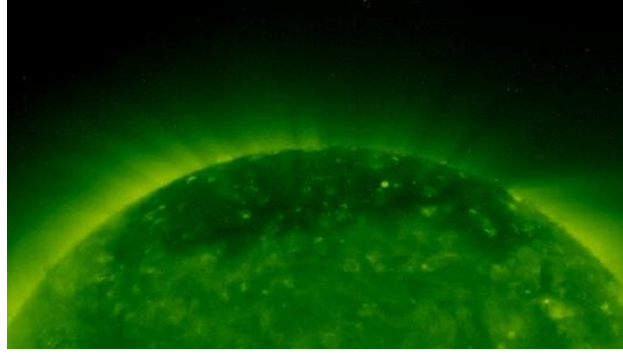


Figure 7: Polar plumes over the south pole of the Sun. Image credit: Aschwanden, 2006.

Coronal loops, seen in Figure 8, contain clouds of gas held in consecutive magnetic field loops which look like an arcade and are filled with denser material than their surroundings (Aschwanden, 2006). Regions of opposite magnetic fields have bipolar loops lined up perpendicular to a neutral line over a large distance, with each of their footpoints (ends of the magnetic field lines) anchored in each side of opposite magnetic polarity along the neutral line.

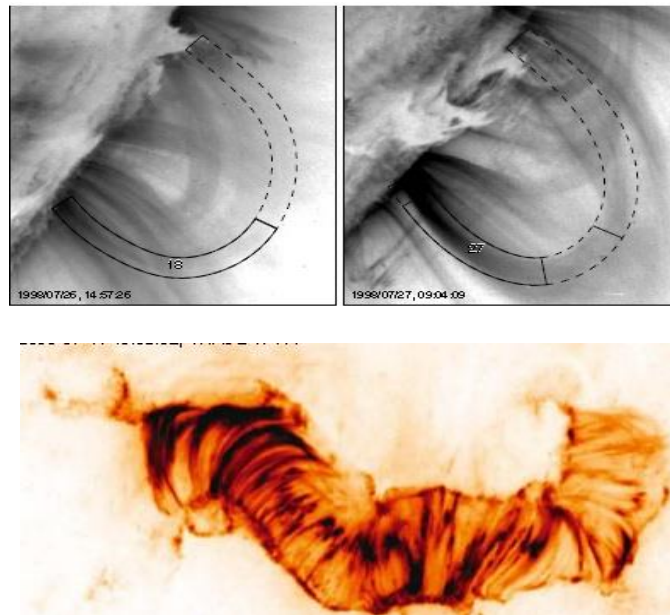


Figure 8: a and b, show coronal loops outlined by dashes. Figure 8c bottom row, shows a long arcade of coronal loops. Image credit: Aschwanden, 2006.

The formation of coronal loops consists of two steps according to Ashwanden (2006): (1) the emergence of a buoyant subphotospheric magnetic flux tubes into the corona, which forms a bipolar magnetic field structure; and (2) filling of coronal flux tubes with heated plasma, which increases the density (and emission measurement) of coronal loops. Coronal loops are channels filled with heated plasma, shaped by the structure of the closed coronal magnetic field (Ashwanden, 2006). A flux tube is considered to be a tube-like cylindrical region of space containing a magnetic field (Cattaneo et al., 2006). In an ideal flux tube, the magnetic field is entirely confined to a compact region, typically cylindrical in shape, and embedded in a field-free environment (Cattaneo et al., 2006). A flux tube is used to describe magnetic phenomena because the ideal flux tube has a well-defined structure. This means that flux that is inside the flux tube will remain inside, and flux that is outside should not be able to enter the flux tube except through the end-points (Cattaneo et al., 2006).

A coronal cavity is an area darker than its surroundings and the height and width of the cavity are about twice the height of the prominence (Saito & Tandberg-Hanssen, 1973). Coronal cavities, (the shell of the cavity is the coronal arcade), are tunnel-like regions of reduced electron density which enclose prominences/filaments and are aligned with polarity inversion lines (PILs) of the photosphere magnetic field. (Saito & Tandberg-Hanssen, 1973). A polarity inversion line or neutral line is where the magnetic field changes polarity. When observed at the solar limb coronal cavities appear as relatively dark, semicircular or circular regions underneath coronal streamers (Saito & Tandberg-Hanssen, 1973). Figure 9 shows an image of a CME eruption and a quiescent prominence both surrounded by a coronal cavity.

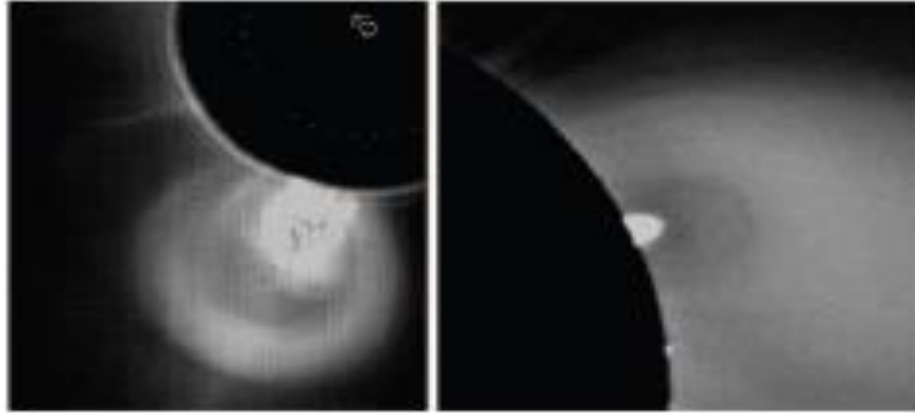


Figure 9: A CME eruption can be seen in the left image and a quiescent prominence and a cavity can be seen in the right image. Image credit: Gibson et al., 2006.

Solar Flares, CMEs, Sigmoids and Prominences/ Filaments

A solar flare is the process where there is a rapid energy release in the solar corona, driven by stored non-potential magnetic energy and triggered by instability in the magnetic configuration (Aschwanden, 2006). Bhatnager & Livingston (2005) defines flares as sudden explosive releases of matter - electromagnetic radiation, energetic particles, wave motions and shockwaves, lasting minutes to hours. They have a quick phase that can last for a few seconds to a minute, followed by a gradual phase lasting for several minutes to hours depending on the intensity of the flare (Bhatnager & Livingston, 2005) Solar flares are extremely hot features, ranging in temperature from 10,000 to several million degrees K (Bhatnager & Livingston, 2005).

Coronal Mass Ejections are huge bubbles of solar plasma filled with magnetic field lines that are ejected from the Sun at high speeds. CME's expel billions of tons of solar plasma in the interplanetary space at millions of degree temperature with speeds ranging from 300-2000 km/s (Bhatnager & Livingston, 2005). It takes about on average 100 hours to reach Earth ejecting masses of 10^{13} kg with a mass flow rate estimated about 2×10^8 kg

per sec. When this large amount of solar plasma hits the Earth, several geomagnetic and terrestrial effects occur disrupting communications and disabling satellite electronics and power grids (Bhatnager & Livingston, 2005). The average frequency of CME's during solar maximum period is about 3.5 events per day, and during minimum about 0.2 events per day; the frequency is correlated with the 11-year solar cycle (Bhatnager & Livingston, 2005).

Flares and CMEs are two examples of major magnetic energy releases which are caused by a common magnetic instability where the magnetic field configuration in an active region becomes stressed or 'sheared' resulting in the built-up of magnetic energy in the corona. An instability like magnetic reconnection in the region, causes the built-up to be suddenly and explosively released at a higher level in the solar atmosphere. (Aschwanden, 2006, Bhatnagen & Livingston, 2005). Figure 10 is an image of a post flare loop system.

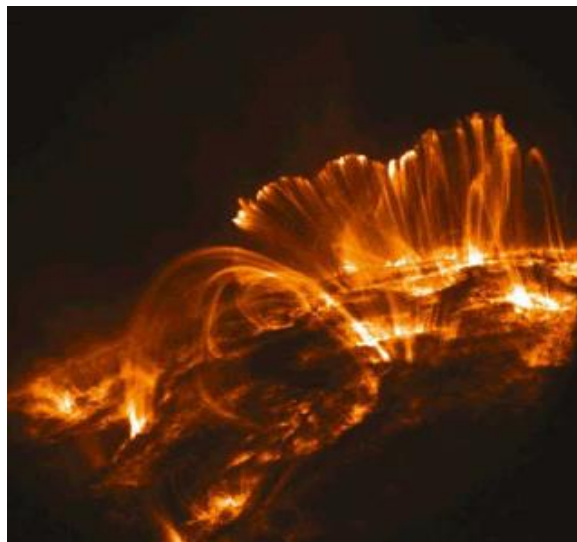


Figure 10: A post flare loop system is imaged with TRACE 171 Å after an eruption. Image credit: National Aeronautics and Space Administration, n.d.

Sigmoids are forward or inverse S-shaped structures seen in the solar corona. Sigmoids that link active regions are more likely to produce flares or CMEs than non-sigmoid active regions and may be precursors of solar eruptions (Canfield et al., 2000). Sigmoids may be magnetic flux ropes embedded in the solar corona (Gibson et al., 2007). They brighten with eruptions and long-duration flares and evolve from a sigmoid to an arcade during an eruption (Rust and Kumar, 1996; Gibson et al., 2007). Sigmoids are often associated with a CME and may become post-flare cusped loops.

Figure 11 shows examples of a variety of sigmoids. Sigmoids are generally observed in soft X-ray emission, but can be visible in UV or EUV (Gibson et al., 2007). Even after CMEs, active regions can show sigmoid structures again in a few hours (Gibson et al., 2007).

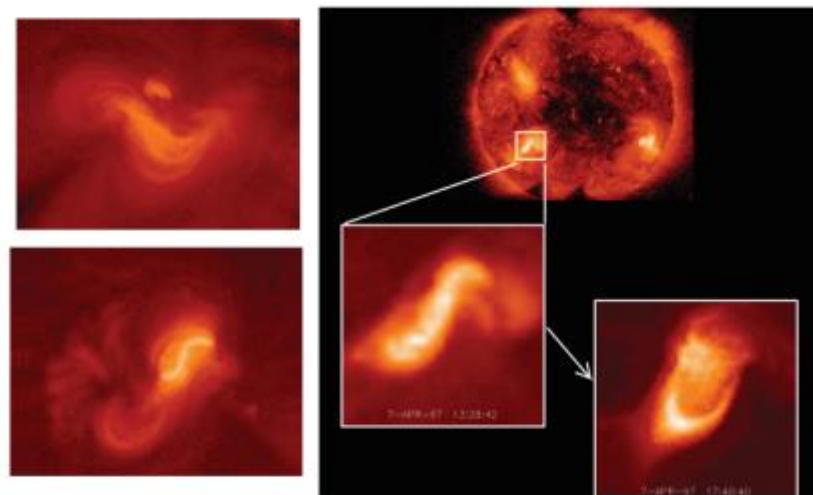


Figure 11: Examples of soft-X-ray sigmoids, as observed by Yohkoh SXT (left top) Persistent sigmoid; (left bottom) transient sigmoid; (right) sigmoid associated with CME, transitioning to cusp. Image credit: Gibson et al., 2007

Prominence eruptions are usually associated with solar flares and CME's but not always. A prominence or filament forms above a magnetic neutral line that builds up

gradually over days and erupts during a flare or CME process (Aschwanden, 2006). They are always located along the neutral line on the photosphere where the magnetic field changes polarity, the polarity inversion line (Mackay, 2010). Figure 12a and b compare images of filaments and prominences seen in $H\alpha$ and EUV.

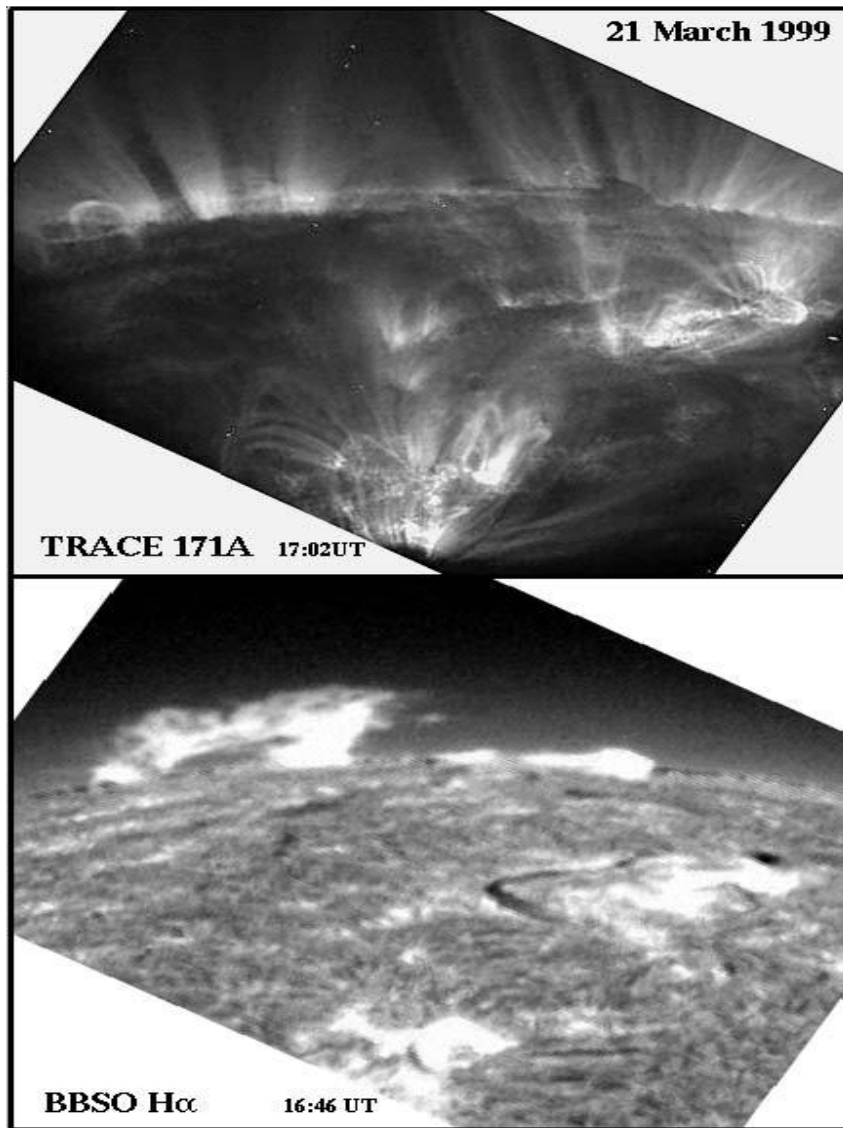


Figure 12: These images compare the corona seen in EUV (top panel: TRACE, 171 Å) and the chromosphere seen in $H\alpha$ (bottom panel: Big Bear Solar Observatory). The prominences show up as bright structures in $H\alpha$ (bottom frame), and as dark, absorbing features in EUV (top frame). Image credit: BBSO & NASA

On the solar disk, the cool dense features appear dark against the bright background of the Sun and are called filaments (See Figure 13b) while the same structures appear bright above the limb, in emission against the dark space background, with a series of looped arcades and a void beneath them; these are called prominences (See Figure 13a).

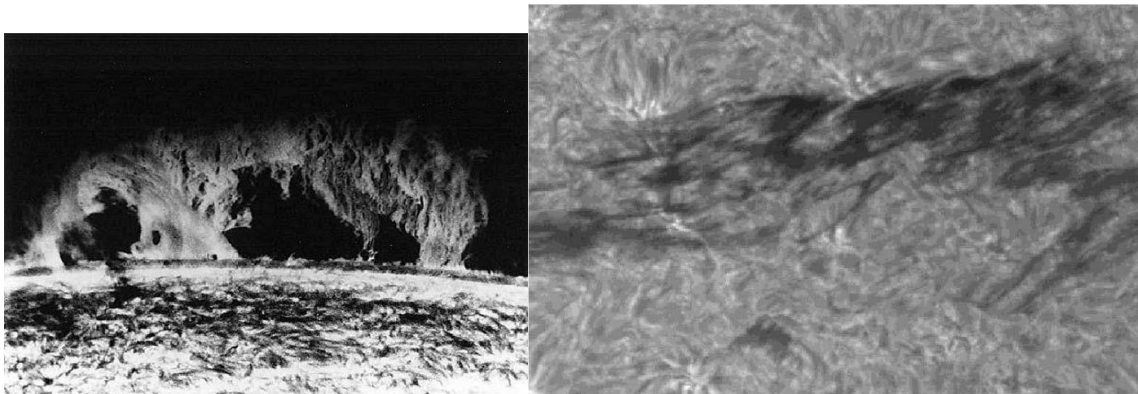


Figure 13a: A small “hedgerow-shaped” prominence above the limb which appears bright in $H\alpha$ against the black space background. Figure 13b: A large polar crown filament on the disk. Image credit: BBSO (left) Swedish Vacuum Solar Telescope (right)

There is a great variety of sizes and shapes of filaments/prominences as their appearance depends on the magnetic environment. Filaments that are over narrow polarity inversion zones of opposite polarity between dense plages (bright patches surrounding sunspots where there are concentrated magnetic fields) are very thin, with almost no lateral structure (Martens & Zwaan, 2001). The corresponding prominences are low, with heights of about 1000 km or less. The other extremes are the filament/prominences found over a very weak magnetic network; these are much higher and more irregular in shape, with a detailed structure (Martens & Zwaan, 2001). Even though there are variations in size and shape, all filaments/prominences have similar magnetic structure because there is continuity in the appearances, which may form an evolutionary sequence (Martens & Zwaan, 2001).

Prominence Background

Solar prominences have a relatively short history. Ancient observations of the solar corona during eclipses were recorded by Indian, Babylonian, and Chinese sources as early as 2800 BC (Aschwanden, 2006). Muratori in 1239 described them as burning holes and Vassenius in 1733 called them reddish clouds in the ‘lunar atmosphere’ (Tandberg-Hanssen, 1998). Regular observations of solar eclipses and prominences started with the eclipse of 1842, which was observed by astronomers like Airy, Arago, Baily, Littrow, and Struve (Aschwanden, 2006). It was not until the eclipse in 1851, observed in Norway and Sweden, that a suitable solar interpretation of the prominence phenomenon developed (Tandberg-Hanssen, 2011). Visual and spectroscopic observations of prominence loops were carried out by Pietro Angelo Secchi in Italy and by Charles Augustus Young of Princeton University during the 19th century (Aschwanden, 2006). The invention of photography in the late 1800’s was used to capture images of the eclipse in Spain in 1860 and a spectrograph captured images of the eclipse in 1868 in India and Malacca where both showed that the spectrum of prominences (bright lines) were masses of solar glowing gas (Tandberg-Hanssen, 2011). Janssen in 1868 discovered he could view prominence emission lines in full daylight without an eclipse by placing the slit of the spectrograph outside the limb of the sun. Lockyer and Huggins at the same time, made the same discovery (Tandberg-Hanssen, 1998). George Ellery Hale built a spectroheliograph in 1892 and observed coronal lines during eclipses. In 1905 Schwarzschild using this invention provided the first photometric measurements of spectral lines in prominences (Tandberg-Hanssen, 1998). Bernard Lyot built a coronagraph at the Pic-du-Midi Observatory in 1930, an instrument that occults the bright solar disk and made it possible to look at prominences

at any time, not just when an eclipse was occurring (Tandberg-Hanssen, 1998, 2011, Aschwanden, 2006).

In 1961 Zirin and Severny used a magnetograph to measure the longitudinal magnetic field of prominences using the Zeeman Effect (splitting of certain spectral lines when in a magnetic field) as it became clear that magnetic fields played a major role in the physics of prominences (Tandberg-Hanssen, 2011). Studies in France at the Meudon and Pic-du-Midi Observatories used the Hanle Effect, (a depolarization due to a magnetic field) to observe prominences. Both methods are still in use today (Tandberg-Hanssen, 2011). As science progressed researchers studied prominence formation proposing several models to explain prominences and how they function (Martin, 2012, Aulanier et al., 1999, Chae et al., 2001, Antiochos & Klimchuk, 1991). Tandberg-Hanssen (1998) suggested that the prominence models can be divided into two classes: those that study the support of the prominence in the solar atmosphere and those that describe the internal, thermodynamic structure of the prominence plasma.

Quiescent and Active Region Prominences/Filaments

Prominences are embedded in the solar corona and chromosphere and contain relatively dense, cool material that is confined by magnetic fields anchored in the photosphere and lying above a PIL (Tandberg-Hanssen, 1998). Aschwanden (2006) describes them as horizontal magnetic field lines overlying a neutral line of an active region that are filled with cool gas from the chromosphere embedded in the much hotter tenuous coronal plasma. Prominences always occur at the boundary between opposite polarities of magnetic fields, the polarity inversion line (Martin, 1998). Although prominences are anchored in the photosphere and extend outwards following magnetic field lines rising into

the corona, they form in the chromosphere, where they exist before erupting or upward motions occur (Martin, 1998).

Quiescent prominences and active region prominences are categorized by where they appear on the Sun and have very different magnetic structures and formation processes (Martin 1998). Prominences differ in the amount of activity ranging from quiescent, when the prominence shows little internal motion and has a stable size and shape, to active when there are many small-scale motions and flows visible and often an increase in absorption, occurring over a period of a few hours (Martin, 1998). Eruptions start with a slow rise, followed by a sharp change to a fast rise when they are high in the corona (Sterling & Moore, 2001). Prominence eruptions can be full, where all of the material is expelled, partial, where only some of the mass erupts, or failed, if the material resettles or falls back to the surface and does not result in a CME (Gilbert et al., 2007a). A prominence can appear in a day, extend for thousands of kilometers and last for months. Prominences contain cool ($T < 10^4$ K) and dense (electron density 10^9 - 10^{11} cm⁻³) plasma in the hot solar corona and can be 100 times cooler and denser than its coronal surroundings (Labrosse et al., 2010). The relatively cool looped plasma is mainly made up of hydrogen and helium that is partially ionized (Gilbert et al., 2002). Their dimensions are approximately 10^4 - 10^5 km in length, and 10^3 - 10^4 km thick and their heights are 10^4 - 10^5 km (Labrosse et al., 2010).

Quiescent prominences are stable structures that can last for several months, while eruptive active prominences are usually associated with flares and coronal mass ejections (Aschwanden, 2006). However, high-resolution movies from H α ground-based and space-based observations have shown that usually stable quiescent prominences can still show quick changes in their fine structure even in only a few minutes (Labrosse et al., 2010).

Active prominences are more dynamic and are found close to active regions; they last from a few minutes to hours, with smaller heights (Labrosse et al., 2010). Intermediate prominences/filaments have a footpoint, the point of intersection with the photosphere, near an active region. Quiescent prominences/filaments are found all over the Sun and have magnetic fields that are concentrated into separate regions with much weaker fields in between, which is actually a zone of mixed polarity (MacKay et al., 2010). Figure 14 shows a quiescent filament seen in $H\alpha$ through different instruments.

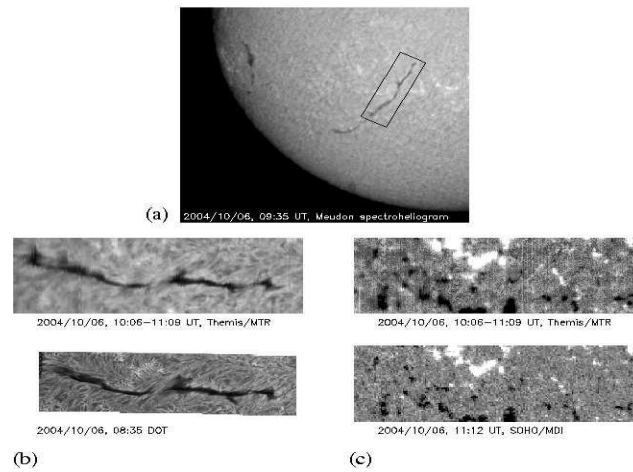


Figure 14: (a) Shows a prominence in Meudon spectroheliograph in $H\alpha$. The box shows the THEMIS/MTR field of view (b) shows the prominence in THEMIS/MTR and DOT in $H\alpha$ line center line (c) shows the prominence in THEMIS/MTR and SoHO/MDI. Image credit: Mackay et al., 2010.

Structure of Prominences/ Filaments

Labrosse et al., (2010) describe prominences/filaments as dynamic bundles of small-scale structures in constant evolution. The structure consists of three parts: a spine, barbs, and two ends contained in a filament channel. A magnetic arcade of several coronal loops typically arches over the prominence along the length of the spine. An overlying arcade is a requirement for filament formation in addition to being located at a boundary

between opposite polarity magnetic fields (Martin, 1990). No filament has ever been observed without the overlying arcade; although there are many sites under coronal arcades, where filaments can form, not all arcades have filaments beneath them (Martin, 1998). The spine runs horizontally along the top of the filament, but sometimes parts of the spine are almost invisible due to a lack of mass (Labrosse et al., (2010). The shapes of the spines of many filaments look like either an S or an inverted S. These S-shapes (or inverted S-shape) of filaments stand out in soft X-ray images. Rust & Kumar (1996) using images from the Yohkoh soft X-ray telescope investigated (inverted) S-shaped X-ray filaments occurrence based on the hemisphere. They found a majority of inverted S-shapes in the northern hemisphere and S-shapes in the southern hemisphere; over the equatorial regions X-ray filaments consisted equally of both S- and inverted S-shapes.

The barbs look as though they stick out from the side of the filament and when viewed at the limb, the barbs are seen to extend down from the spine to the chromosphere below. The barbs and the ends of the filament (legs) are a bundle of threads that end at a single footpoint or at multiple points (Mackay et al., 2010). Barbs are connected to patches of minor polarity on each side of the filament. Minority polarity is the polarity opposite to the dominant polarity of the network on the same side of the filament (Martin, 1998). However, the relationship between filament magnetic fields, weak and strong background fields, and minority polarity patches has not yet been explained (Martin, 1998). The threads have widths of about 200 km and are aligned with the local magnetic field. Barbs can develop quickly from mass motions along the spine and can flow to the chromosphere at the side of the prominence. Barbs can also disappear when they return their mass to the spine. The appearance and disappearance can happen in minutes (Joshi et al., 2013).

Individual threads have lifetimes of only a few minutes, but the filament itself can exist for many days (Mackay et al., 2010). Figure 15 shows an image of a filament showing the spine and the thread-like barbs.

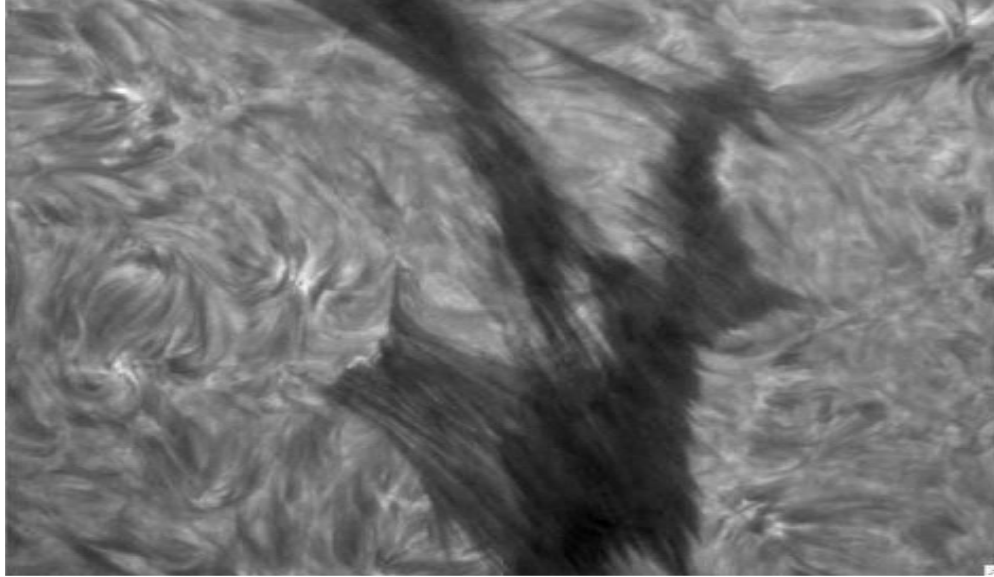


Figure 15: A high resolution H α image of a filament spine with barbs extending out from the spine. Obtained from the Swedish Solar Telescope. Image credit: Mackay et al., 2010.

For filaments to form there must be a convergence of areas of opposite polarity magnetic fields. After the opposite polarities meet, the magnetic field of those magnetic field patches begins to disappear; this disappearance is called cancellation (Martin, 1998). This is considered to be the disappearance of flux by its upward transport through the near photospheric layer after magnetic reconnection at the photosphere; the magnetic fields near the filament reconfigure and form a horizontal component in the corona that becomes filled with filament mass (Martin, 1998). The rate of change of the fine structure is always short, in the range of ten minutes and no prominence has ever been observed with stationary fine structure and Martin (1998) concludes that mass motions are an invariable condition of prominence existence. Up flows and down flows are consistently observed; how this is

accomplished has not been definitely established; it is proposed that there must be some force which can oppose gravity (Martin, 1998).

It is difficult to compare a filament with itself when it becomes a prominence as it moves across the limb, because the fine structure always changes with time. Also active region filaments have low heights and blend in with the height of the spicule (jet-like eruptions ejecting material off the chromosphere into the corona) forest so they are hard to see at the limb. Figure 16 (a) and (c) show prominences that can be seen above the spicule forest (b) a hedgerow prominence (Mackay et al., 2010).

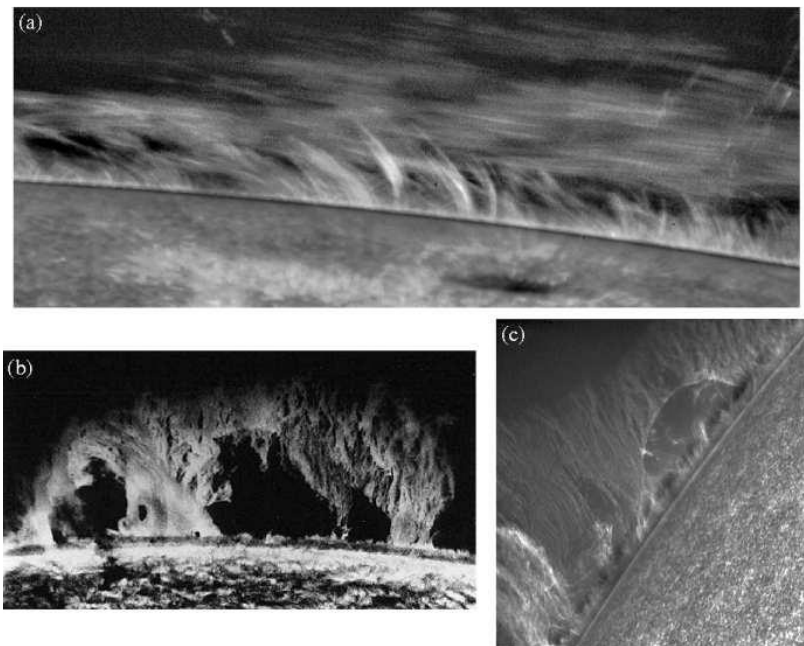


Figure 16: Examples of solar prominences in different wavelengths: (a) Ca II H INODE/SOT image (b) BBSO H α image (c) Ca II H HINODE/SOT image. Image credit: Mackay et al., 2010.

Fibrils are small fine darker filament-like features which tend to run along magnetic field lines and align themselves horizontally and parallel to the PIL (Martin et al., 1994). The footpoints of fibrils are in positive and negative flux regions and interact with other

fibril footpoints that ultimately magnetically connect combining into one; they are connected to or part of the larger filament structure, curving into or running along the filament's main axis (Martin et al., 1994). Foukal (1971a) discovered that the fibrils at both sides of the channel are *antiparallel*, from which he concluded that the magnetic field below the filament has a strong horizontal component along the channel axis of the filament and points in the same direction on either side of the channel. Figure 17 shows a schematic of a fibril located next to a filament. (Plagettes are little plages above small network magnetic field clusters (Martin et al., 2012)).

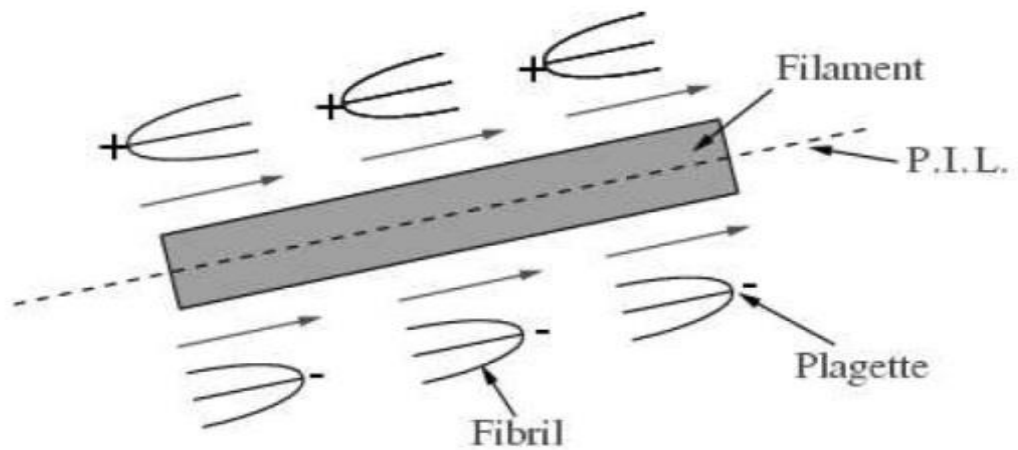


Figure 17: An image of a filament channel with fibrils which lie anti-parallel to one-another on both sides of the PIL. The fibrils are nearly parallel to the path of the PIL. Image credit: Mackay et al., 2010

Filament Channels

Filaments always form above a PIL, beneath a coronal arcade and along a *filament channel*, which is basically a neutral magnetic field region between the two opposite polarity regions (Martin, 1998, Gaizauskas, 1998, Bhatnagen & Livingston, 2005). According to Martens & Zwaan (2001), fibrils on either side of the channel are nearly parallel to the channel axis or if the parallelism is not perfect, the fibrils are slightly turned

away from the axis; they are never inclined toward the axis. Filaments only form in completely developed channels of fibrils where no fibrils cross the PIL. Channels can form rapidly or slowly. These channels, much longer and broader than the filaments, form prior to the appearance of visible filament mass and can survive successive filament eruptions (Martin, 1990).

A filament channel can also be defined as a region in the chromosphere along a PIL where the chromospheric fibrils are aligned with the PIL; not every filament channel contains a filament, nor does every PIL develop an associated channel (Su et al., 2010). The fibrils indicate the direction of the magnetic field in the chromosphere. Martin et al. (1994) noted that the *fibrils* in the channel show a streaming pattern that is opposite on the two sides of the channel. The horizontal part of the *magnetic field* must point in the same direction on the two sides of the channel (Martin et al., 1994). A required precondition for the formation of a filament channel is a magnetic field with a strong horizontal component. Foukal (1971a) in a study of filament channels found that chromospheric fibrils aligned themselves in bands along a PIL in, or beside, an active region. Because the H α fibrils in a band on one side of a channel have their orientation opposite to that of the fibrils in the band on the other side of the PIL, he concluded that the *magnetic field* has a predominantly horizontal component along, not across, the axial direction of a filament channel (Gaizauskas et al., 2001).

Gigolashvili (1978) concluded that there is a preference for left handed spiral motions in prominences in the northern solar hemisphere and right handed motions in the southern hemisphere (Martin et al., 2012). Martin et al., (1994) proposed the concept of chirality (handedness) of filament channels which were either dextral (right handed) or

sinistral (left handed) depending on the direction of the magnetic field of the channel. They also determined that channels in the northern hemisphere are mainly dextral, while those in the south are mainly sinistral. Therefore, the chirality of filaments can be determined either indirectly from the channel or directly from magnetic field measurements (Martin et al., 1994). Figure 18 is a depiction of the chirality of filament channels.

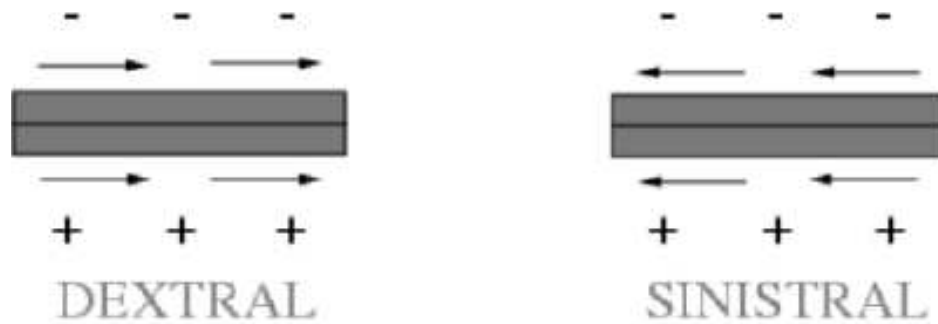


Figure 18: The chirality of a filament channel is defined by the direction of the magnetic field along the channel. A dextral channel, the magnetic field points to the right; a sinistral channel, the magnetic field points to the left. Image credit: Mackay et al., 2010.

Pevtsov et al., (2003) in a study of filaments found that 80% of quiescent filaments in the northern hemisphere are dextral and 85% of filaments in southern hemisphere are sinistral, in agreement with the hemispheric helicity rule (solar magnetic fields in the northern hemisphere have negative sign of helicity; fields in the southern hemisphere have positive helicity) Helicity is the twist and writhe of the magnetic field lines; sheering and twisting of magnetic field lines cause helicity. Their data showed the active region filaments follow the same rule: 75% of active region filaments in the northern hemisphere are dextral, and 77% of filaments in the southern hemisphere are sinistral (Pevtsov, 2003).

Martin et al., (1994) reported the chirality of filament channels and the chirality of filaments as a one-to-one relationship of dextral (sinistral) filament barbs to the dextral

(sinistral) fibril patterns of filament channels. Filaments in dextral channels have right-bearing barbs, and those in sinistral channels have left-bearing barbs (Mackay et al., 2010). The chiralities of filament channels and filaments can be found by the direction of fibrils in the chromosphere and threads in the filaments (Martin et al., 2012). Figure 19 shows fibrils on the positive field side of the filament which are like arrows *directly* showing the direction of the local magnetic field and *indirectly* indicating the magnetic field direction along the PIL (dashed line which also is the filament spine).

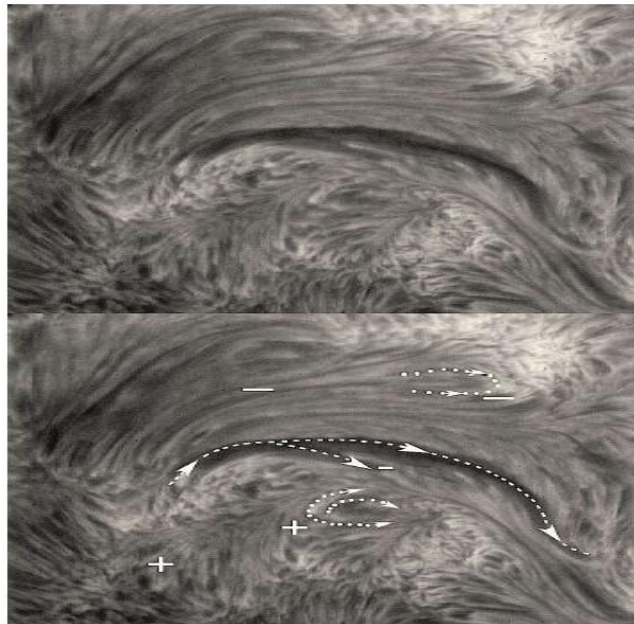


Figure 19: The arrows in the lower image indicate the direction of the magnetic fields of the fibrils in a filament channel and the direction of the magnetic field of the spine of the filament. Image credit: The Dutch Open Telescope (Martin et al., 2012).

Martin et al., (1994) suggest that the ends of the barbs of filaments on the disk are connected to weak magnetic fields with opposite polarity called minority or *parasitic polarity* regions, compared to the majority polarity elements on the side where the barb is located. These minor polarity areas are constantly being recreated by supergranule cells

and occur all along the filament channel. When the parasitic (minority) polarity and the dominant polarity outside the channel interact, flux cancellation occurs creating larger structures including the barbs (Mackay et al., 2010). Wang & Muglach (2007) propose that flux cancellation between the parasitic polarity and the nearby dominant polarity contributes to the formation of filament barbs. On the other hand, Liu et al., (2010) studied quiescent filament barbs where the chirality changed within hours. Only one of the four barbs overlay a small PIL inside the filament channel and no magnetic elements were found at the endpoints of all barbs. They concluded that the evolution of the barbs was driven by flux emergence and cancellation of small dipole units at the filament channel border and questioned the reliability of barbs as the indicator of filament chirality.

Chirality Relationships

Filament channels are a key component of filaments/prominences that are supported by magnetic fields and continue to exist even when their contents (i.e., the filament) erupts. A single filament channel may survive successive eruptions and reformations of its filament (Gaizauskas et al., 2001, Martin et al., 2012). A dextral filament will contain dominantly negative helicity, while a sinistral filament will contain positive helicity (Mackay et al., 2010). Pevtsov et al., (1994) found that active regions as a whole could be characterized according to their helicity. Martin and McAllister (1996) reported that the chirality of coronal loops and flare loops also have one-to-one relationships with filament channels and filaments. Coronal loops and flare loops were found to be opposite in chirality to filament channels and filament barbs in the same system (Martin et al., 2012). Martin, (1998) proposes that the cavities around filaments exist because filaments and

arcades have opposing helicity. Figure 20 summarizes the one to one chirality relationships.

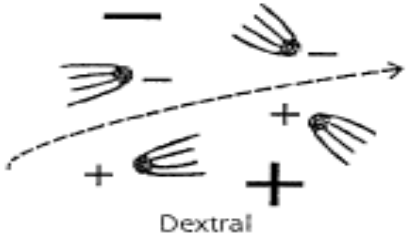
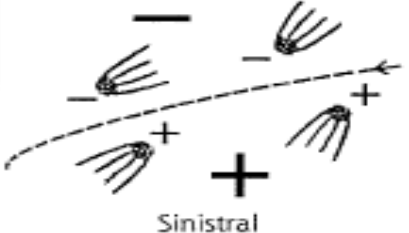
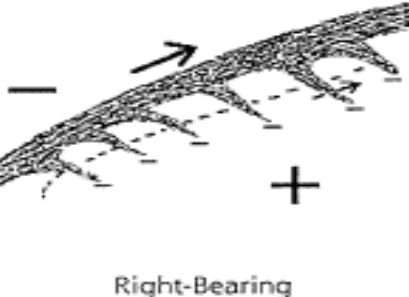
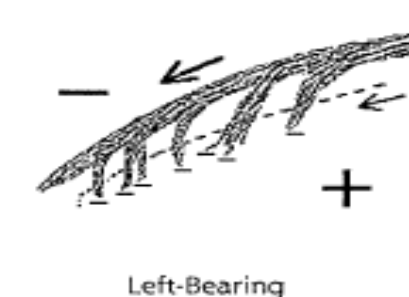
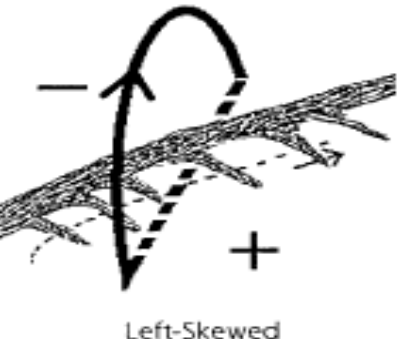
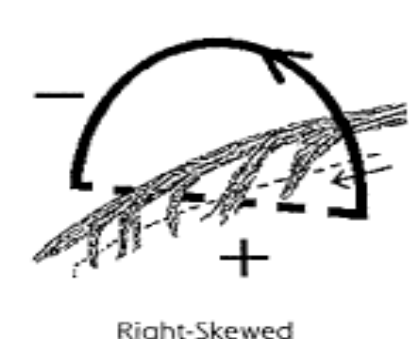
Feature	Chirality	
		N L _w
1. Filament Channels Small Scale	 Dextral	 Sinistral
2. Filaments Medium Scale	 Right-Bearing	 Left-Bearing
3. Coronal X-Ray Arcades Large Scale	 Left-Skewed	 Right-Skewed
	Dominant in Northern Hemisphere	Dominant in Southern Hemisphere

Figure 20: One-to-one chirality relationships for (1) fibril patterns, (2) filament spines and barbs, and (3) overlying arcades of coronal loops, are shown in each column. The patterns on the left are dominant in the northern hemisphere and the patterns on the right are dominant in the southern hemisphere. Image credit: Martin, 1998.

Martin et al., (2012) propose a “Chiral System” to illustrate filament formation and the buildup to a CME. The key features are depicted in

Figure 21. The components are: (1) a coronal loop system (blue), (2) a filament channel with representative fibrils (green), (3) a filament with a spine (red), (4) barbs (green), and (5) a sigmoid in the cavity, an area where the density is extremely low all around the filament and within the coronal loop system (Martin et al., 2012).

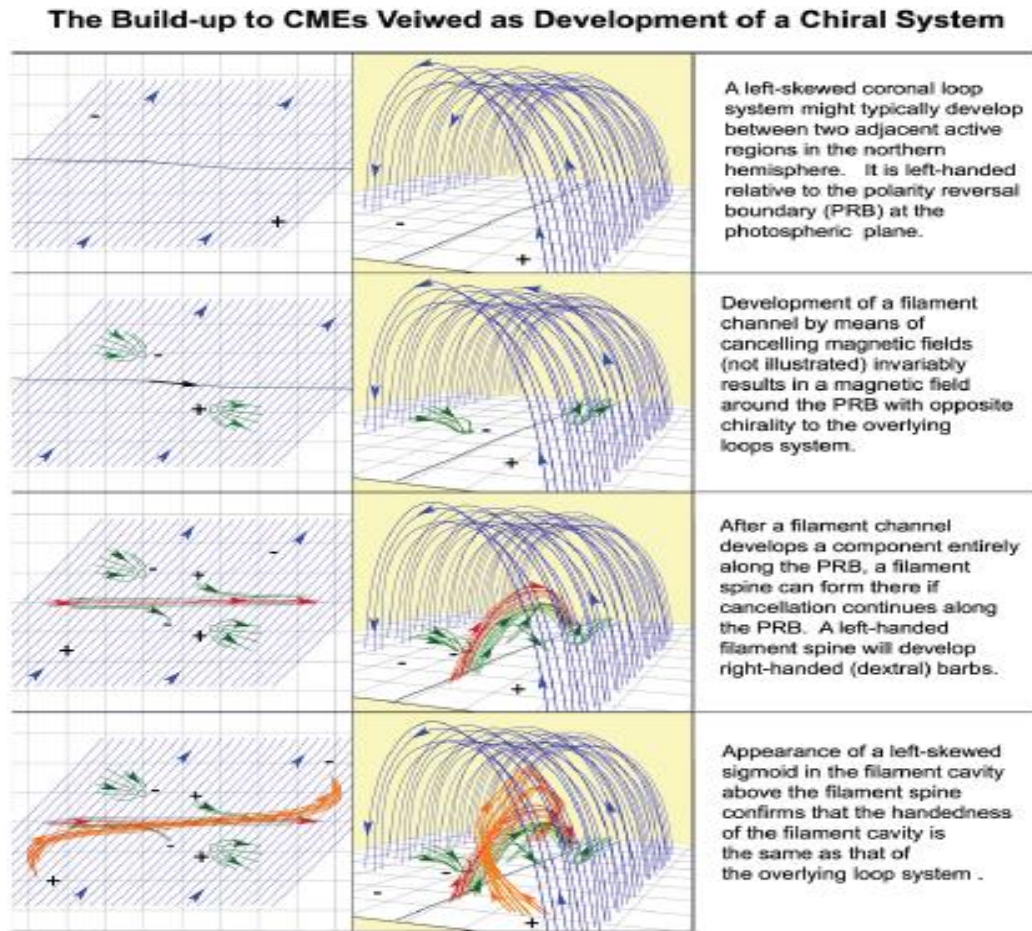


Figure 21: This diagram shows a chiral system building up to a CME. A left skewed sigmoid can be seen forming under the coronal arcade. Image credit: Martin et al., 2012.

A Chiral System develops from the outside to the inside. The initial coronal loops (left-handed in this example), are balanced by the development of a right-handed filament channel. In the filament channel, the development of a filament with a left-handed filament spine always produces right-handed (dextral) barbs (Martin et al., 2012). Wang et al.,

(2009) confirmed that the filament spine is left handed if its barbs are right handed. According to Martin et al., (2012), these observations suggest that net helicity of a complete chiral system might be close to zero and that the conservation of helicity might apply to a chiral system. Martin et al., (2008) suggest that the formation of filament channels and filaments is the early part of a long term buildup that begins with the formation of a filament channel and continues until an eruptive solar event occurs such as the eruption of a filament, a solar flare and a CME. The buildup of filament channels is linked to cancelling magnetic fields which results in magnetic reconnection at or very close to the photosphere (Martin et al., 2012). Martin et al., (2012) propose that the mechanism for cancelling magnetic fields can be the source of the buildup of energy and helicity in active regions, specifically at the sites of filament channels and may be at any location where cancellation is seen. Magnetic fields below an erupting prominence reconnect releasing stored energy as a solar flare. This reconnection is also known as “tether cutting,” since the magnetic fields in the reconnection are like tethers holding down the prominence (Sterling & Moore, 2003).

Helicity buildup can be important from the very beginning in active regions because cancellation takes place between simple bipoles in the earliest stages of active region formation (Martin, 1990). A schematic of a possible way to produce helical fields is shown in Figure 22 where shearing and reconnection forms helical field lines above the neutral line (PIL). Another model suggests that twisting occurs in the convection zone and the flux tube comes through the photosphere already twisted (Rust & Kumar, 1994). Observations also show that prominences tend to form in regions where opposite polarity flux is

cancelled at the neutral line, where shearing and reconnection forms helical field lines as shown in Figure 22 (Van Ballegoijen & Martens, 1989).

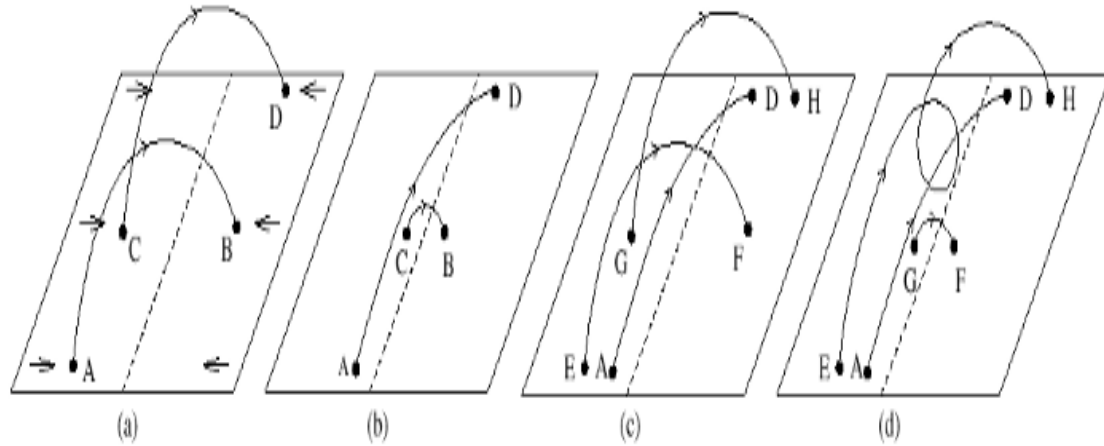


Figure 22: A diagram of Magnetic reconnection between the sheared loops AB and CD produce a long loop AD which forms helical field lines. The dashed line is the PIL. Image credit: Van Ballegoijen & Martens, 1989.

This model suggests that reconnection also produces longer and more sheared field lines above the neutral line, slowly increasing the prominence until it eventually becomes unstable and erupts (Aschwanden, 2006, Van Ballegoijen & Martens, 1989). Martin et al., (2012) suggest there are solar eruptions because the Sun must expel energy and helicity built up in the solar atmosphere. Because CMEs only occur above filament channels (Martin et al., 2008), there is a link between CMEs and the development of chiral systems that include filament channels and filaments. Eruptive solar events, flares, erupting filaments and CMEs, according to Martin et al., (2012) do not cause one another; instead, they all have a common cause. A concise flowchart that describes the stages of the ‘Key Processes of the Buildup to Eruptive Solar Events’ proposed by Martin et al., (2012) is shown in Figure 23.

The Build-up to Eruptive Solar Events

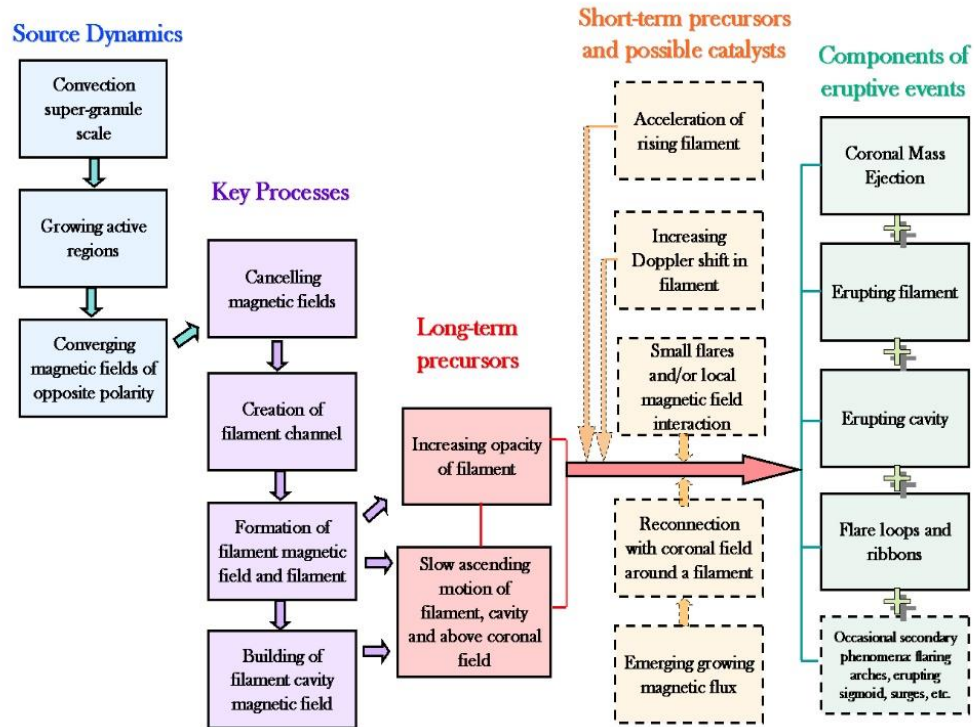


Figure 23: This is a schematic representation of stages of the build-up to a CME from the source dynamics and key processes in columns 1 and 2 respectively to the components of eruptive solar events in column 5. Image credit: Martin et al., 2012.

Martin et al. (2012) describes the stages of the long term build-up beginning with the formation of a coronal loop system between adjacent active or decaying active regions, followed by the convergence and cancellation of magnetic fields along the PILs below the coronal loop systems resulting in the formation of a filament above a filament channel. The growth of a filament cavity magnetic field can result in the development of a sigmoid, but always leads to an eruptive solar event - a CME, often with an erupting filament and a flare.

Magnetic Reconnection

Virtually all plasmas generate magnetic fields which inevitably lead to magnetic reconnection (Priest & Forbes, 2000). Magnetic reconnection is the formation of

connections between bipolar regions. Reconnection is essentially a topological restructuring of a magnetic field caused by a change in the connectivity of its field lines resulting in magnetic energy being converted to kinetic energy, thermal energy, and particle acceleration (Priest & Forbes, 2000). This reconnection allows the release of stored magnetic energy, the main source of free energy in plasma; how this occurs is still not clear (Priest & Forbes, 2000). All magnetic phenomena on the Sun, prominences, flares, the corona and sunspots require reconnection which may be the mechanism that heats the solar corona to extremely high temperatures (Priest & Forbes, 2000).

According to Aschwanden, (2006) there are three reasons why the coronal magnetic field is constantly stressed and has to adjust by restructuring the large-scale magnetic field (i.e., magnetic reconnection processes): 1. The solar dynamo in the interior of the Sun constantly generates new magnetic flux from the bottom of the convection zone (the tachocline) which rises by buoyancy and comes through the photosphere into the corona; (2) the differential rotation as well as convective motion at the solar surface continuously wrap up the coronal field with every rotation; and (3) the connectivity to the interplanetary field has to constantly break up to avoid excessive magnetic stress.

Magnetic reconnection always releases free non-potential energy, which is converted into the heating of plasma, acceleration of particles, and kinetic motion of coronal plasma (Aschwanden 2006). When a new magnetic flux system is pushed towards an old magnetic flux, a new dynamic boundary is formed where the magnetic field can be directed in opposite directions at both sides of the boundary (Aschwanden 2006). The magnetic field drops to zero at the boundary allowing a continuous change from a positive to a negative magnetic field strength (Aschwanden 2006). Bringing two oppositely directed

magnetic flux systems together will always have a set area of first contact, which limits the size of the neutral boundary and channels outflows to both sides, shown in the 2D model in Figure 24, where the inflows (driven by external forces) will cause outflows along the neutral line in an equilibrium situation. The plasma can flow across the magnetic field lines, called the Diffusion Region, and is channeled into the outflow regions along the neutral boundary (Aschwanden, 2006).

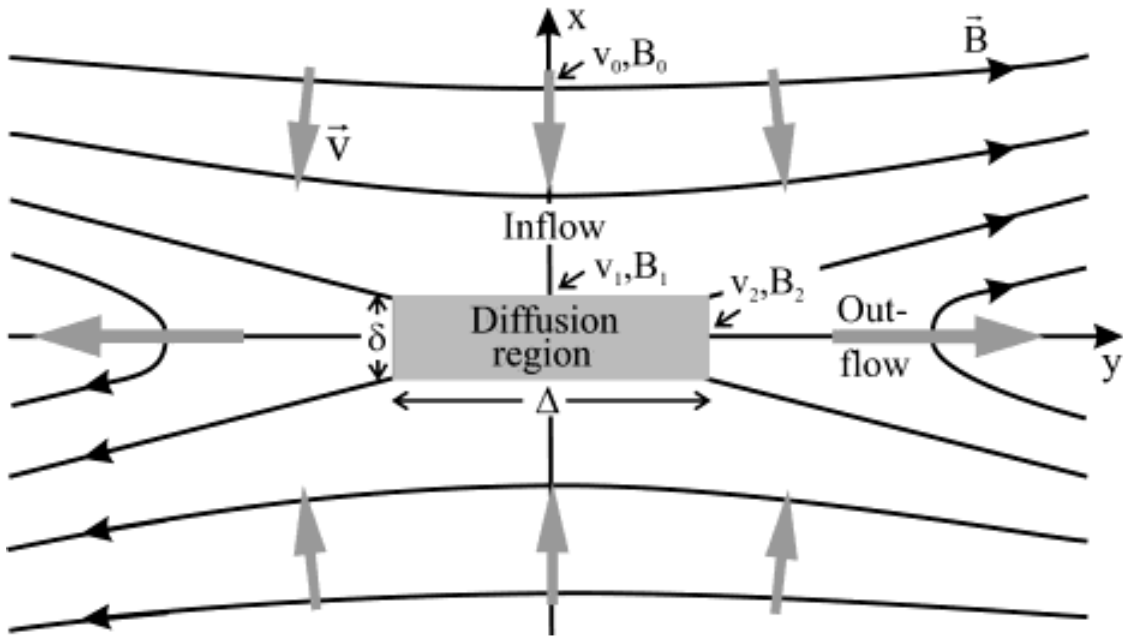


Figure 24: A basic 2D model of a magnetic reconnection process. Two oppositely directed inflows collide and create oppositely directed outflows. Image credit: Schindler & Hornig 2001.

Flux Cancellation and Counterstreaming

Flux cancellation is the disappearance of photospheric magnetic flux caused by opposite polarity fields interacting in the photosphere (Mackay et al., 2010). It happens all over the Sun, but especially at large PILs on the quiet Sun. Wang, (2001) obtained results that support magnetic reconnection with photospheric flux cancellation as the main method for injecting mass into quiescent prominences (Mackay et al., 2010). Martens and Zwaan,

(2001) stated that downward pointing barbs, linked to parasitic polarity elements, form because of the failed cancellation of the motion of flux elements across the PIL; these changes of minor polarities in filament channels lead to strong changes of H α filaments and they believe prove directly the relationship between minor polarities and barbs/ ends of filaments. The disappearance and reappearance of a part of a filament seems to be a result of the emergence of magnetic flux, followed by cancelling flux (Schmieder et al., 2006). Counter streaming is material flowing along the spine of a filament in both directions; the same happens in the barbs with up-flows from the barbs into the spine in one part and down-flows in another part. What causes the flows is unknown but the barbs seem to be parallel to the magnetic field (Mackay et al., 2010). Studies by Lin et al., (2003, 2005) and Schmieder et al., (2007) found counterstreaming in filament threads in H α with velocities in the range 7-15 km/s and speeds in one instance as high as 30 km/s. They also found that material flows up and down the barb structures with the downward flow slower than expected if the material were falling unrestricted under the force of gravity. This means that there is a mechanism that acts as an upward force to the cool material while still letting it move up and down easily (Labrosse et al., 2010). Active region prominences have a high level of activity with easily seen flows along the prominence axis (Tandberg-Hanssen, 1998). Chae, (2003) found fast (80-250 km/s), jet-like and eruptive behavior in a forming active region filament.

In a study of a hedgerow prominences (cluster of smaller prominences) Chae et al., (2008) found strong horizontal flows of H α emitting plasma that came from the chromosphere and rose to the corona then extended horizontally until reaching the main body of the prominence. Horizontal field lines are essential for the extended presence of

material to be suspended in the corona (Kilper et al., 2009). In higher altitudes the flows either moved across vertical threads or lifted them up, while in the lower altitudes they formed bright blobs of plasma which disappeared as soon as they formed by going down the thread resulting in a sudden change of flow direction from horizontal to vertical (Chae et al., 2008). The study shows that there is a consistent horizontal flow which supports the idea that there are initially horizontal magnetic fields and that vertical threads in quiescent prominences are stacks of plasma supported against gravity by the sagging of initially horizontal magnetic field lines (Chae et al., 2008).

Disparition-Brusque and CMEs

The lifetime of a prominence is determined by the balance between heating and cooling. A sudden disappearance of a prominence is called a disparition brusque, where an instability causes a subsequent eruption into the corona and interplanetary space, often with a flare or a CME (Aschwanden, 2006). Prominences usually show activation, increased motions or a disparition brusque before a flare so this can be considered a good flare precursor (Tandberg-Hanssen, 2011). Before a quiescent prominence undergoes a sudden disappearance from an ascending motion, the prominence plasma shows increased velocities and then the whole prominence begins to rise at several hundred km/s (Tandberg-Hanssen, 2011). Flows in the photosphere below the prominence can affect the stability of the magnetic field supporting the prominence. Studies found there was an increase in zonal shear below the starting point of the eruption and a decrease after the eruption which may affect the coronal field triggering a CME (Mackay et al., 2010).

Following CMEs, quiescent prominences often reform in the same location so despite the disturbances, the conditions for their formation are stable for periods of up to

many months (Berger et al., 2010). Filaments erupt due to magnetic reconnection below the filament causing the material along the PIL to move outward. This does not affect the PIL; as a result material immediately starts to move along the channel recreating the filament which just erupted. Material erupts in a reconnection event sometimes gets caught in the Sun's gravity and is pulled back down towards the surface, sometimes returning to the filament channel from which it just tried to escape (Martin et al. 2004).

Models of Magnetic Field Configurations

Prominences are supported, shaped, and filled with magnetic fields. There are several models proposed for prominence magnetic field configurations but all are variations on the three basic models as shown in Figure 25.

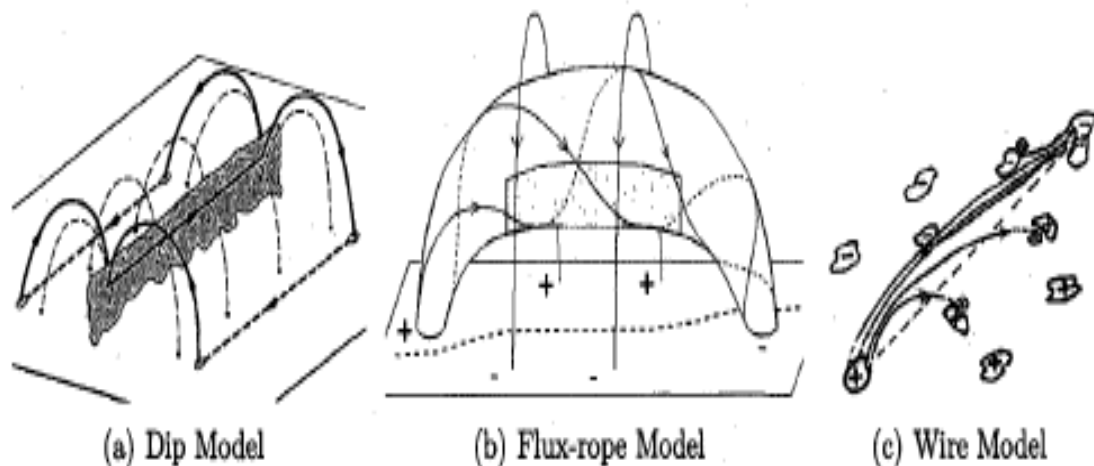


Figure 25: This is a schmeatic diagrams showing the prominence magnetic field structure in the (a) dip model, (b) flux rope model, and (c) wire model. Image credit: Kilper, 2009.

Dip Model

Two different types of static prominence models were proposed: the Kippenhahn & Schluter (K-S) (1957) model and Kuperus & Raadu (K-R) (1974) model to explain

prominence magnetic field configurations (Mackay et al., 2010). In 1957, Kippenhahn and Schluter (1957) proposed a model of a solar prominence showing how cool plasma can be supported against gravity by a magnetic field containing dips in the field lines (Mackay et al., 2010). Because of the weight of the prominence plasma it can distort the magnetic fields causing dips. The dip is where coronal plasma collects and cools to chromosphere temperatures. In this dip model, the gravity of the material is balanced by the magnetic tension due to the dip in the field, but the actual formation process is unclear, i.e., whether the dips exist first and cause the material to collect, or does the presence of material create the dips, which then causes more material to condense (Kilper et al., 2009, Mackay et al., 2010). Because many quiescent filaments/prominences last for long periods there must be a stable equilibrium of the dense prominence plasma against the gravity force. Since the partially ionized plasma can only move along the magnetic field lines it will slide to the lowest points where it is trapped in the dips of the nearly horizontal field lines (Aschwanden, 2006).

Figure 26 is a schematic of the K-S and the K-R models. In the K-S model the polarity of the field across the prominence sheet is the same as the polarity of the photospheric field below; (positive to the negative magnetic field) this is the Normal polarity field, N-type prominences (Tandberg-Hanssen, 2011). The other type of field configuration is found in the K-R model, the Inverse polarity field, (the magnetic field points from negative to positive) the I-type prominences. I-types are seen more often than N-types, seem to be taller and are typical of polar crown prominences. N-type prominences are lower than 30,000 km (Tandberg-Hanssen, 2011).

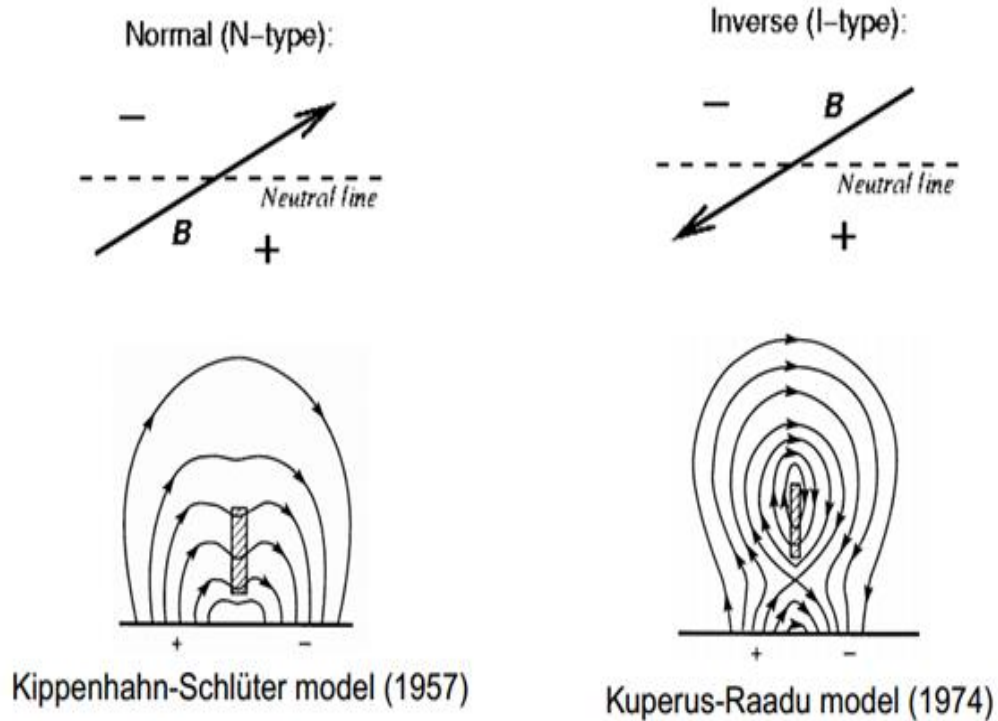


Figure 26: The Kippenhahn–Schlüter model and the Kuperus–Raadu model show magnetic fields supporting a prominence. Image credit: Aschwanden, 2006.

Flux Rope Model

The "flux rope model" was first proposed by Kuperus & Raadu (1974). The helical magnetic fields in the interior of a loop arcade suspend the prominence and support the plasma against gravity. Flux rope prominences are twisted tubes of magnetic field that *do not* require the material's gravity to create any dips; the mass is simply located at the lowest part of the helical magnetic rope at the bottom of the flux rope (Kilper et al., 2009). The flux rope is either created from a magnetic arcade that is sheared by solar differential rotation, where flux cancellation and reconnection creates the loops in the flux rope, or a buoyant flux rope is created at the tachocline and then rises through the convection zone and photosphere, up into the corona (Kilper et al., 2009). Once the structure has formed,

chromospheric material can rise up through the ends, cool, and then settle into the bottom of the series of turns within the flux rope, which can be seen in Figure 27. This model explains the existence of prominence cavities and the isolation of the prominence from the surrounding corona which the K-S model cannot (Kilper et al., 2009). Flux rope models for prominence/filament formation can be divided into two categories, those where flux ropes emerge intact from beneath the photosphere (Rust & Kumar, 1994; Low & Hundhausen, 1995) or those where weakly twisted flux ropes are formed by magnetic reconnection acting on fields that have already emerged (van Ballegoijen & Martens, 1989; Martens & Zwaan, 2001). Both types of models describe photospheric flux cancellation as the emergence of U-loops (dips) in the first model and submergence of post-reconnection loops in the second one (Welsch, 2006). In both types, the concave upward parts of magnetic field lines or dips hold and support prominence plasma by the magnetic tension force against gravity (Xia et al., 2012; Tandberg-Hanssen, 2011; Aschwanden, 2006).

Ballegoijen & Martens (1989) found that a greatly sheared arcade reconnection occurs near the base of the arcade at the photospheric level, forming a helical structure that can support prominence formation, but shear alone may not be enough. Demoulin & Priest (1989) studied the twisted flux rope model where the dip in the magnetic field configuration is formed from twisting the arcade. They found that differential rotation causing photospheric motions can cause the top of the flux rope to twist. The size of the dip will increase with the twisting until an unstable twist is reached and the prominence erupts. Figure 27 is a diagram of a twisted arcade formed by differential rotation. Figure 28 is a schematic of how a flux rope is formed.

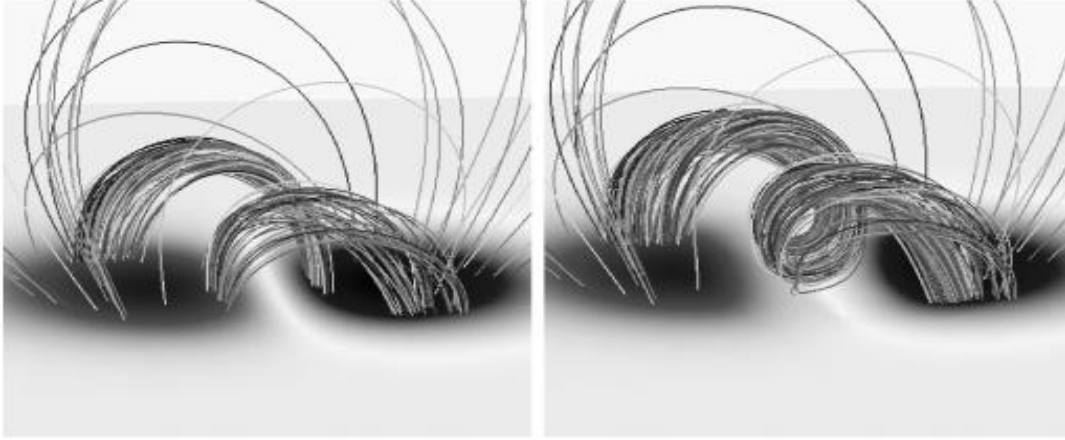


Figure 27: This figure shows the evolution from an arcade-like topology to a twisted flux rope-like topology. Image credit: Amari et al., 1999.

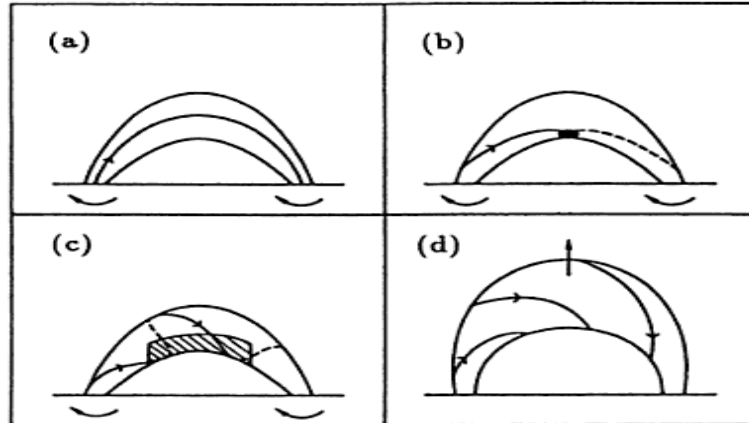


Figure 28: This figure shows the formation of a prominence in a twisted flux rope. (a) is an initial untwisted magnetic flux rope. (b) a dip begins to form as torsion is applied. (c) the prominence material is suspended at the apex of the twisted flux rope. (d) eruption occurs when the twist becomes too large. Image credit: Demoulin & Priest, 1989.

For a flux rope model the weight of the prominence plasma has no effect on the dips; it does not create the dips as the *dips already exist* in twisted flux ropes; the mass is located at the lowest part of the helical magnetic tube (Aulanier et al., 2002). In a study by Lopez et al., (2006) they concluded that dips are consistent with the presence of a weakly twisted flux rope in the corona above the PIL and the filament is supported by dips in the helical field lines. The flux rope must be close to stable equilibrium and needs a coronal

arcade on top of the flux rope to provide magnetic tension forces to hold down the flux rope in the corona (Mackay et al., 2010; Aschwanden, 2006). Martin & McAllister (1996) studied the structure of these arcades and found a strong correlation between the orientation of coronal loops within the arcade and the handedness of the associated filament: left-skewed arcades have dextral filaments and right-skewed arcades have sinistral filaments. This means that the direction of the axial field in the coronal arcade is the same as the filament and the filament channel (Mackay et al., 2010). Since the prominence plasma is located in the dips of the helical windings, the flux rope model predicts that the magnetic field at the prominence has inverse polarity (I type) compared to the surrounding photospheric fields (Mackay et al., 2010). Due to the direction of the axial field in the flux rope and the inverse polarity, any disturbance always results in right/left-bearing barbs in dextral/sinistral orientations of the axial field (Martin et al., 1994). Therefore the flux rope model provides an explanation for the observed orientation of barbs.

Wire Model

Studies from high-resolution $H\alpha$ images show that plasma material in quiescent filaments seems to be in constant motion i.e. counterstreaming flows (Martin, 1998). Some models do not have any material contained or supported within the prominence, removing the requirement of dips in the magnetic field, but instead require a continuous flow of material along magnetic field lines (Kilper, 2009). The "wire model" of Martin & Echols (1994), based on observations of quiescent filaments, consists of several long, sheared loops without any dips. The assumption is that the fine scale structure seen in $H\alpha$ images lies parallel to the magnetic field (Mackay et al., 2010). The filament consists of many threads that are highly sheared; the spine is made from the tops of the arches, and the barbs

are inclined field lines that come out from the spine and extend sideways down to the photosphere and only connect to parasitic (minor) polarities (Martin & Echols, 1994). In the wire model the filament plasma lies on the magnetic arches that are highly sheared in the direction along the PIL and the arches *do not* contain dips (Mackay et al., 2010).

Figure 29 is a 3D model of the magnetic field of a filament, the wire model from Martin & Echols (1994). Lin et al. (2008a) developed a diagram of the wire model in Figure 30. In the diagram the spine is represented by the green field lines and the barbs by blue and red field lines; the end of the filament is the dashed lines entering the fields at either end. Martin & Echols (1994) proposed that the thread-like structures are part of all filaments and that they are the basic building blocks of all filaments. Dextral filament channels produce filaments with right-bearing barbs and sinistral channels produce left-bearing barbs. In the wire model the barbs do not have to be the same chirality as the spine as they have been reconfigured by the local polarities. According to Martin et al., (2012) barbs have the same chirality as the filament channel, not the spine.

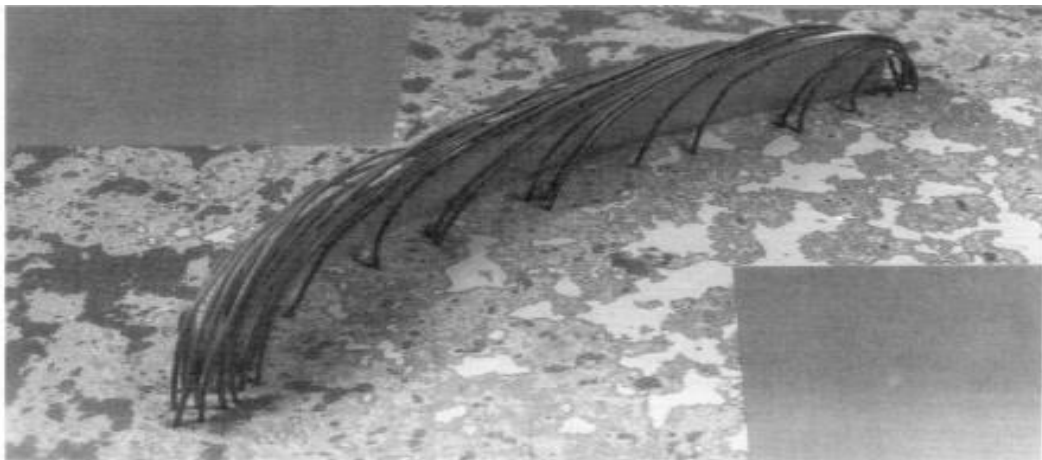


Figure 29: A model of the geometry of the magnetic field of a filament. A 3D view showing the rooting of the magnetic field to small patches of magnetic flux in opposite polarities. White is positive polarity and black is negative. Image credit: Martin & Echols, 1994.

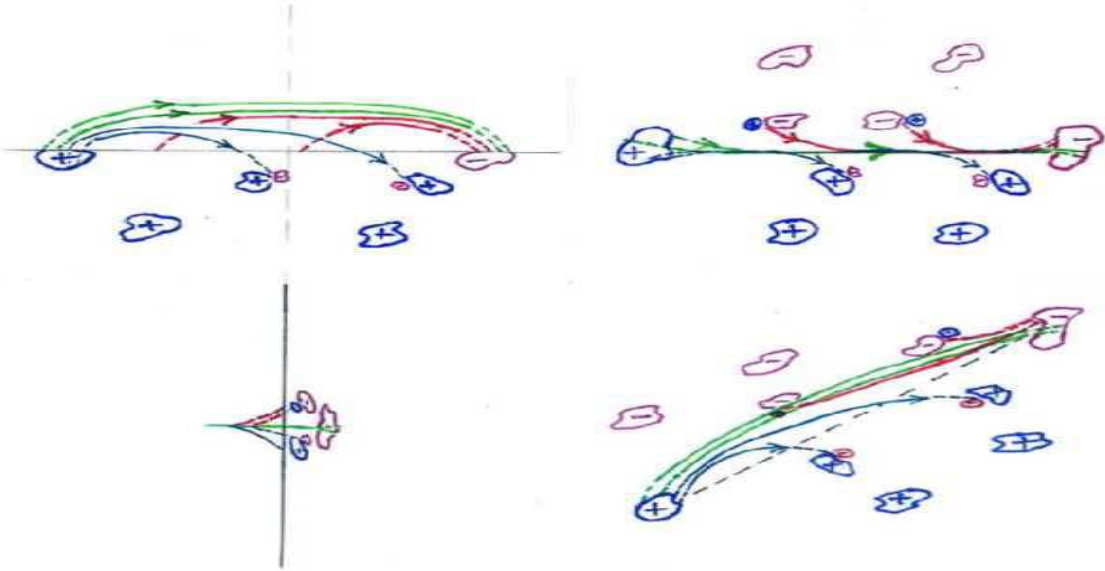


Figure 30: The Martin and Echols (1994) model of filament magnetic structure is shown in the four panels. A dextral filament is shown: the green lines shows the prominence spine, the blue and red lines show the barbs. Image credit: Lin et al., (2008a).

Because there are no spine or barb field lines with dips, there must be other (non-magnetic) forces to act parallel to the inclined field lines to support the cool dense plasma against gravity (Mackay et al., 2010). Without these forces the cool plasma would fall down to the chromosphere in minutes, which is not what happens. The model does not suggest any mechanisms for these other forces (Mackay et al., 2010).

Models of Prominence Mass Accumulation

There are three conditions required before a prominence/filament will form: (1) there must be a presence of an overlying magnetic arcade, (2) there must be a transport of flux toward the PIL under the magnetic arcade and, (3) there must be cancellation of magnetic flux that approaches the PIL (Martin, 1990, Martin et al., 1994). Filaments always form along filament channels and in regions where chromospheric fibrils are aligned with the neutral line as seen in Figure 31.

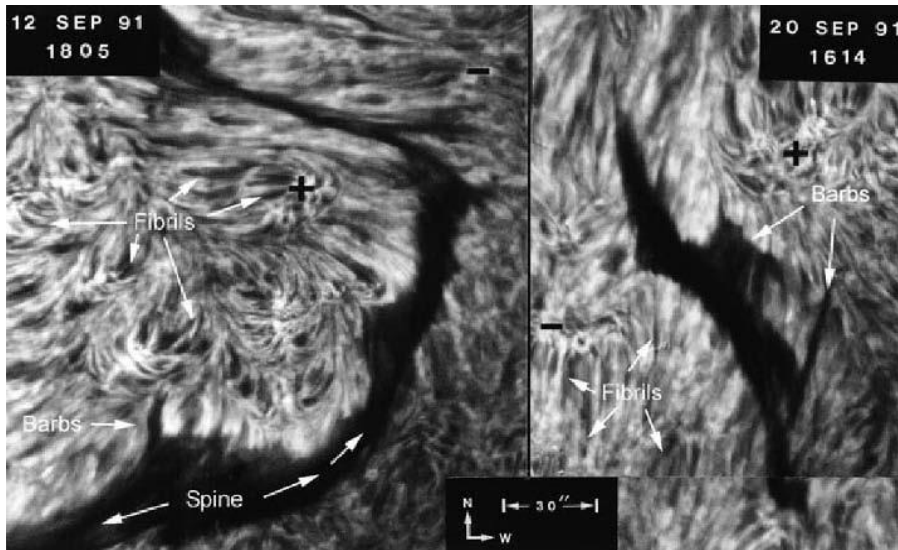


Figure 31: Left – an S-shaped filament in a filament channel. Both images show chromospheric fibrils aligned with the neutral line. Image credit: Martin, 2001.

Figure 32 is a diagram of the three main theories of how prominences obtain their mass: (1) coronal condensation of plasma with reconnection below the prominence, also known as the levitation model, (2) injection by chromospheric upflows from reconnection near the footpoints, and (3) footpoint heating triggering evaporation-condensation, also known as the thermal non-equilibrium model (Aschwanden, 2006).



Figure 32: Three different model concepts for the mass accumulation of prominences. (1) Condensation and cooling in a coronal loop, (2) upflows of cool prominence material from the chromosphere by injection at a footpoint and (3) footpoint heating that causes condensation in the coronal mid-section of the loop. Image credit: Aschwanden, 2006.

High-resolution observations show that prominence mass consists of a collection of small condensations with size scales of around 1000 km (Tandenberg-Hanssen, 1995). Since each prominence condensation is believed to form in an individual magnetic flux tube or coronal loop, each condensation is physically separated from the others by the magnetic field (MacNeice et al., 1999). The issue is that the large mass is larger than the coronal portion of the loop where it forms, so the condensation cannot be from just cooling of coronal material. The condensation mass must come from the chromosphere and come up into the loop either by flux emergence (magnetic force) or by siphon flows (MacNeice et al., 1999). Although filaments and prominences seem to be static over longer time periods, there is observational evidence that the formation is a continuous process where mass is always entering and leaving the filament magnetic field during its existence (MacNeice et al., 1999). Observations have shown that prominence material is in continuous motion with approximately horizontal speeds of 5-10 km/s with counter streaming flows of plasma passing through one another (Martin, 1998). The large mass and the horizontal flows of prominence condensations affect the magnetic field and how a prominence can form. Each magnetic flux tube must be mainly horizontal since the condensations must move along the field (Martin, 1998). Zirker et al., (1998) reported a high degree of motion with counter streaming flows in both directions along the spine of quiet Sun prominences. Kilper (2009) found that material also moves in and out of prominences, with *mass draining* (i.e. mass loss) seen along the magnetic field lines. Therefore the material could not come from the corona, as there is not enough mass to supply the prominence. The mass of a large quiescent prominence is estimated to be about 10% of the entire mass of the corona so unless the mass flow circuit is closed through the

chromosphere the corona would be completely used up after a dozen prominence eruptions; the large prominence mass must come from the chromosphere, because there is not enough plasma in the corona (Tandberg-Hanssen, 1974; Aschwanden, 2006). The prominence plasma flow is therefore dynamic, with horizontal and/or vertical motions from the chromosphere which can continuously change the amount of cool material in the filament (Kilper et al., 2009). This process of mass movement from the chromosphere is carried out either through magnetic reconnection (below the prominence or at the footpoint) which injects or lifts cool plasma directly into the corona as in Figure 32 (diagrams 1 and 2), or through thermal (heating) pressure forces, diagram 3, which evaporate heated plasma which then condenses onto prominence threads (Mackay et al., 2010).

Coronal Condensation / Levitation Model

This model depends on the “levitation” of material lifted from the chromosphere by low lying dips in the prominence, either by relaxing loops in the prominence, flux ropes emerging through the chromosphere or after reconnection of loops in the chromosphere that then rise (Kilper, 2009). Priest & Smith (1979) modeled prominences as stretched out loops where thermal conduction becomes ineffective, so that radiative cooling dominates and forms cool prominence plasma (Aschwanden, 2006). The low density and high magnetic field strength (~ 10 G) in the corona results in the magnetic field pressure dominating gas pressure, so charged particles must move mostly along field lines (Kilper, 2009). The coronal condensation-levitation model as shown in Figure 33 proposes that cool plasma is lifted by rising magnetic fields at the PIL and transported transverse to the magnetic field (Mackay et al., 2010). Lites & Low (1997) suggest photospheric material is dragged up into the corona through the levitation process as a horizontal flux rope emerges.

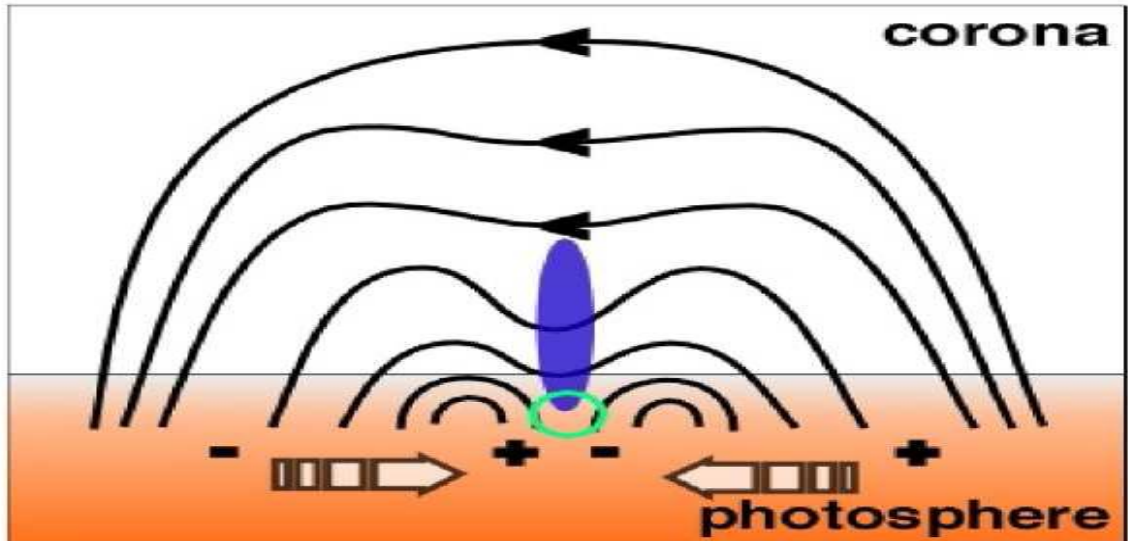


Figure 33: Illustration of the coronal condensation/levitation of plasma (Blue) by U-loop (dips). Image credit: Mackay et al., 2010.

In the levitation model the filament channel magnetic structure is a highly twisted flux rope that brings up cool plasma as the axis and lower portions of the rope appear above the photosphere, placing the prominence plasma in the U-loop dips of the helical field (such as the K-R model) (Rust and Kumar, 1994). The flux rope, according to this model, is either created from a magnetic arcade that is sheared by solar differential rotation, where flux cancellation and reconnection creates the loops in the flux rope, or a buoyant flux rope is created at the tacholine and then rises through the convection zone and photosphere up into the corona (Rust and Kumar, 1994). Once the structure has formed, chromospheric material can rise up through the ends, cool, and then settle into the series of dips in the flux rope.

Another lifting mechanism is the relaxation of magnetic fields during flux emergence resulting in dipped U loops, where the condensation sits, after reconnection from flux cancellation (the K-S model) (Mackay et al., 2010). However, most of the

uplifted cool plasma drains along the rising field lines onto the chromosphere and how this process can lift photospheric or chromospheric material into the corona also has not been explained (Mackay et al., 2010). Aschwanden (2006) reported that flux emergence simulations have shown that emerging U-loops and the associated photospheric plasma do not easily break through the photosphere or rise to coronal heights seen in quiet Sun and intermediate prominences, even without a preexisting coronal field. Even though the U-loops of the emerging tube do not rise to coronal heights, the process of flux emergence may still produce a coronal flux rope with dips (Aschwanden, 2006). A flux rope could form through the reconfiguration of sheared field lines that lie above the emerging tube's axis or through helicity injection (Aschwanden, 2006). Once the tube is formed above the photosphere, it can rise to coronal heights, dragging cool photospheric or chromospheric plasma with it (Mackay et al., 2010). This process of flux emergence and then flux cancellation may occur for active region prominences but Mackay et al., (2010) state it is not likely for quiescent or intermediate prominences. Van Hoven et al., (1992) report the results of a model simulation of the formation and support of a narrow prominence at the apex of a coronal magnetic loop or arcade. The condensation process starts with an initial radiative cooling and pressure drop, with a secondary *siphon flow* from the dense chromospheric ends. As the dense prominence forms, it causes a bending of the confining magnetic field, between the semi-rigid ends of the magnetic loop forming a wide magnetic 'hammock' or well (K-S-type) that supports the prominence at or near the field apex. The footpoint motion driven energy imbalance leads to radiative cooling of plasma at the apex. Because of the pressure drop mass is siphoned into the corona pulling more plasma to the apex. As the density at the apex rises the radiative energy loss reduces the thermal pressure

and draws more mass from the chromosphere. The resulting bending of the local supporting field continues to cause the mass inflow to levitate and condense in the U-loop (Van Hoven et al., 1992).

Siphon flows can drive material upwards if there is a large enough positive pressure difference between the chromosphere and a dip near the apex of a coronal loop (Antiochos et al., 1999). The main problem with these models is that most of the uplifted cool mass tends to drain along the rising field lines onto the chromosphere (MacNeice et al., 1999; Kilper et al., 2009). The ability of this model to lift photospheric or chromospheric material as high as 100,000 km into the corona also has not been shown. Simulations of the reconnection levitation mechanism have shown that rising field lines are produced by reconnection between bipolar systems, but it still must be proved that this is what causes the observed motions and properties of prominence plasma (MacKay et al., 2010).

Injection Model

In the "injection model" material is driven up the legs of the prominence by magnetic reconnection low in the solar atmosphere (Chae et al., 2003; Kilper, 2009). The cool plasma is forced upward in filament channel flux tubes with enough force to reach the tops of the prominence by reconnection low in the solar atmosphere. See Figure 34 for a diagram of the Injection model. The injection or upflow model suggests that photospheric or chromospheric mass is injected (upflowed) with enough speed at flux cancellation/reconnection points, either at or away from the PIL, for mass to rise into the corona at or near its original cool temperature (Mackay et al., 2010).

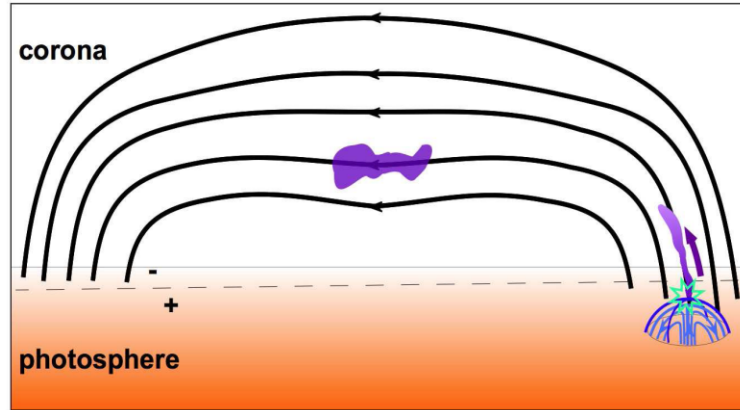


Figure 34: An illustration of injection of plasma (purple) by reconnection between minority-polarity bipole (blue lines) and pre-existing filament-channel field (black lines). Image credit: Mackay et al., 2010.

In other models, an unspecified mechanism is assumed that produces a ballistic injection with some initial velocity, which may explain surge like upflows (Aschwanden, 2006). Because injection causes unidirectional upflows in each flux tube, counter streaming could result through reconnection at the bases of different flux tubes on opposite sides of the PIL or through reconnection at each footpoint (Mackay et al., 2010). Many active region prominences have jets which may come from reconnection events, and could be explained by injection (Mackay et al., 2010). Prominence barbs also might be explained by the injection of cool plasma by reconnection between the filament channel field and small bipoles emerging in the channel (Mackay et al., 2010). The injection model, however, does not explain how cool plasma appears suddenly in the corona so often and the mainly horizontal fine scale counterstreaming flows in quiescent prominences and how reconnection can drive cool filament channel material to such high heights in the corona, as high as 100,000 km, without also heating the plasma (Mackay et al., 2010). Another issue is whether cancellation reconnection occurs in or below the chromosphere; if the interacting flux systems reconnect instead in the low corona, then cool dense plasma will

not be lifted or injected directly (Mackay et al., 2010). Cancellation seen in the photosphere or chromosphere does not necessarily mean that the associated reconnection site is at the same level (Zwaan, 1987).

Evaporation-Condensation /Thermal Non-Equilibrium Model

Other models suggest that prominence mass can be lifted into the corona either by magnetic forces during flux emergence, or by gas forces due to siphon flows. The magnetic levitation model does not seem to be able to supply prominence mass because the mass is seen to flow downward from the corona onto the chromosphere, not upward (Engvold, 1976). In the evaporation-condensation model, proposed by Antiochos & Klimchuk (1991) localized heating near a footpoint causes chromospheric material to rise into the prominence, and then radiatively cool and condense near the middle of the structure. This model is based on the fact that adding heat to a coronal loop increases the density of the corona while decreasing slightly the chromospheric mass. See Figure 35 for an illustration of the Evaporation-Condensation model. Antiochos and Klimchuk (1991) modeled a prominence that heated the loop near a footpoint causing the plasma to rise into the loop and as the density increases it cools more rapidly and forms the condensation. Other studies focused on the cooling of the hot plasma by decreasing coronal heating rate; when the heating stops most of the loop mass drains back onto the chromosphere. Antiochos and Klimchuk (1991) proposed heating at the footpoint away from the midpoint of the loop. By doing this they found that the midpoint initially heats up but then collapses and cools to chromospheric temperatures by evaporation leaving condensation in long loops; they concluded that condensation can form as a result of a heating *increase* instead of a decrease as proposed by other models (Antiochos and Klimchuk, 1991).

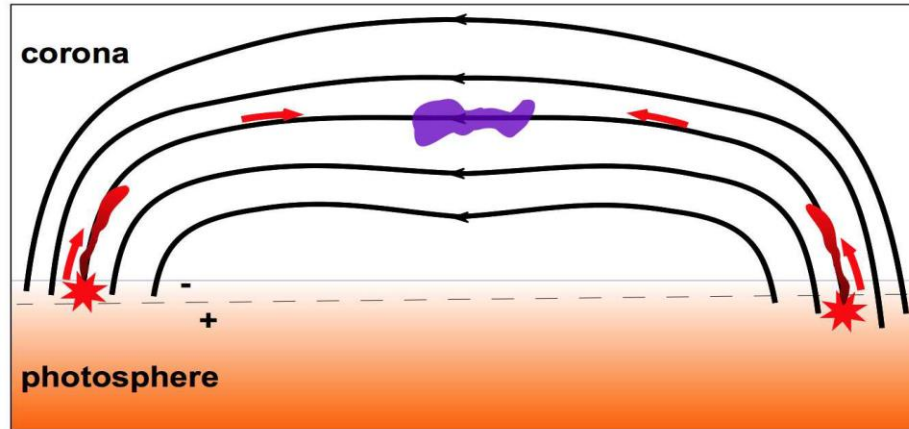


Figure 35: The Evaporation-condensation model: hot up-flows (red) is forced upwards by heating at above the footpoints which evaporate plasma that eventually condenses in the corona as cool prominence material (purple). Image credit: Mackay et al., 2010.

The concept is that if the heating scale is small compared to the length of a coronal loop and localized near the chromospheric footpoints, then the plasma in the middle of the loop, where there is no heating, must undergo a radiatively driven thermal collapse to low chromospheric temperature to reach equilibrium again which results in condensation forming (Antiochos & Klimchuk, 1991). This process does not need dipped flux tubes, which the magnetic structure models always contain although the dips can help maintain the cool plasma (Mackay et al., 2010). Poland & Mariska (1986) in a study used a heating mechanism at both footpoints to drive the upflows. A one-sided reduction of the heating rate by approximately 1% was found to be enough to cause condensation at the loop top and cause a pressure difference at the footpoints to drive a siphon flow. Once the condensation at the loop top starts, it stabilizes the prominence against fluctuations of the footpoint heating rate. They showed that by heating concentrated at the footpoints lead to condensations of coronal plasma in the dips of the near-horizontal segments of coronal loops or even in loops without dips (Karpen et al., 2001). Although dips were usually

considered to be a required condition for the stability of prominences, equilibrium is not necessary because of the dynamic nature of prominences, i.e., the observations of counterstreaming flows (Zirker et al., 1998). Prominence plasma is never in equilibrium as it undergoes continuous cycles of formation and then destruction of condensation knots (Antiochos et al., 2000a). Condensations form, move along the loop, and finally fall onto the chromosphere in a continuous cycle. This helps to explain why no supermassive condensations are seen in quiescent prominences (Antiochos et al., 2000a). Antiochos et al. (2000a) explains that since some prominences can live for months, condensations could form that would take up most of the dipped field section which could be tens of thousands of kilometers long. But because any change in the loop heating is expected to push condensations out of the dipped field region, they do not grow too large. The thermal non-equilibrium (condensation-evaporation) model not only grows condensations in the Sun's corona, but it grows them the “right size” (Antiochos et al., 2000a). The problem with this model is that it cannot explain how this could work for active region prominences which are too short to support the thermal non-equilibrium /evaporator-condensation process with typical values of the heating scale, or of the vertical structure of hedge-row prominences (Mackay et al., 2010).

Prominence/ Filament Eruption

Martin et al., (2008) propose that filament eruption is a result of a complex process that begins with a filament channel with canceling magnetic fields, i.e., magnetic reconnection at or close to the photosphere along a PIL. The reconnection transfers magnetic flux from the photosphere into the chromosphere and corona along the PIL building the filament channel. The magnetic flux transported upward from the

photosphere/chromosphere carries plasma into the corona along the filament magnetic field. However, the flowing and counterstreaming filament mass also slowly drains out of the field leaving behind new strands of cavity magnetic field with little mass. When the buildup of magnetic pressure in the filament and cavity magnetic fields becomes greater than the overlying coronal loops, the coronal loops, the filament and the cavity together begin a slow rise, which can last for a few hours to many days before quickly rupturing with a solar flare. Martin et al., (2008) suggest that the process can be accelerated by external triggering mechanisms.

The formation of a filament is driven by flux convergence and cancellation, which produces loop-like filament segments with a half-turn. Filament segments of the same chirality may connect and form long quiescent filaments adding some helicity to the filament. This linking of filament segments of the same chirality may be repeated many times over the lifetime of a filament. Very long filaments can be formed this way. Each time footpoint anchored legs and arches are added to the filament configuration through cancellation, it increases helicity (Martens & Zwaan, 2001). A magnetic flux tube will become unstable when the number of field line winding turns exceeds a certain maximum; only a few turns are necessary before the flux tube becomes “kink-unstable” (Martens & Zwaan, 2001). Probably only one or two pairs of footpoint ends need to be completely removed through cancellation for the filament system to become kink-unstable and Martens & Zwaan (2001) and Martin & McAllister (1997) conclude that the same mechanisms, i.e. convergence and cancellation that drive the formation of filament/prominence systems may, because of excess helicity, cause eventual filament eruption and then filament reformation.

The overall helical magnetic structure of a prominence can become very visible during activation and the eruption. During activation the originally quiescent prominence changes to where plasma visible in $H\alpha$ fills up more of the helical magnetic configuration and increases the number of windings destabilizing the filament (Martens & Zwaan, 2001). The eruption is caused by the kink instability, which begins when the amount of magnetic twist in the flux tube exceeds a critical value: as the number of turns increases, eventually the threshold for kink instability is exceeded and the filament may erupt (Martens & Zwaan, 2001). Welsch (2006) suggests that CMEs remove non -potential, helicity carrying flux systems from the corona out into space, removing the erupting volume of magnetic helicity. This allows the magnetic field in the erupting region to relax to its global energetic minimum, the potential state. Reconnection without eruption can release some of the corona's free energy, but eruption with reconnection can release all of the free energy (Welsch, 2006).

Some Open Issues for Future Research

Mackay et al., (2010) points out that a major challenge of prominence research is to determine how to resolve the different structures observed in the same filaments and prominences when seen on the disk versus the limb. How can filaments and prominences be more easily compared since they are essentially the same phenomena but when the filament becomes a prominence as it approaches the limb it appears different. Even though prominences are simultaneously observed in He II 304Å and $H\alpha$, and are known to lie in the same magnetic configuration, they often look so dissimilar in different wavelengths and appear to have different topologies (Mackay et al., 2010). Filament plasma seen in absorption on the disk may not be exactly the same as the prominence plasma seen above

the limb a few days earlier. One problem in comparing filaments and prominences is that the fine structure changes continually with time (Mackay et al., 2010). Also, active region filaments usually are at such low heights (less than 100,000 km, the approximate height of the spicule forest) that they are hard to see at the limb. Some prominences can be clearly seen in He II 304Å above the limb, but may not be so easily visible on the disk because of plasma velocity, temperature and density changes which may explain why prominences do not seem to have the same characteristics as filaments when they cross the limb (Mackay et al., 2010; Labrosse et al., 2010). Mackay et al. (2010) suggests that it would be of benefit if images with high spatial resolution of filaments and prominences were taken simultaneously at different wavelengths to track the same filament as it moves across the solar disk and above the limb.

Labrosse et al. (2010) noted that there is a consistent pattern seen in filaments observed against the disk where vertical motions appear in barbs and horizontal ones appear in the prominence spine. Labrosse et al. (2010) suggest that further research is needed to determine the relationship. What is the relationship between observed H α and EUV motions; are these different components or are they features of the same motions? EUV motions seem to be faster than those seen in H α ; is this correct (Labrosse et al., 2010)? Certainly further research is needed to determine the magnetic structure of prominences. Several models and theories have been proposed on how magnetic fields are formed (e.g. sheared arcade versus flux rope) and where prominence plasma comes from, but the actual mechanism is still unknown. How does cancelling magnetic flux and helicity cause a prominence to grow and what sparks an eruption remain unknown with no definitive answers.

CHAPTER II METHODOLOGY

Purpose

The purpose of this study is to report the different (and similar) morphology when comparing Extreme Ultra Violet (EUV) data from the Solar Dynamic Observatory's (SDO) Atmospheric Imaging Assembly (AIA) He II 304Å with data from the Dutch Open Telescope (DOT) H α at the 656.27nm centerline, as well as the 656.23nm (blue shift) and 656.31nm (red shift) emission lines. Two prominences have been selected for this study; the first a northeast low lying prominence (N53E90) and the second a very active northwest prominence (N33W90).

H α and He II 304 Å show similar prominence/filament structure even though their emissions appear at drastically different temperatures. H α tends to show cooler (~10,000K) lower region prominences located in the chromosphere and He II 304Å show hotter (~80,000K) emissions located higher in the upper chromosphere and into transition region. This comparison of a simultaneously observed prominence from two different systems will provide data that can be combined to enhance the information and knowledge of this phenomenon. By understanding the advantage of each wavelength a more complete picture can be determined in future studies in order to understand filaments and prominences in their entirety. It is important to identify different and similar morphologies to understand

why certain structures can appear in one observation and not the other and why structures sometimes appear in both observations.

Hypothesis

Simultaneous observations using data from both ground-based (DOT) and spacecraft images (SDO) found strong 304\AA emissions in the hotter outer portion of a prominence and strong $H\alpha$ emissions in the relatively cooler lower segment. The details revealed in the $H\alpha$ images are superior in terms of structural detail when compared to 304\AA images; however, there is benefit in using both methods to provide a more complete picture of the properties, structure and evolution of a prominence.

Observations

The wavelength 304\AA (30.4nm) represents He atoms that are ionized to form He II ions which emit EUV radiation. EUV radiation is blocked by the Earth's atmosphere so it is only possible to observe from spacecraft such as SDO. He II ions emit temperatures ranging between 60,000K, in the upper chromosphere, up to a peak of 80,000K (Waltham, 2012). The brighter areas seen in this wavelength are places where there is a high plasma density.

The $H\alpha$ wavelength is located in the visible red spectral line at 6562.8\AA (656.28nm). Hydrogen can emit in the ultraviolet spectrum which is considered the Lyman series but Hydrogen can also emit in the visible part of the spectrum which is called the Balmer series. When the electron orbiting the H atom jumps from the third down to the second lowest energy level, a photon is released and this is observed at a wavelength of 6562.8\AA , which located in the red part of the visible spectrum. $H\alpha$ has a formation

temperature of about 6,000K to 11,000K (Wang, 2002). By viewing the Sun in the $H\alpha$ wavelength, much of the photosphere is eliminated allowing the chromosphere to be seen.

The Dutch Open Telescope

The Dutch Open Telescope (DOT) is a ground based solar optical telescope built in 1997 and located in the Canary Islands off the coast of Africa. It is a 0.45 meter reflecting telescope equipped with a 10x enlargement lens system and a 2 meter focal length. The telescope and the tower have an open framework concept which means that the wind can pass by with little resistance in order to reduce oscillations in images. The wind is able to pass through the system including the primary mirror, so that no internal turbulence develops and a constant temperature is held to prevent seeing (Rutten, 2012). This open concept was very innovative at the time and it was designed and built by R.H. Hammerschlag (Rutten, 2012). The seeing at the high-latitude location is extremely good at about 0.4 arcsec (Vernin, 1992).



Figure 36: The Dutch Open Telescope on La Palma (Bettonvil, 1999)

Cameras

The Dutch Open Telescope is equipped with seven scientific cameras, each with a different filter; Calcium (3968.7 Å), G-Band (4305 Å), Blue Continuum (4319 Å), Barium (4554 Å), Barium Continuum (4504.8 Å), Red Continuum (6550.5 Å) and H α (6562.8 Å). All cameras and their filters can be used simultaneously. Some filters, such as H α , are tunable which allows users the ability to take images at different wavelength positions of an emission line.

The camera used for the H α filter is a Redlake ES4020 (Rutten, 2012). It has an image pixel scale of 0.11 arcsec/pixel and covers a field of view of 113 x 113 arcsec. Its tunable range is between 6562.0–6563.6 Å. The camera has a cadence of 30 seconds and the time difference between images taken on the center line, blue shift and red shift is about 4 seconds. This delay is the time it takes to apply voltage to the filter. DOT as well as SDO use the image file format FITS.

FITS files stand for Flexible Image Transport System and was designed to create a standard medium in order to interchange astronomical data between observatories (Allen, 2005). The benefit of using FITS files is their archival and metadata storage ability. Inside a FITS file there is a stored header containing information about the image, such as the date and time of the observation, right ascension and declination of the target and other observational and instrument parameters. The DOT images are typically 2MB and SDO's full disk images are 32MB each.

DOT Data

The H α data used for this study was imaged by DOT's H α camera on October 31, 2010, between the times of 11:49 – 17:47 UT. It includes three different wavelengths: the

centerline at 6562.7\AA , a blue shifted set at 6562.3\AA , and a red shifted set at 6563.1\AA . The images have had flats pre-applied.

There are 628 FITS files per wavelength spanning 8 hours. During this time there are two prominences of interest. The first is a north east prominence off the limb of the Sun at the coordinates N53E90. This prominence was imaged between the times of 11:49-12:49 UT. The second is a north west prominence at N33W90; it was imaged between the times of 13:08-17:46 UT.

There is a gap of images during the observation of the NW prominence in the DOT data; this is due to the adjustment of the viewing location, refocusing, and taking flats. The gaps are between the times of 14:07-14:29 UT, 14:30-14:36 UT and 16:42-16:47 UT. Between all DOT images there is a slight amount of oscillation and out of focus frames due to the oscillation and the effects of atmospheric seeing.

Solar Dynamic Observatory

NASA's Solar Dynamic Observatory (SDO) is the first mission to be launched for the Living with a Star Program (Waltham, 2012). The LWS program is designed to understand the causes of solar variability and its impacts on Earth (Pesnell, 2012). SDO's mission is to study the Sun's influence on Earth by looking at the solar atmosphere in several different wavelengths simultaneously. It was launched on February 11, 2010, on an Atlas V rocket and has mission duration of 5-10 years. After a series of orbit-raising maneuvers, SDO eventually settled into its geosynchronous orbit at an altitude of about 36,000 km. (Pesnell, 2012). Choosing a geosynchronous orbit is beneficial because it has a constant downlink capability. The downside to this type of orbit is that SDO experiences

eclipses when the Earth and the moon passes between the satellite and the Sun twice a year for a few weeks. This causes a loss of 44 hours each year (Pesnell, 2012).

SDO is equipped with three instruments; the Helioseismic and Magnetic Imager (HMI), the Atmospheric Imaging Assembly (AIA), and the Extreme Ultraviolet Variability Experiment (EVE). The AIA contains seven different extreme ultraviolet (EUV) channels which image the solar corona simultaneously at a resolution of 1 arcsec and a high cadence of 12 seconds (Waltham 2012). The EUV temperature range of the AIA covers a range between 6×10^4 K to 20×10^7 K. (Waltham 2012). The 304\AA (30.4nm) channel represents the chromosphere/ transition region by filtering Helium II ions. The camera used has a 41×41 arcmin field of view with an image pixel scale of 0.6 arcsec/pixel. Processed AIA data are made freely available for public access through a search form on the Virtual Solar Observatory website. By selecting the date and time, wavelength and cadence, the raw FITS file images become available for download. There are over 1950 images needed for this study.

Calculating the dimensions of a prominence

In order to obtain accurate size measurements it is important to understand the scale being used. The average semi-major axis of the Earth to the Sun is about 149,597,887.5 km with a minimum distance of 147.1×10^6 km and a maximum distance of 152.1×10^6 km (National Aeronautics and Space Administration, n.d.). The Sun's equatorial diameter is approximately 1,392,000 km (National Aeronautics and Space Administration, n.d.). By using the equation $2\pi r$, where r is the radius of the Sun, the circumference of the Sun can be solved to equal 939,951,248.76 km. In order to convert this from km to arcsec it needs

to be divided by degrees (360), minutes (60) and seconds (60). $939,951,248.76 \text{ km} / 360^\circ / 60' / 60''$ results in 1 arcsec on the sun being equal to $\sim 725 \text{ km}$.

The plate scale of DOT's H α camera is about 0.11 arcsec/pixel. Therefore one pixel in a DOT H α image is the equivalent to $\sim 80.08 \text{ km}$. SDO's AIA produces a 4096x4096 pixel image with a 41 arcmin field of view (Pesnell, 2012). Therefore the angular resolution is 0.6 arcsec (2460 arcsec/4096 pixel resolution). By using the same method as before each pixel in an SDO image equals $\sim 436.8 \text{ km}$.

The prominences used for this study were observed on October 31, 2010. Although the times taken are the same, the viewing angle at which these prominences are observed are different. All measurements taken will be line of sight and it will be assumed, for model making purposes, that the location of each prominence is crossing the limb.

Calculating the speed of mass motions

To estimate the speed of plasma flows of a prominence requires manipulation of data. Because the images used are 2D, it is possible to measure the height and width of a prominence, but it is not possible to estimate depth. Any speeds calculated in this study will be estimated unobstructed line of sight to a 2D plane where the prominence is observed. There will be an unknown in estimating the movement in a depth or Z-axis direction which can sometimes be an essential part of mass motions such as when estimating speeds of red shifted or blue shifted moving material. When viewing mass motions image by image it can be difficult to identify directions and speeds. By creating aligned movies and playing them at slower speeds mass motions can be more easily observed.

Figure 37 below shows how speeds are estimated in a DOT 2D image. The start time, 12:20 UT, and location of a mass is identified and marked inside the green circle. By watching frame to frame it is possible to see the mass moving and its direction. Once the path of movement is complete the time is noted, 12:38 UT. The blue line represents the path the motion has traveled which is about 162 pixels long. 162 pixels is ~13,000 km. It took the mass about 17.5 minutes (1050 seconds) to move between the start location and the end location, therefore $13,000 \text{ km} / 1050 \text{ seconds}$ equals an estimated speed of ~12.8 km/s.

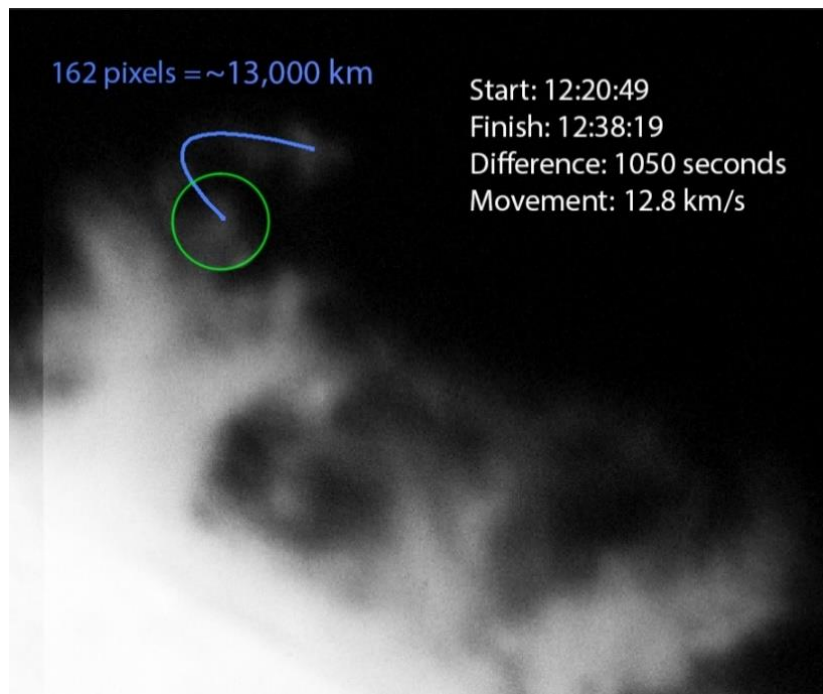


Figure 37: An example of how velocity of a mass is estimated. By marking the start time and location, path of motion, and end time and location, an average velocity can be calculated. The mass moved 13,000 km in 1050 seconds which results in a speed of ~12.8 km/s.

CHAPTER III

RESULTS

Northeast Prominence (N53E90)

The first prominence was observed on October 31, 2010, from 11:49-12:49 UT.

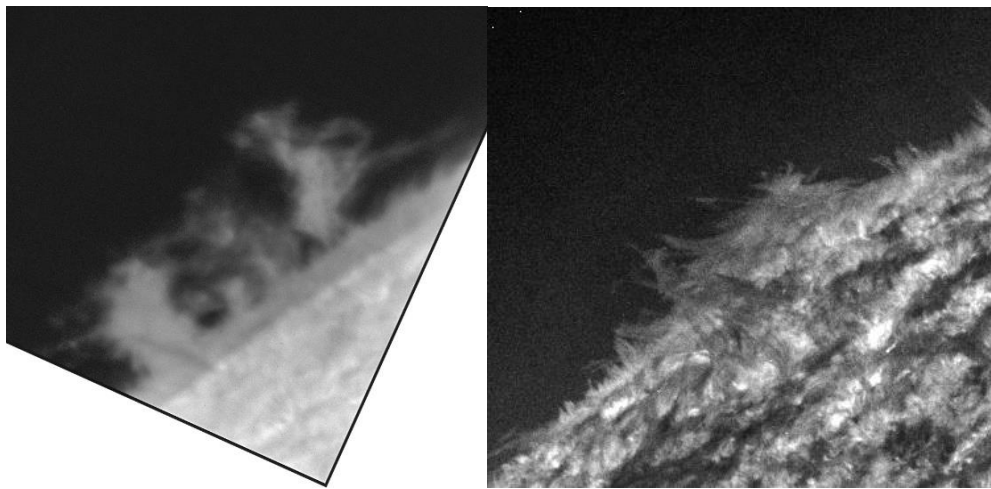


Figure 38: North East Prominence. Left: DOT's $H\alpha$ prominence, Right: SDO's 304\AA the same time.

The DOT $H\alpha$ images suffer from atmospheric distortions and oscillation issues causing the images to have a reduction in clarity. The oscillation effects cause the images to shift every frame which have been aligned to mitigate this but there are still flaws which can cause small errors. Because SDO is a spacecraft its images don't have issues with atmospheric distortions and focusing issues, the clarity is always optimal. The resolution of the DOT telescope is about 0.4-0.5 arcsec while the SDO spacecraft has a resolution of about 1 arcsec. During the hour of observation the prominence appears to change very

little. The prominence studied is a low lying quiescent prominence because it is not located near any apparent active regions. Its shape is a hedgerow prominence as it is composed of many quasi-vertical threads (Tandberg-Hanssen, 1995). The prominence appears to have a similar shape in both wavelengths but there are some obvious differences. The H α image shows more detail in terms of characteristics of the prominence while the 304 Å images just appears as one massive mound. Although this area is cropped out of the H α images, this extension is not seen or indicated in the H α images. This material could possibly be too hot and too high up in the chromosphere to be seen in H α but it does indicate that the prominence is larger than it appears in H α .

DOT's H α NE Prominence Analysis

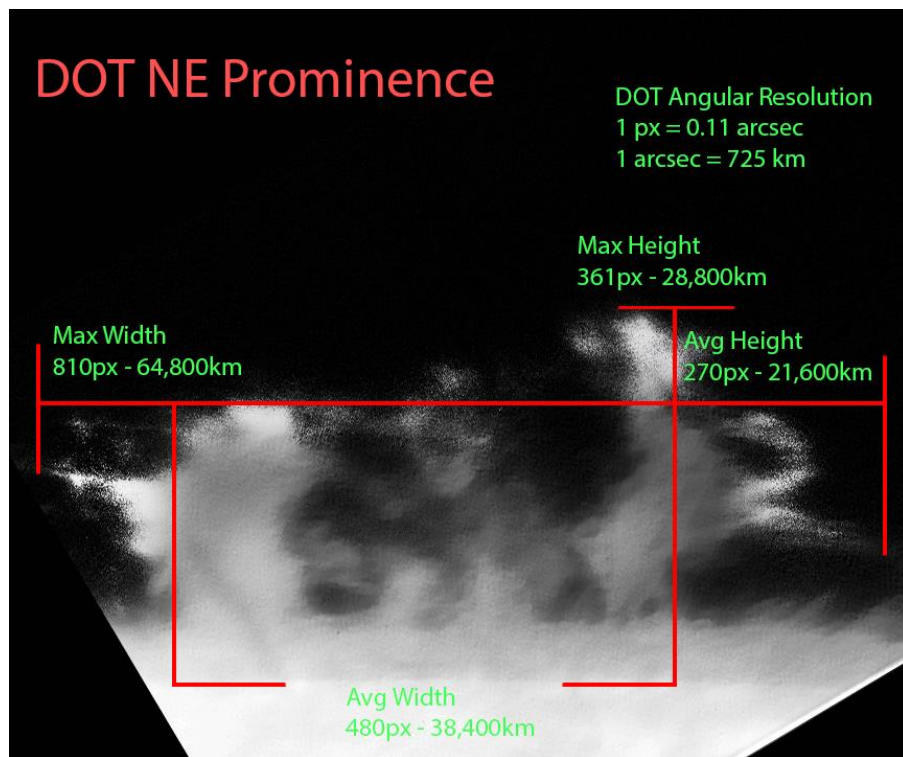


Figure 39: DOT NE prominence dimensions. The prominence was rotated clockwise. The outer edges were brightened and over saturated in order to see the faintest of material.

Since there are several different prominences making up this hedgerow prominence, several different measurements can be taken. As seen in Figure 39, the maximum height reached by any of the prominences is ~28,800 km off the limb. The average height of this entire cluster is around 22,000 km off the limb. The heights throughout the hour do not change much except in certain event areas which are expanded on later. The width can vary from 38,400 km to beyond 64,800 km where material either moves out of view or heats up to the point where it is no longer visible in the H α wavelength.

This prominence can be divided into three parts: the left side which is in the shape of a pillar or arch prominence, the center which has no discernable shape but appears to exchange material with the left arch prominence, and the right side which seems to be more independent but also exchanges material with the middle prominence. The right prominence shows movement and counter streaming in all directions making it difficult to distinguish its dominant direction, however there appears to be a counterclockwise rotation giving it the appearance of a tornado. An estimated average speed inside the right prominence is calculated to be ~14 km/s (Table 1, Speed 1). Dopplergram movies reveal blue shifted material moving to the left and the red shifted material moving to the right and all at approximately the same speeds.

The left prominence (broken arch shape) appears to be much thicker than the right one. It has a lower portion about 8,800 km wide and a top region that appears to split into three different directions over time. It begins as a broken arch prominence which exchanges material with the middle prominence but eventually it builds enough mass between the middle to be considered a single arching prominence; this becomes very apparent at 12:09

UT where it appears to have enough mass to create a spine connecting the two, as seen by the green line in Figure 40.

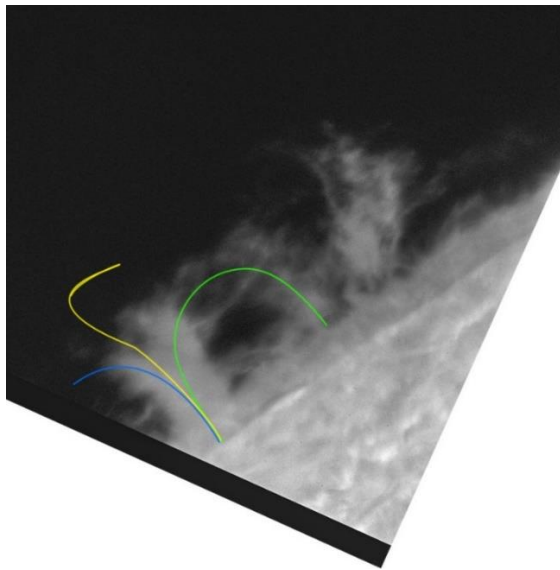


Figure 40: Three directions of NE prominence. The green line shows the connection to the center prominence creating a single prominence arch. The direction indicated by the Yellow line develops throughout the hour as material expels quickly over its top. The Blue line appears to be a result of a reaction to a fast moving material at the beginning of the hour.

SDO's 304Å NE Prominence Analysis

The SDO NE prominence is not clearly defined by its shape. Unlike the hedgerow shape appearance in the $H\alpha$ images it appears to look more similar to a mound prominence with more of a horizontal thread direction and it is 45° clockwise to the horizontal direction of the Sun. As seen in Figure 41 below, the average height measured from the limb of the Sun to the top of the prominence is about 20,000 km which is very similar to the average height off the limb seen in $H\alpha$. The differences can be due to the line of sight because of the orientation of each telescope. The limb of the Sun in the two wavelengths do not align perfectly either, 304 Å only shows material in the upper chromosphere and the transition region while $H\alpha$ shows material much closer to the photosphere.

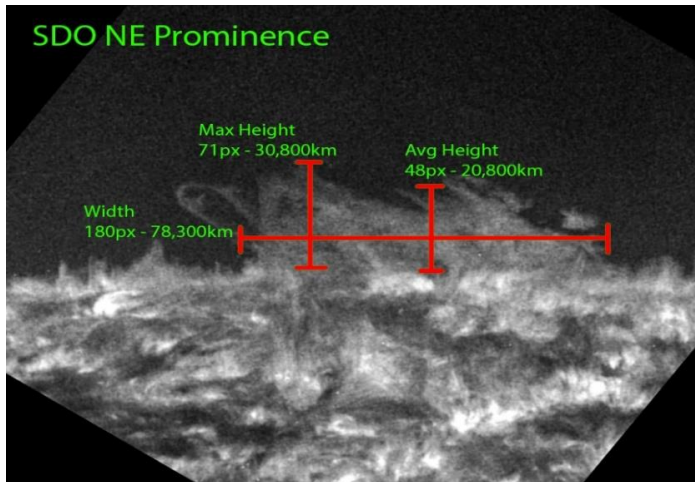


Figure 41: SDO dimensions of the NE prominence as seen in 304Å

When comparing the two views, there is a difference in width. $H\alpha$ indicates a width of 64,800 km while the prominence in 304Å indicates a width of about 78,300 km. Figure 42 shows how DOT's prominence aligns with SDO's prominence. There are key features in both the left side and the right side of the prominence that can be seen in both wavelengths. There are also masses seen moving in DOT images that can be seen in the SDO images (Event 1 and Event 2).

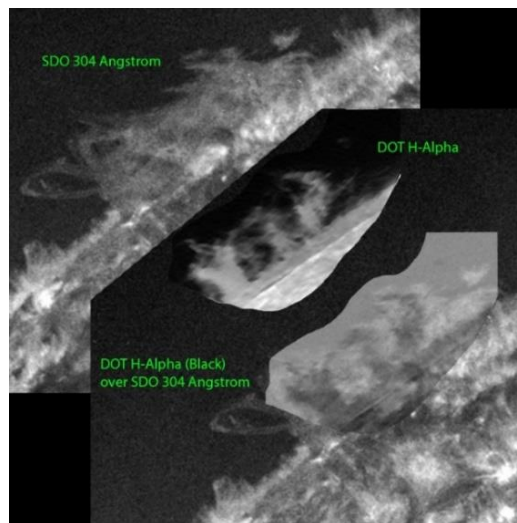


Figure 42: This figure represents how the prominences align. The $H\alpha$ image is inverted and overlaid on top of the 304Å image which allows both images to be seen.

The 304Å prominence in Figure 43 below, shows material over the disk of the Sun which indicates a possible footpoint, circled in green. The material on the disk appears to be cool as it is blending with the chromosphere which causes it to be very difficult to see. The spine of the prominence appears have a footpoint inside the highlighted green circle but no mass motions can be seen. The spine is actually seen because of its stationary appearance against the rapidly moving chromosphere. There is no evidence of this extension of material of the spine in the H α data.

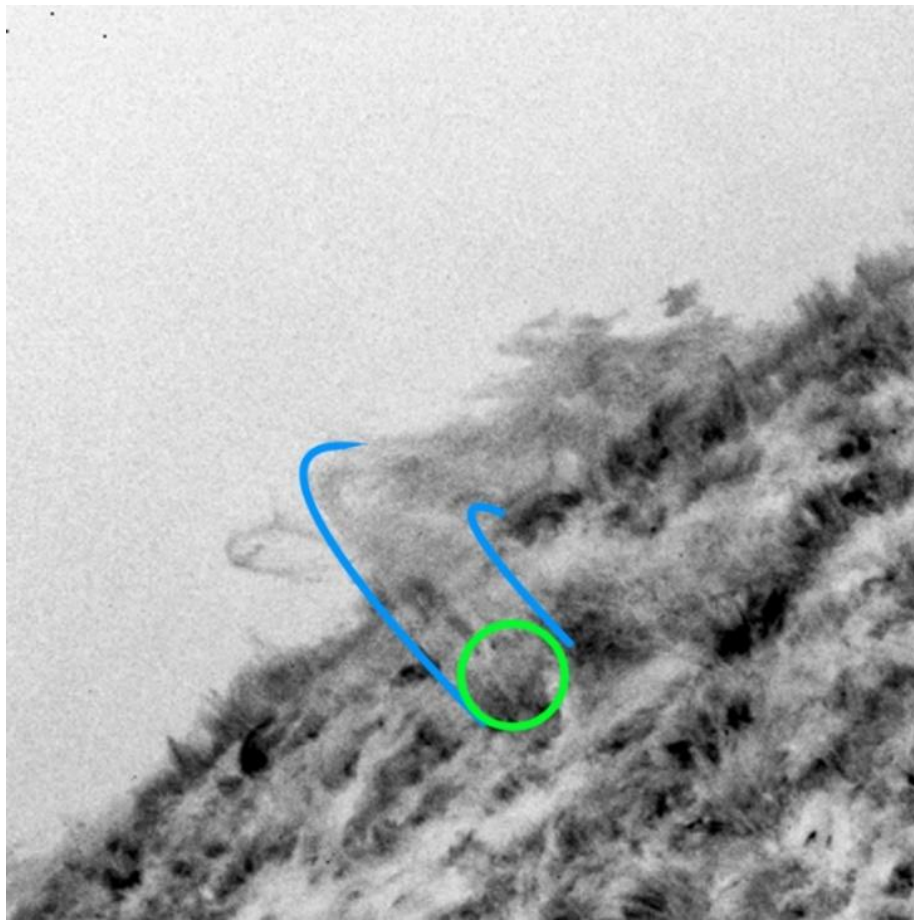


Figure 43: SDO prominence extending onto the disk. This inverted image of SDO shows how the prominence appears to extend onto the disk of the Sun. The blue line highlights the spine of the prominence moving from the disk over the limb and the green line shows where the indicated footpoint exists.

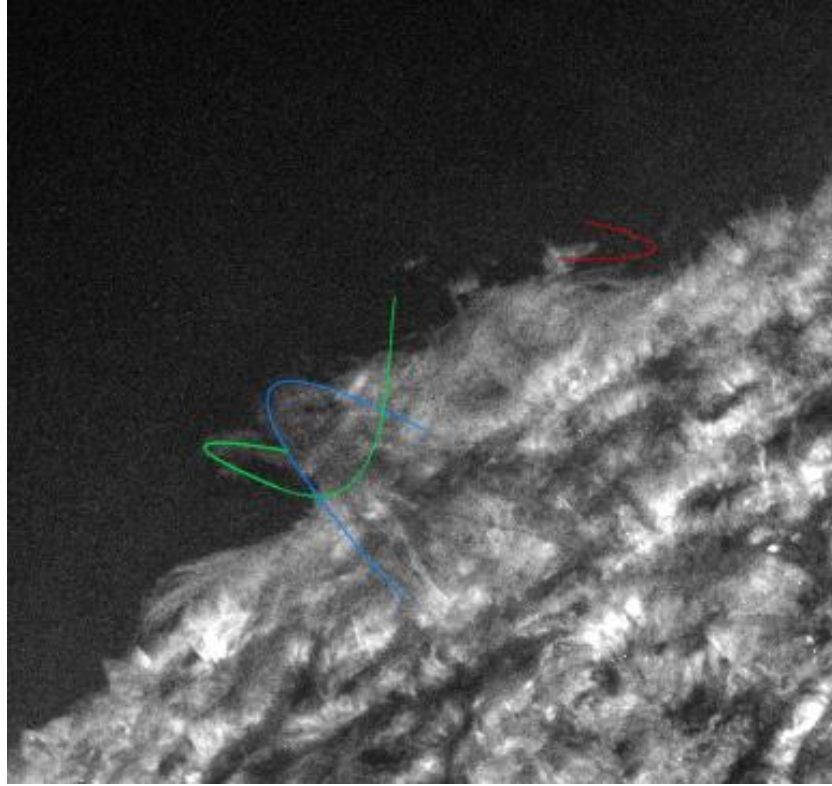


Figure 44: Event paths of the NE prominence. This figure displays two mass motions of interest. The blue line represents the arch of the prominence, the green line represents motion seen moving out and then under the main prominence. The red line shows a small mass which moves in a circular path back to where it first appeared.

The SDO images show a lot of motion in all directions, despite this, spines are not easily identified. The spine of this north east prominence can be seen on the limb, where a footpoint appears to be located. To the left of the prominence (green path) there is material that moves outwards and curves around 180° counterclockwise and moves back toward the surface. The material at this point could be passing behind the less dense material or in front of the prominence; it is not clearly seen but the material along the green path is visually observed moving along this path. Because the prominence appears too dense for material to be seen moving behind it, it is likely that the green path does flow under the main arch of the prominence. The red line shows an abundance of material forming at the

top right prominence and moves as one mass in a loop towards the surface rather quickly at ~ 21 km/s (Table 1, Speed 2) then when it reaches about 17,000 km off the limb it halts for about 10 minutes then continues slowly upwards toward where it first formed.

There are three events that occur throughout the hour which will be used in the comparison. The first event (green path in Figure 44) occurs in $H\alpha$ starting at 11:57 UT and only lasting about 30 minutes, in SDO this event can be seen lasting the entire hour. The second event involves a mass of material (red path in Figure 44) that moves in a counterclockwise direction. This mass is easily seen in 304\AA and starts at 11:50 UT where it continues until the end of observation at 12:49 UT. This mass is seen in $H\alpha$ although it is very faint at times. The third event (yellow path in Figure 44) is seen in $H\alpha$ and only barely seen in 304\AA . It starts at 12:21 UT and continues until the end of observations at 12:49 UT.

First Event- Plasma dip

In the DOT images at 11:57 UT there appears to be a dark thin cool streamer against the left side of the prominence, as pointed to by the yellow arrow in Figure 45. This streamer does not appear in either the red or the blue shift. It disappears early into the hour around 12:01 UT when material is ejected outwards at a speed of ~ 46 km/s (Table 1, Speed 3). The ejected material seen is bright and moving faster than the surrounding flow of material. It is ejected eastward at a $\sim 25^\circ$ angle to the surface of the Sun and becomes difficult to see throughout the hour due to the framing of the DOT images. The red shifted data indicates there is motion moving away from the observer and there is almost no motion in the blue shifted data providing further evidence of an away moving direction.

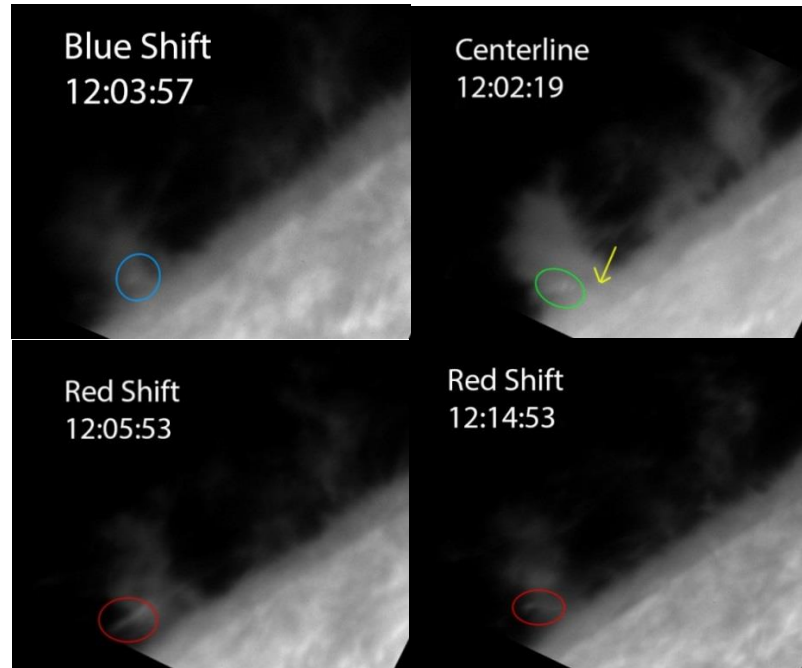


Figure 45: NE prominence event 1 H α . Material can be seen extending eastward at high velocity. It is easily seen in the center line and even more so in the red shift, it is not seen very well in the blue shift. The velocity taken from the red shift is ~ 46 km/s.

The 304Å images show this event slightly differently. In the H α images, there appears to be an ejection of material around 12:01 UT, but in the 304 Å images, material already appears to have been moving eastward at a $\sim 45^\circ$ angle to the surface of the Sun. As seen in Figure 44, the green line shows the path the material follows. It appears that the material observed in the H α centerline and redshift images correlates with the angle at which the material moves in 304 Å. As seen in Figure 46, the 304 Å images show the material moving outwards at $\sim 37,500$ km off of the limb of the Sun and reaching a height of $\sim 26,000$ km where it curves around, heads back towards the surface and continues parallel with it until it moves outwards once again. The total distance traveled is more than 110,000 km. The mass, although it is difficult to detect, can be seen in front of the prominence mound throughout its entire path. Its path appears to move underneath the left

prominence arch, this is unique as it means that there are magnetic lines moving perpendicular to and below the main arching prominence's magnetic line.

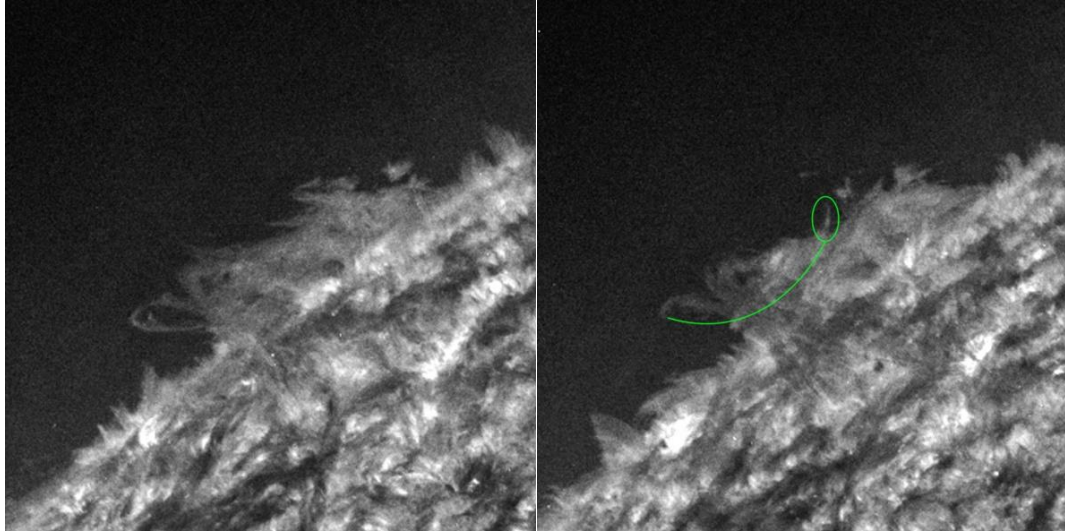


Figure 46: Mass traveled in event 1 in 304\AA can be seen throughout its entire path (green).

There is no evidence of this return path of material in $H\alpha$ in the red, blue, or center line images. This could be because the material is too hot to appear in the $H\alpha$ zone as it passes back through.

Second Event- NW mass of plasma

The second event begins around 11:54 UT in the 304\AA images. On the top right side of the prominence a mass of plasma becomes brighter than the surrounding plasma by heating up and then begins to follow a path identified in Figure 47a. It dips down towards the surface where it starts to blend in with the background plasma. At around 12:15 UT the mass can be seen rising once again upwards from the prominence where it hovers briefly and then continues on its path towards its original location. It is interesting that in the $H\alpha$ wavelength the mass cannot be seen until about 12:10 UT where it follows a similar path as seen in Figure 47b. In both wavelengths, the masses can be seen moving out of the right

side of the prominence around 12:10 UT where they continue to move identically in the same manner until the end of observing at 12:49 UT. The mass is very faint in the $H\alpha$ images but maintains the same movements as seen in the 304 \AA images. The mass is not seen in the blue shifted images and although it can be seen in the red shifted images, it is most easily seen at the center line. This indicates there is very little radial movement and that the mass is just moving vertically from the cameras line-of-sight.

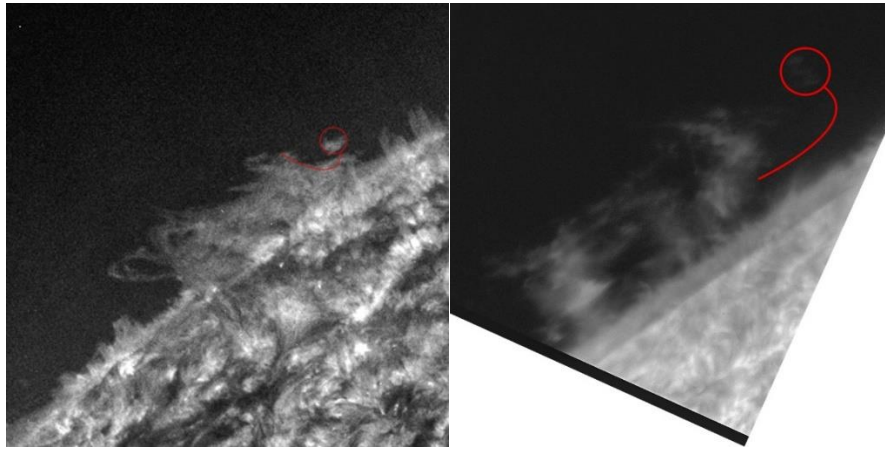


Figure 47: Event 2 NE prominence mass motion. a(left) b(right): The picture on the left is of 304 \AA and shows the mass moving from the top of the prominence down and back up. $H\alpha$ in the right image shows the mass moving out of the right of the prominence and moves vertically from the cameras line-of-sight.

The speeds in $H\alpha$ and 304 \AA were observed during the same time period of 12:10 UT to 12:24 UT. In the $H\alpha$ images the mass moves $\sim 18,000 \text{ km}$ resulting in a speed of $\sim 21 \text{ km/s}$ (Table 1, Speed 4). Observations in the 304 \AA during the same time period, the mass appears to move $\sim 16,100 \text{ km}$ and with a speed of $\sim 19 \text{ km/s}$ (Table 1, Speed 5). The speeds are very similar and this provides further evidence that the material observed in both image sets demonstrates the same mass flow patterns and follows the same magnetic fields. It is not possible to distinguish the motion observed in the beginning of the 304 \AA images at 11:54-12:10 UT in the $H\alpha$ wavelength. There is no indication that the material observed in

this event originates from the top of the prominence in any of the three sets of H α images. Rather, the material appears to originate from the side of the prominence where it then follows the same path as outlined in the 304 Å images. As the mass of material nears the top of the prominence, around the end of the observation period, there appears to be material in H α images which moves from the top of the prominence into the mass. It appears that the hotter, brighter material moves upwards. The reason for this is that when the mass first appears in 304 Å images, it is very hot and very bright, but as it moves at about 21 km/s (Table 1, Speed 2) down closer to the bottom of the prominence, it begins to cool slightly losing its brightness and its speed. This mass is much larger in 304 Å images indicating that the plasma in the mass is much hotter than can be seen in H α images. Although there is not enough data to watch the mass in the H α images, the mass can continue to be watched in 304 Å images. The mass can be seen moving higher up into the transition region about 50,000km line of sight from the limb where it slowly expands and eventually dissipating.

Third Event - Curl

The third event is best observed in the H α wavelength images. It follows the green curling path as seen in Figure 48 and starts at 12:20 UT at the top of the left prominence. The left side prominence at this point starts to split in the middle; its right side continues to exchange material over its arch towards the center prominence while the left side of the split begins to expel material leftward. From the middle of the split, material is being expelled quickly outward as it curves 90° clockwise. The material appears to curl when it reaches a height of about 28,000 km off the limb at around 12:33 UT. Material is still being expelled from the split of the prominence and, at one point, the material appears to slow

down slightly at its peak, however, with more material flowing towards it, the force pushes the material downward into a curl. The material begins to curl in on itself and become wrapped in a clockwise turning vortex. The distance the material in the curl travels is about 13,000 km and its speed around the curl is about 24 km/s (Table 1, Speed 6) on average.

The most amount of material visible is in the centerline images and the redshift images, but the blueshift images show very little motion except where the material is most dense. Between 12:41-12:44 UT in the 304Å images, there can be seen a small clockwise curl of brightened material. When observing the overlays, the timing and curl align at 12:41 UT. Although the start of the event in H α images occurs 21 minutes before any observations are visible in 304Å images, the same event is seen occurring at the same time once the material becomes hot enough to be seen in the 304Å images. The brightening in 304Å indicates that the material is hotter than the surrounding plasma, which is shown circled in a green circle in the right image of Figure 48b below.

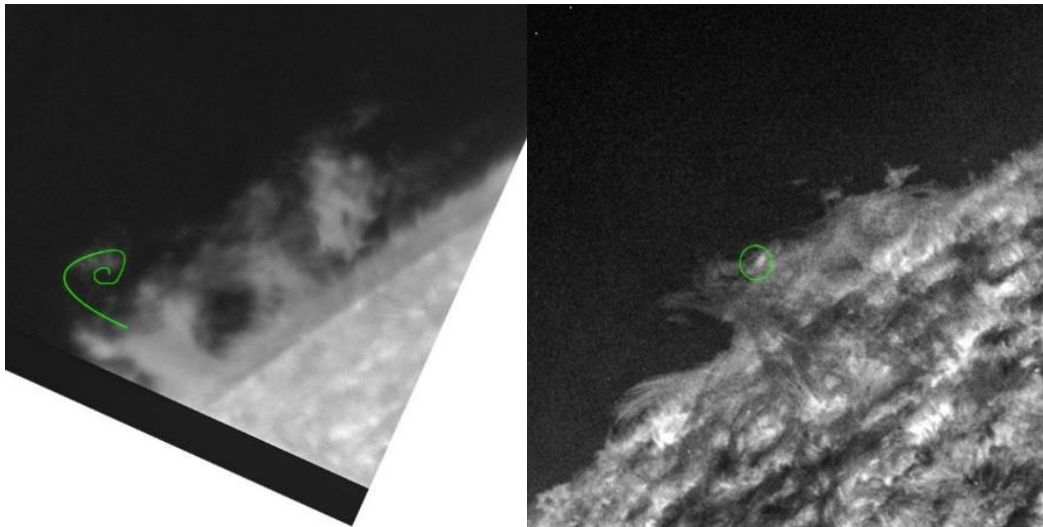


Figure 48: Event 3 curl- NE prominence. a (left), b (right): the left image is H α showing the clockwise curl the material follows. Right image is 304Å showing a small curl and brightening.

The North West Prominence N33W90

The second prominence was observed on October 31, 2010 between 13:08-17:46 UT. During the four and a half hours of observation this prominence's surroundings evolve considerably but the main pillar of the prominence remains relatively the same. This prominence is considered a broken arch in $H\alpha$ images and remains in this configuration the entire time although it does appear to increase in mass near the end of the observation period. However, the 304 Å images appear quite differently; it is an arching prominence to the right and to the left. Because the SDO 304 Å images can be cropped to a larger field of view more of this prominence can be seen. There are many extensions of the prominence visible in the 304 Å images, as seen in Figure 49. The main pillar is easily viewed in both wavelengths but there are many more barbs and footpoints seen in 304 Å images. There is an active region close by which noticeably interacts with the prominence when observed in 304 Å images.

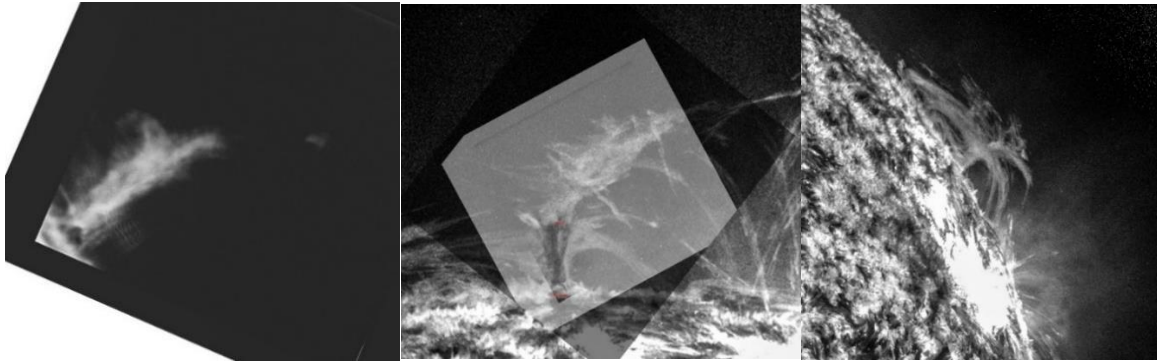


Figure 49: North West Prominence. Left: DOT's $H\alpha$ prominence, Right: SDO's 304Å, Center: An overlay with DOT as black and SDO is white

DOT $H\alpha$ NW Prominence

The prominence's dimensions in the $H\alpha$ images change considerably during the observation run. There is, however, a main pillar which keeps its rigidity the entire time

and only the mass around it changes. At the beginning of the observation period there is little material moving around the pillar; the dimensions remain at a height of about 60,000 km and a width of about 10,500 km, as shown in Figure 50. As this prominence becomes more active material can be seen moving faster and getting brighter and although the pillar maintains its width more or less, the height can be seen extending over 90,000 km off the limb of the Sun although the material appears to be scattered. The width of the main pillar remains approximately the same but material can be seen moving northward stretching its width beyond 12,800 km. The average calculated speeds of the material in the pillar prominence are about 23 km/s (Table 1, Speed 7). The incoming material that appears much higher around 70,000-90,000 km moves faster with speeds of up to ~50 km/s (Table 1, Speed 8), see Figure 51 below.

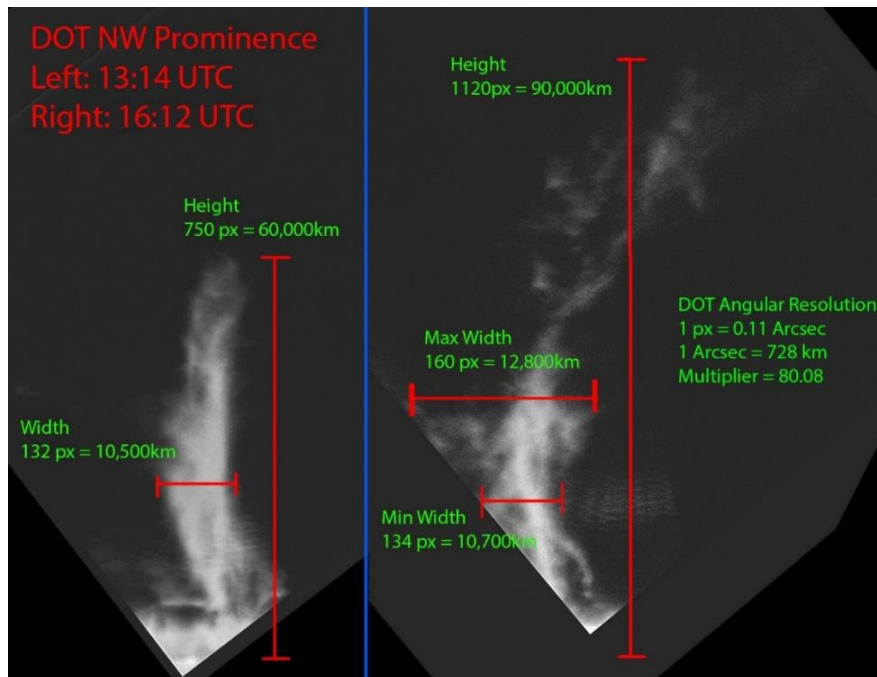


Figure 50: DOT NW prominence dimensions. The left picture is of the prominence at the beginning of the observation run around 13:14 UT. The right picture is of the prominence later in the observation run around 16:12 UT.

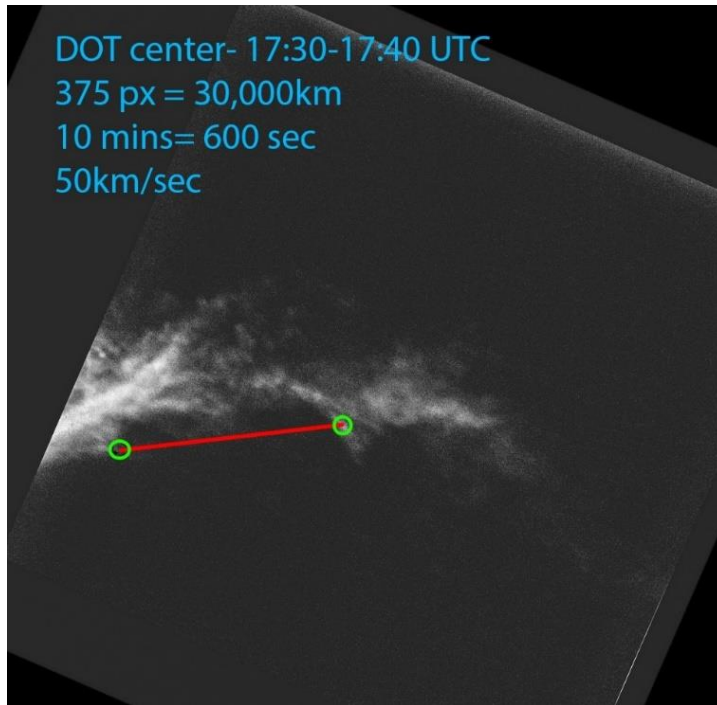


Figure 51: DOT H α speeds: This image shows material moving downward near the end of the observation run, with a speed of ~ 50 km/sec.

Most of the material observed moving out of the pillar area of the prominence is blue shifted. In the 304 \AA images, material can be seen moving away from the pillar and flows towards an active region which is closer to the camera on the disk of the Sun. There is redshifted material but it mostly occurs closer to and inside the pillar where there is counterstreaming. Around 16:06 UT material stops moving outward and begins to move inward towards the pillar. The material appears most dominant in the H α centerline images with about the same motion in the redshift images and blueshift images.

The Shape of SDO's 304 \AA NW Prominence

The northwest prominence in the 304 \AA images looks considerably different than its H α counterpart. The main pillar is clearly seen even though it is surrounded by material interacting with it. Because of the ability to see this surrounding material interact with the

main pillar it is clear what is causing the H α prominence's behavior. In 304Å images, the NE side prominence and the material interacting to the left of the main pillar eventually thins out, although never completely, and near the end of the 4.5 hours of observation the right side builds up in mass and height due to the incoming material from the west prominence which interacts with it. The main pillar appears to have its footpoint just behind the limb of the Sun.

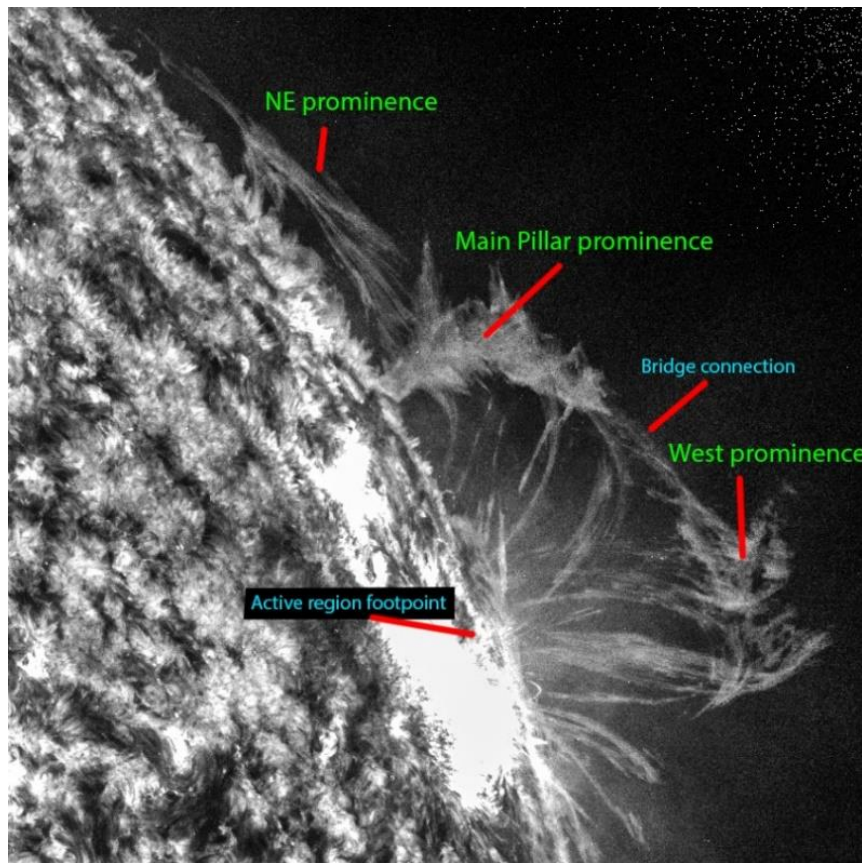


Figure 52: NW prominence in 304Å at 16:42 UT.

There is an indicated footpoint which is located near an active region that interacts with the prominence. Material can be seen moving into a bright region on the disk which appears to be a footpoint as seen in Figure 53. The area of this footpoint is measured to be about 7,400 km wide.

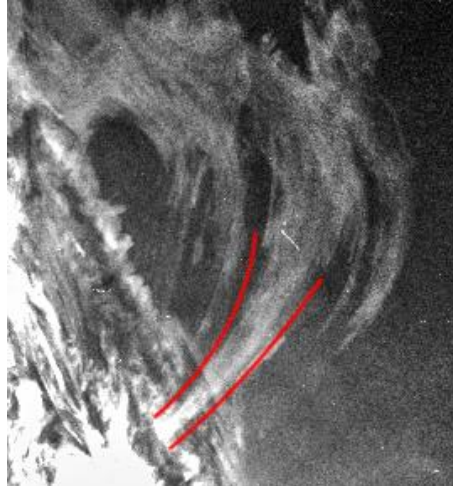


Figure 53: This image shows material moving from the pillar prominence into the chromosphere on the Sun

This footpoint and the active region are on the disk of the Sun and closer to the observer than the pillar; the two footpoints are more than 115,000 km away from each other. This means that any material moving from the pillar to the active region footpoint will flow towards the observer.

Figure 54 shows how the prominence type evolves throughout the observation period. In the left image there are two main paths that the material in the pillar follows; the lower stream in the back with a height of ~40,000 km (purple) and a higher stream (blue) in the foreground which is about 60,000 km high. The blue path shows the prominence pillar with a main stream which reaches a height of ~60,000 km then curves downward and connects to a footpoint next to the active region. It begins as a broken arch with material moving in a curved arching direction to the right but the material is too faint to see where it ends. This process occurs quickly as the material moves rapidly making a connection at 13:31 UT. The yellow path shows the direction material flowing from the NE footpoint, in front of the pillar, and connecting with the active region footpoint. The yellow

path and the blue path appear to be headed into the same footpoint next to the active region. The other main arch, shown as the purple path, coming from the pillar is an arching prominence moving material from the main pillar to behind the limb where it connects with another footpoint. The footpoint is believed to be near an active region because at ~16:00 UT there is an eruption coming from behind the limb where the material from the purple path is flowing toward.

All material observed near the active region is always moving towards the region. There does not seem to be any visible counterstreaming occurring. Material that reaches more than 22,000 km away from the pillar does not appear to have any returning motion. The green path shows material moving between the main pillar and a footpoint 66,000 km away to the NE, which appears to be behind the limb. The green path also has material moving even further NE but at the beginning this part of the prominence is considered a broken arch as there is not enough visible material to see the other footpoint.

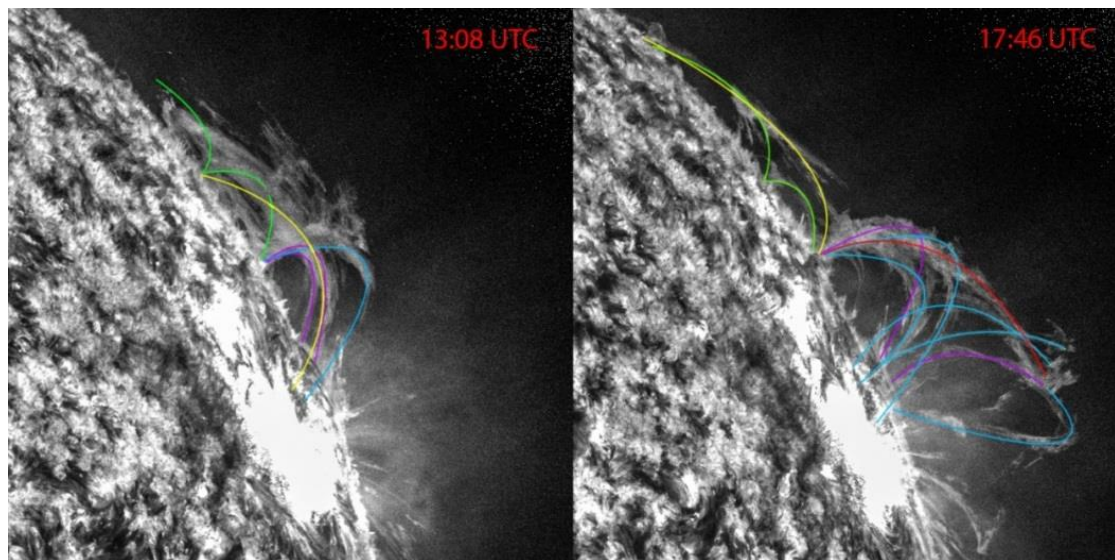


Figure 54: Movement of the NW prominence. a (left) b (right): These images shows how material moves between footpoints, how they interact with each other and how the prominence evolves over time.

The prominence changes its appearance over the four hours of observation. The right image at 17:46 UT shows the NE footpoint moving material to a further NE footpoint which was not previously seen. The yellow path now shows material flowing from the left side of the pillar to a footpoint more than 185,000 km away to the north. Material is still seen moving from the NE footpoint to the active regions footpoint although it is very faint. At 14:22 UT another prominence begins to appear and continues to grow with barbs of material flowing in three different directions; towards the active region, towards the pillar and towards the assumed footpoint behind the limb indicated by the purple line. The red path, or bridge, shows how the pillar exchanges material with the newly formed prominence. There is visible counterstreaming occurring on the bridge when material from the newly formed west prominence and the pillar interact. This new interaction changes how material moves outward from the pillar

Dimensions of SDO's 304Å NW Prominence

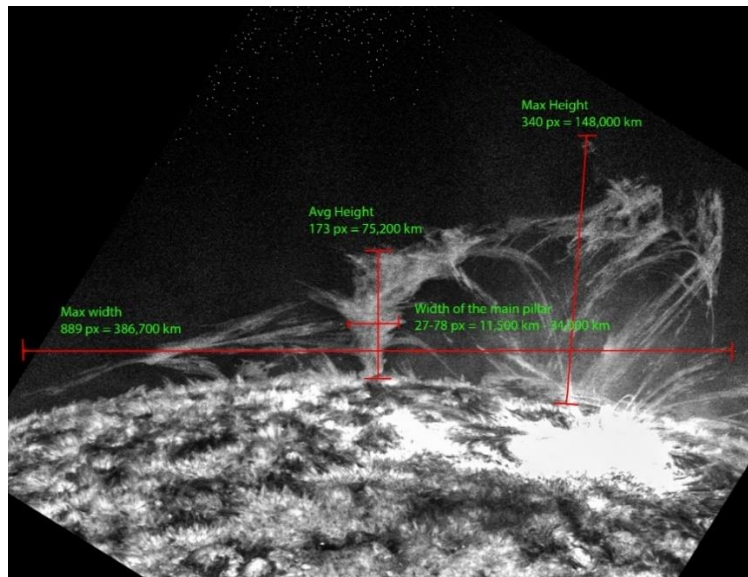


Figure 55: NW prominence dimensions in 304 Å. The dimensions of the NW prominence in 304 Å at the beginning of the observing run at 13:08 UT.

Figure 55 shows the prominence reaching maximum heights observed in $H\alpha$ images, at around 148,000 km. The width of the prominence is difficult to determine in the 304 Å images because it is hard to see where the edges of the pillar are. The width is estimated to be between ~11,500 km up to ~34,000 km. As the prominence evolves and makes new visible connections with other footpoints nearby, the total width measured in the 304 Å images is over 386,700 km.

The material appears to increase in speed as it moves further away from the pillar prominence. In the 304 Å images, the speed near the center of the pillar is difficult to estimate as the material is too dense and it blends too much with the surrounding material. Speeds of up to 55 km/s (Table 1, Speed 9) were observed at higher heights later during the observation run which corresponds with speeds found in the $H\alpha$ images (Table 1, Speed 8), see Figure 56 below.

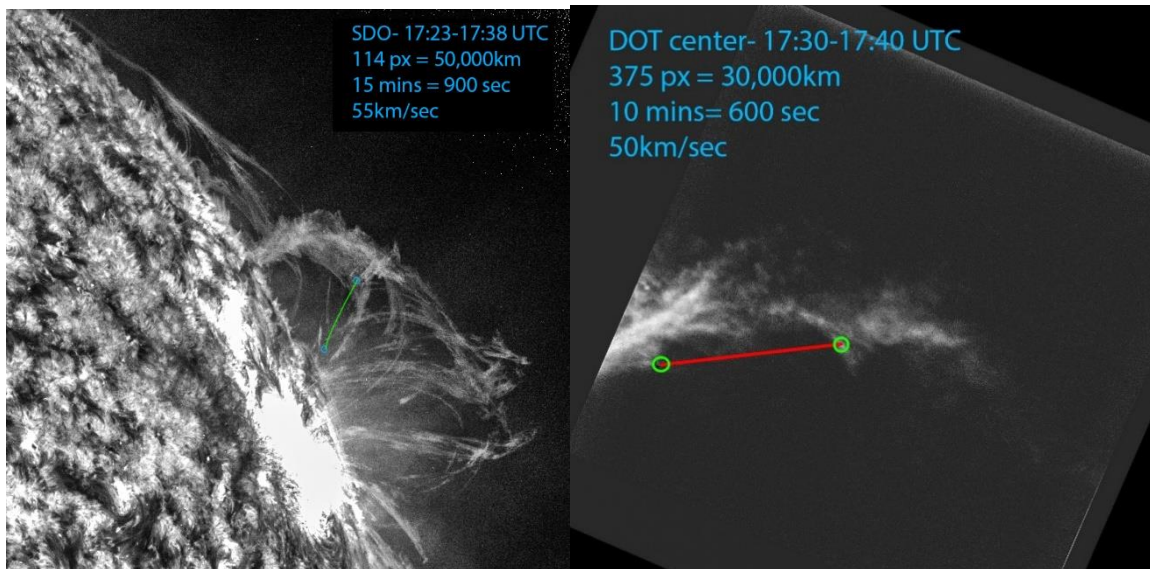


Figure 56: NW prominence speeds. The speeds seen near the end of the observation run are measured from the downward flowing material that originated from new west prominence. The speeds seen in $H\alpha$ and 304 Å are very similar at ~50-55 km/sec.

The Evolution of the NW Prominence

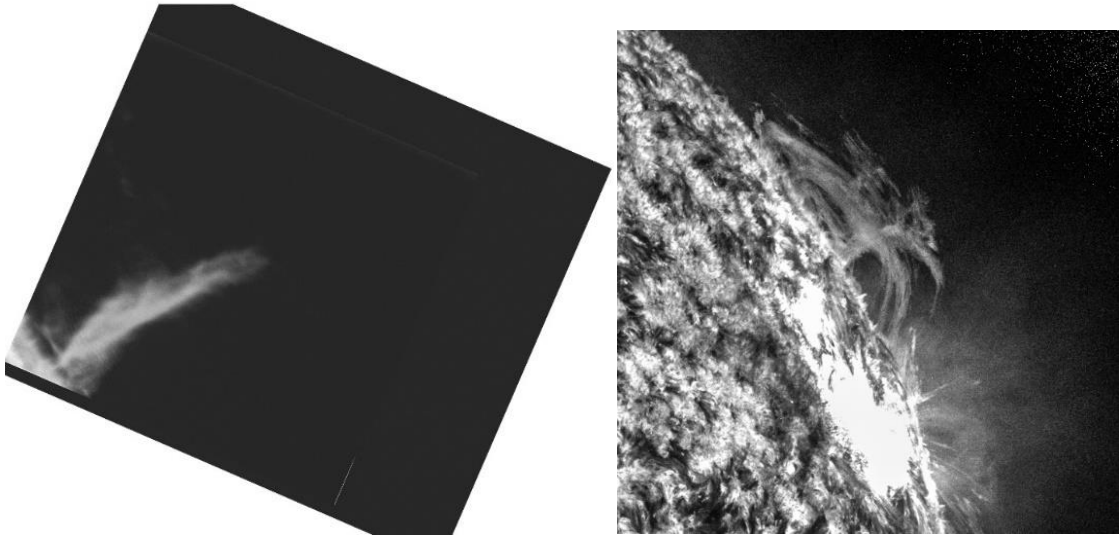


Figure 57: NW prominence at the start. This is the start of the prominence at 13:08 UT in the $H\alpha$ wavelength (left) and the 304\AA wavelength (right)

The prominence begins at 13:08 UT where in $H\alpha$ it appears to be one single pillar in the shape of a broken arch prominence. At 13:26 UT the pillar appears to split at the top in two opposite directions, see Figure 58 below. This split becomes very prominent around 13:54 UT. In 304\AA it is too difficult to see this split in detail because there is material blocking the view, however, it is clear that material is moving to the right and left of the pillar because the material is visible in this wavelength. This material is higher and hotter because it can be seen in 304\AA and it is too faint to be seen in $H\alpha$. There is mass seen moving outwards from the main pillar prominence to the right as well as material is seen moving inwards and outwards to the left of the pillar. Throughout the entire observation run material is observed moving in different directions. Material is seen flowing mostly outwards in the beginning and near the end once the bridge connection is made with the

west prominence it will start to flow inwards. In the 304 Å images this flow of material is seen moving in the same direction.

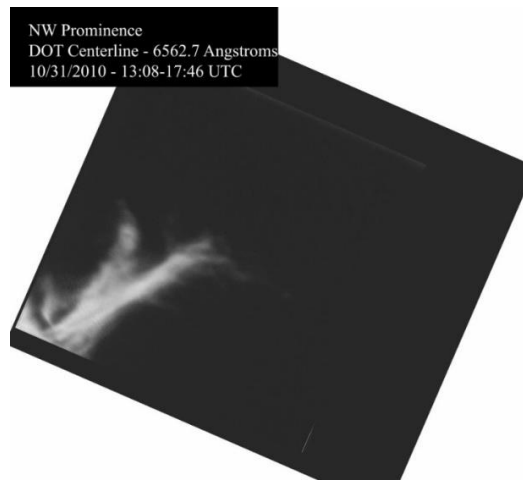


Figure 58: NW prominence H α split. In H α a split is seen at 13:54 UT. This shows that this prominence is interacting with other footpoints in two opposite directions.

At approximately 14:19 UT in the 304 Å wavelength, 135,000 km west of the main pillar and 120,000 km above the surface, a mass begins to appear, see Figure 59. This mass slowly seems to grow in mass throughout the remaining three hours as material appears in the wavelength. The material appears suddenly high up above the solar surface with material flowing downward in five different streams indicating that the material is cooling down. Material appears to have already been moving upwards along the footpoints but it was too hot to be seen 304 Å. Eventually the material gathers together and as it becomes denser it cools down and eventually becomes visible and flows downward towards the surface. The first connection made by the newly formed west prominence with the surface occurs at 15:19 UT and the material is calculated to be moving at ~56 km/s (Table 1, Speed 10) downward. All the other connections that the west prominence develops have similar speeds except for the bridge connection, seen in Figure 62, from the west prominence to

the pillar prominence where the speed is slower at around 27 km/s (Table 1, Speed 11). This decrease in speed is probably due to counterstreaming of mass between the west prominence and the pillar, the collision of material inhibits their speeds.

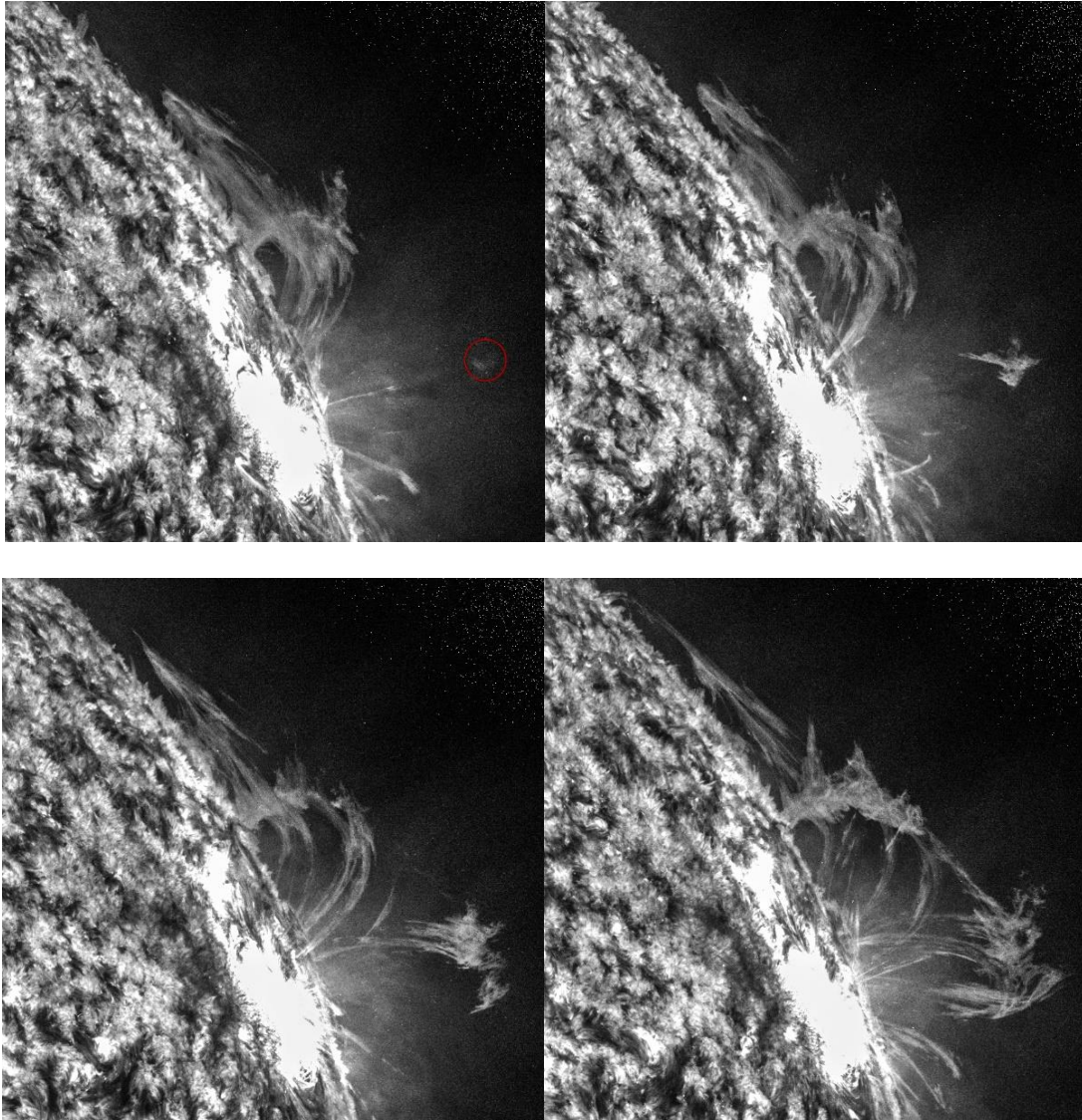


Figure 59: Appearance of the west prominence in the NW. The four images show the evolution of the west prominence which appears at 14:19 UT (top left) circled in red. The top right image shows how a barb from the mass begins to direct itself towards the active region (14:59 UT). The bottom left image shows how a bridge connection begins to faintly form with the pillar prominence as well as with more barbs begin to move toward the surface (15:39 UT). The bottom right image shows the many connections this mass has created as well how much bigger the prominence actually is (16:35 UT).

At about 14:41 UT in the H α images, material is observed in the blue shift moving in an arching downward direction to the right out of frame, seen in Figure 60. There is very faint material seen in the red shift at the same time moving to the right, away from the pillar. This indicates that the movement of mass is toward the camera and this is confirmed by the 304 Å data. Because the pillar's footpoint is behind the limb and the active region footpoint is on the disk closer to the camera, any material that flows from the pillar to the active region needs to move toward the camera. The speeds seen in the blue shift are about 25 km/s (Table 1, Speed 12).

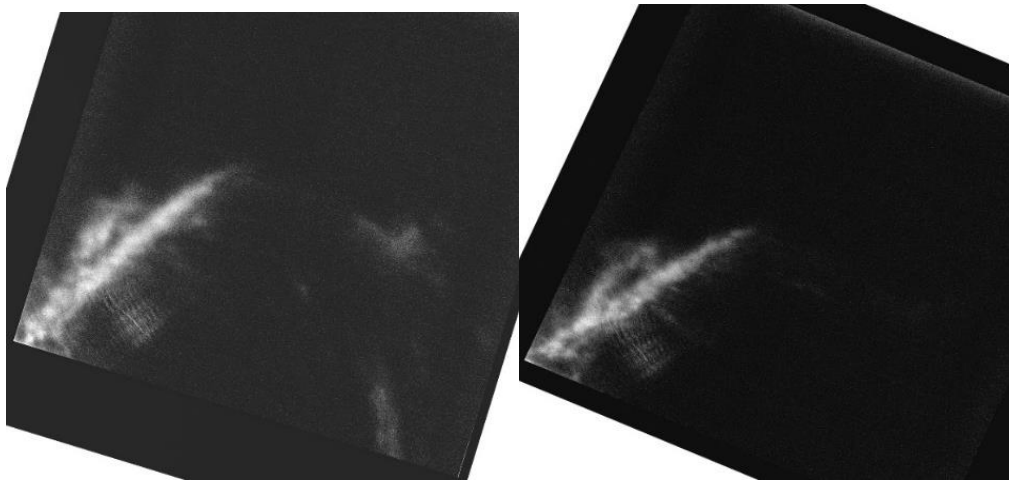


Figure 60: Blue shift moving material in H α . Left image shows H α blue shift (6562.3 Å) at 14:41UT and the right image is the red shift (6563.1 Å) at the same time. Material is seen moving towards the camera and almost none is moving away.

In 304 Å it is difficult to distinguish mass motions in the same area because it is so dense with material. Speeds needed to be calculated closer to the active region where the material was moving to. The speeds of the material moving from the pillar to the active region were calculated to be about 43 km/s (Table 1, Speed 13), see Figure 61. This difference in speed could be explained by the concept that plasma builds momentum the further away from the pillar it gets because there is less material to interfere with it. It could

also be attributed to the fact that the speeds taken in H α are only two dimensional and because the material is moving towards the camera there is a dimension missing. The 304 Å calculations were taken later closer to the active region where it started to head downward into the footpoint.

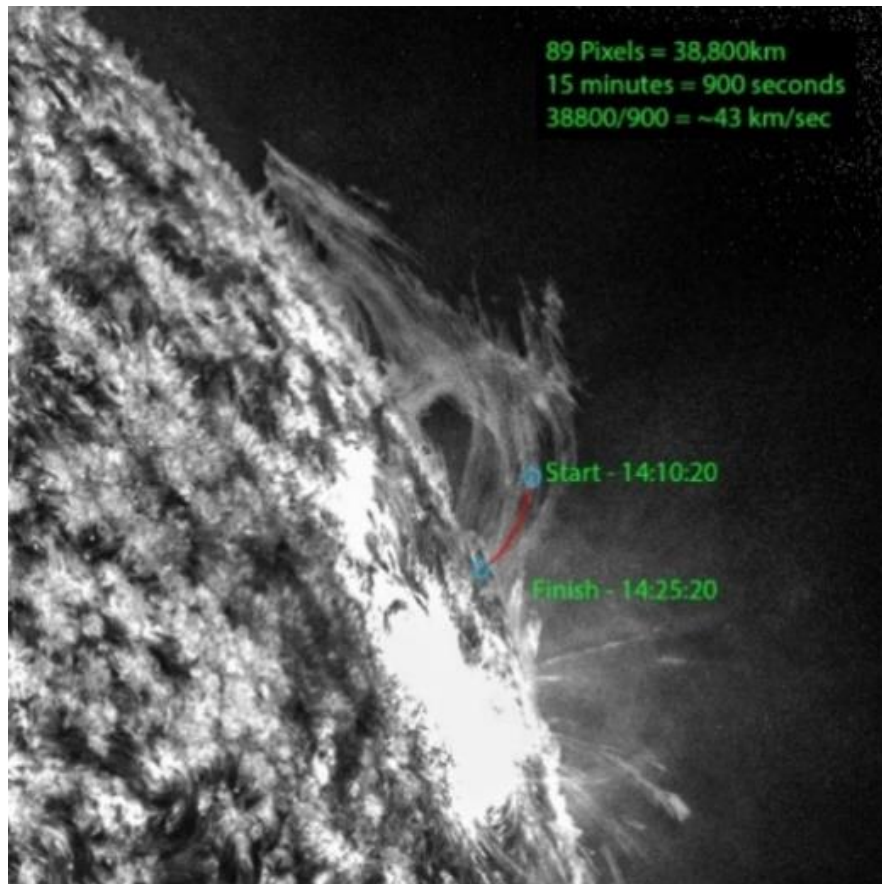


Figure 61: Speeds calculated in 304Å. Speeds calculated of material moving from the main pillar down towards a footpoint next to an active region are about 43 km/sec (Table 1, Speed 13). The material travels 38,800km in 900 seconds.

At 15:52 UT a bridge is formed between the newly formed west prominence and the pillar prominence. The first indication of this interaction with the west prominence and the pillar occurs at 15:36 UT. As seen in Figure 62, there is very bright (hot) material that appears right above the pillar similar to how the west prominence appeared. This is material

which has been moving through the bridge connection before it cooled enough to be seen in 304 \AA . The material moving along the bridge and above the pillar is flowing downwards toward the pillar and interacting with the outward flowing material from the pillar.

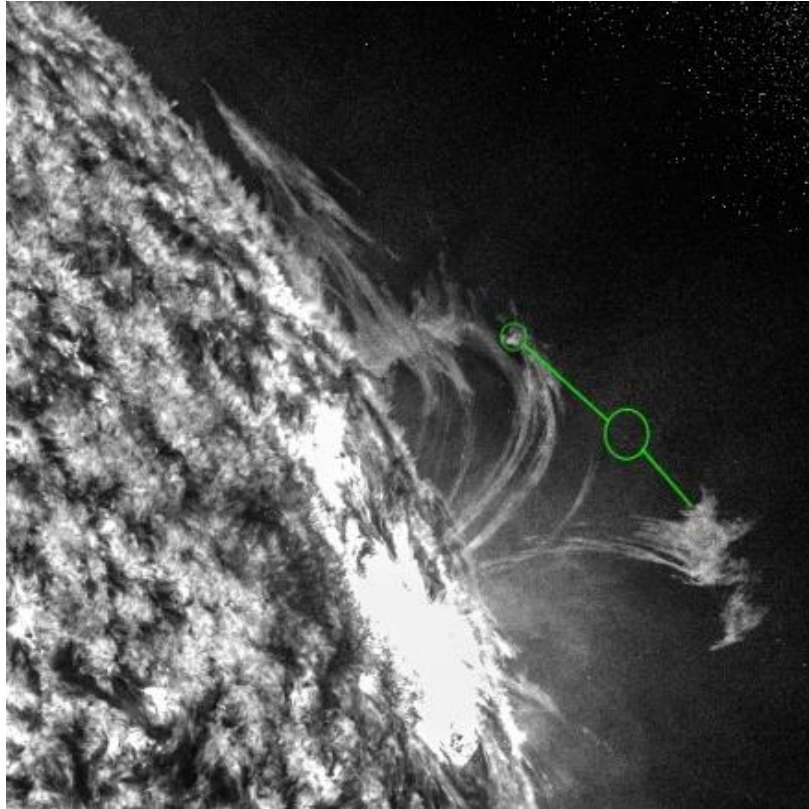


Figure 62: Bridge connection between pillar and west prominence. At 15:36 UT there are very faint signs of a bridge forming. The smaller left circle shows a bright mass appearing at the same time as the bridge. This mass is moving inward toward the pillar interacting with the more dominant right moving material.

In $H\alpha$, up until 15:55 UT all material outside the main structure of the pillar has been mostly moving outward. At 15:55 UT all material to the right of the pillar, in all $H\alpha$ channels, can be seen moving left towards the pillar. In 304 \AA , as seen below in Figure 63, when these two opposite flowing masses interact with each other the main pillar prominence releases material in several perpendicular directions to the prominence. These

ejections begin to occur at 16:10 UT. The speed at which material is moving outward is calculated to be about 31 km/s (Table 1, Speed 14) in the 304Å wavelength.

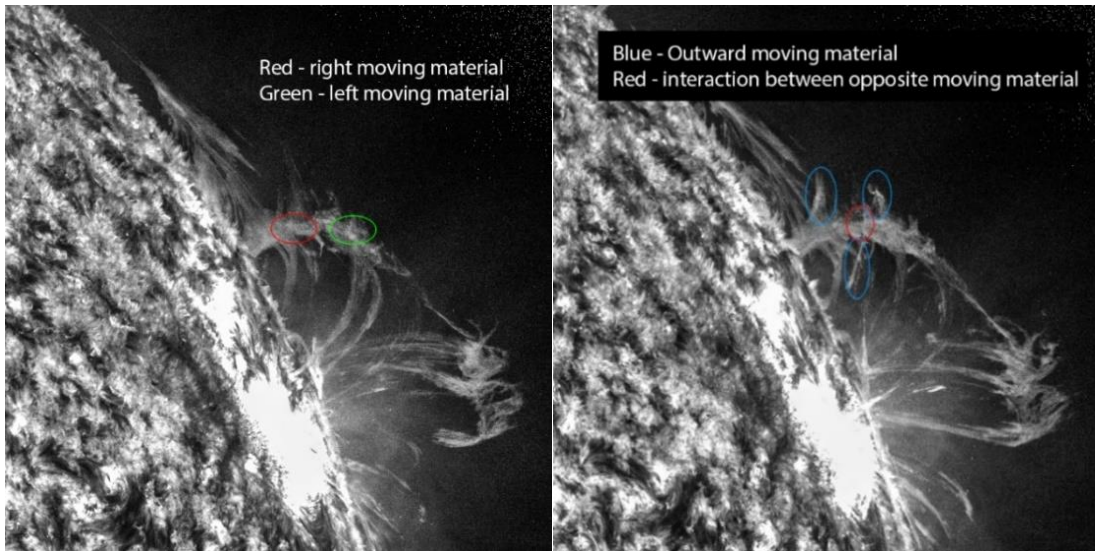


Figure 63: Plasma eruption from flowing collision. The left image taken at 16:03 UT shows that plasma material is flowing in two opposite directions, towards each other. The right image taken at 16:23 UT shows where the plasma interacts with each other shown in the red circle; the material in the blue circles show rapid outward moving material.

This same event observed in 304Å can also be observed in the H α images see Figure 64. The top left image occurs at 16:12 UT and shows material highlighted in a blue circle moving left towards the pillar prominence, circled in red is material from the pillar prominence being ejected outwards to the northeast, as a result. The top right image at 16:17 UT shows the blue circled material moving closer and at this point material inside the red circle breaks off of the pillar and moves outwards. At 16:21 UT the bottom left image shows the red circled material moving outwards from the pillar quickly while the blue circled material continues to flow towards the pillar. At 16:39 UT the bottom right image shows material from the blue circle quickly following the path of the material in the red circle.

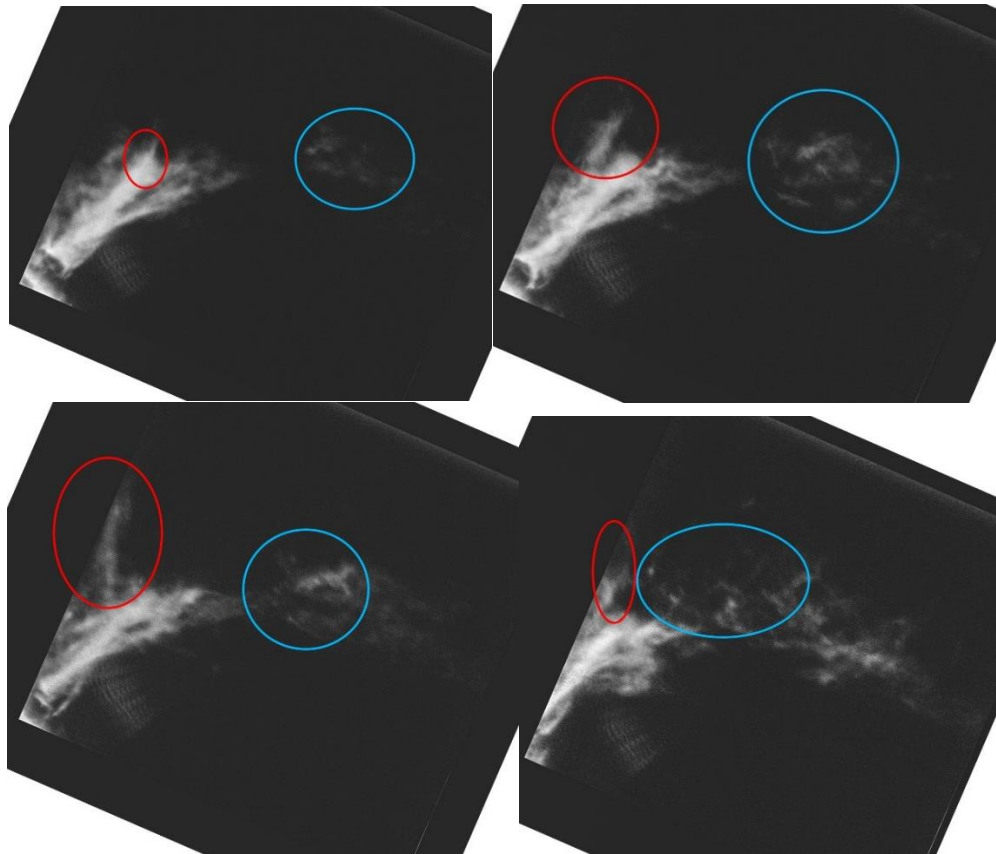


Figure 64: Plasma eruption from flowing collision in H α . These images material circled in red moving outwards as material circled in blue moves inwards.

At 16:12 UT the leftward flowing material from the bridge appears to cut off the main barb of the pillar which was moving material down into the active region footpoints. At 17:10 UT material can be seen moving from the back and underneath the bridge to continue to make its connection with the active region's footpoint, shown in Figure 65 left image. The interaction between opposite moving material appears to stop around 16:56 UT where the outward material being ejected to the left stops and actually begins to flow back in towards the pillar. The material from the bridge is still flowing downward onto the pillar towards its footpoint. As a result of this interaction the pillar appears to rotate clockwise. This appears to occur because the material from the pillar that was pushing outward

continues to flow outward but moves around the outside of the bridge, while the downward moving material from the bridge connection appears to move in front of the pillar. This rotation is seen in the 304 Å wavelength.

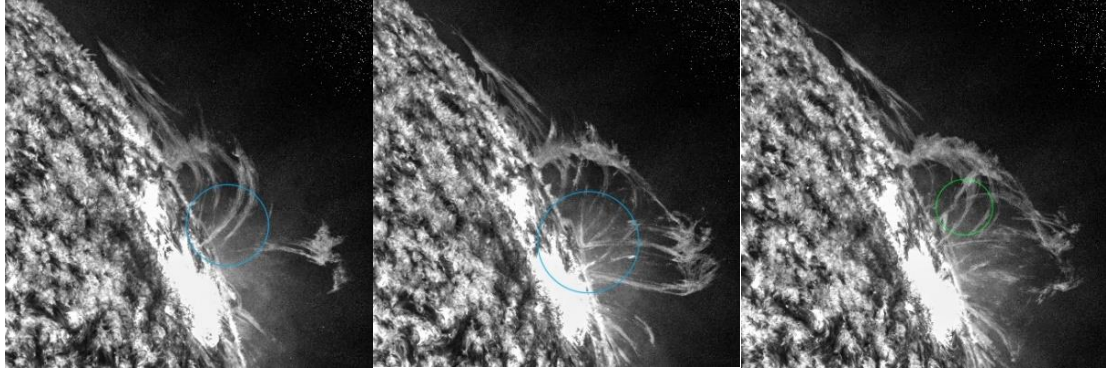


Figure 65: Eruption stops plasma flow to active region. Left image (15:31 UT), inside the blue circle downward moving material is flowing from the pillar to the active region. Center image (16:21 UT) shows the streaming material has stopped. The Right image (17:33 UT) shows new connections created by the outward moving material from the pillar which travels around the back of the bridge (green circle) and under the left moving bridge material.

At 15:59 UT there is an eruption on the far side of the limb. This eruption is believed to be near the footpoint where the streams from the pillar and west prominence had connections to. Due to this eruption, material from the pillar prominence halts its flow of downward moving material toward the active region. Material flowing downward into the active region from the new west prominence however continues to do so without stopping. Figure 66 shows that the velocity of this eruption reaching speeds of ~ 119 km/s (Table 1, Speed 15). The eruption's material appears to be directly headed towards where the west prominence's downward left flowing material interacts with the prominence pillar outward flowing material, all three motions collide at about the same time $\sim 16:20$ UT. It is possible that the ejections shown in Figure 63 and Figure 64 are due to unseen material from the eruption and not the collision of plasma from the pillar and the west prominence. This

scenario seems less likely than the scenario of the two opposite direction moving plasma interacting with each other because some of the material that gets ejected starts to move outwards at 15:58 UT which is right around the time when the eruption starts to be seen above the limb.

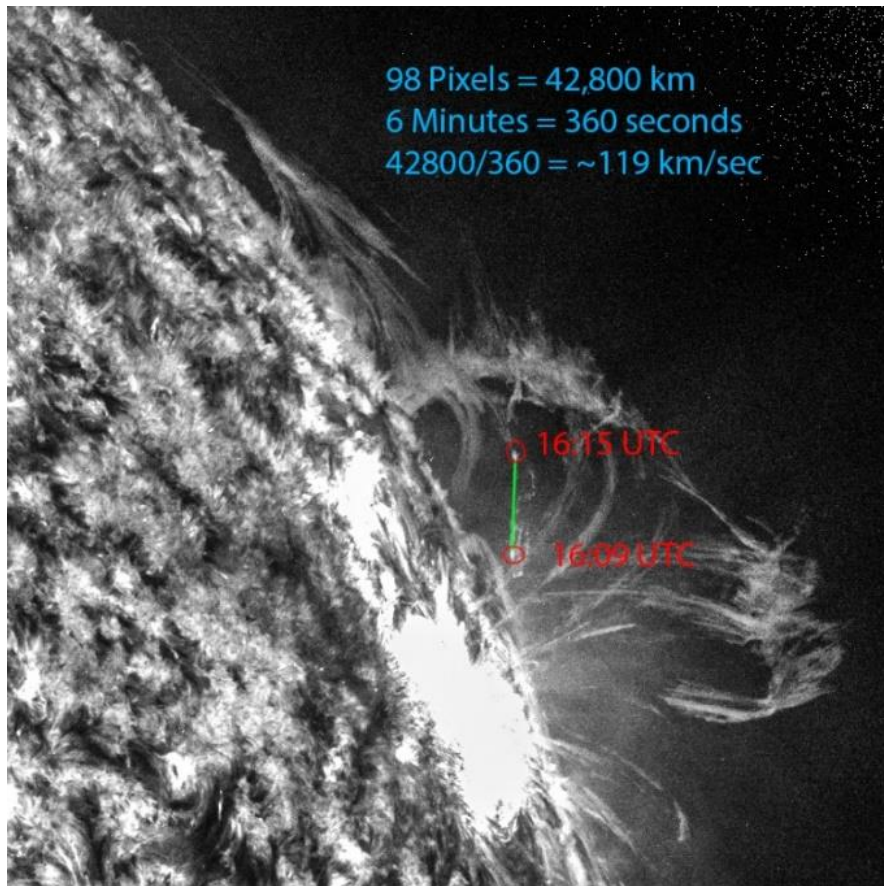


Figure 66: Eruption speeds. The eruption behind the limb creates the fastest speeds observed near this prominence during this timeframe. The material from the eruption moves at about 42,800km in six minutes, this results in a speed of ~119 km/s.

The entire prominence remains in equilibrium at this point until the end of the observation run. However, in the 304 Å images, material flowing downward from the west prominences becomes fainter around 17:33 UT and the steady flow it once had stays sporadic until the last image at 17:46 UT.

Table 1 Velocity Calculations

NE Prom							
DOT	Start	Finish	Time in sec	Distance in Pixels	Distance in km	Speed in km/s	
1 Right prom pg93	120019	120919	540	95	7607.6	14.09	
3 plasma dip event 1 pg 99	120119	120319	120	69	5525.52	46.05	
4 mass of plasma event 2 pg 103	121019	122419	840	225	18018	21.45	
6 event 3 curl pg 104	122019	122919	540	162	12972.96	24.02	
SDO							
DOT	Start	Finish	Time in sec	Distance in Pixels	Distance in km	Speed in km/s	
2 Red line pg99&103	120020	121820	1080	52	22620	20.94	
5 mass of plasma event 2 pg 103	121019	122419	840	37	16095	19.16	
NW Prom							
DOT	Start	Finish	Time in sec	Distance in Pixels	Distance in km	Speed in km/s	
7 average speed in pillar pg107	134315	135615	780	220	17617.6	22.59	
7 average speed in pillar pg108	152621	153521	540	164	13133.12	24.32	
8 incoming pillar speeds pg107&114	173021	174021	600	375	30030	50.05	
12 blue shift from pillar pg 118	143629	144729	660	208	16656.64	25.24	
SDO							
DOT	Start	Finish	Time in sec	Distance in Pixels	Distance in km	Speed in km/s	
9 pillar away material pg 114	172320	173820	900	114	49590	55.10	
10 west prominence pg 116	152320	153620	780	101	43935	56.33	
11 bridge connection speed pg117	155820	161520	720	45	19575	27.19	
13 pillar to the active region pg118/120	141020	142520	900	89	38715	43.02	
14 ejected material pg 122	161020	162320	780	56	24360	31.23	
15 erupted material pg 125	160956	161556	360	98	42630	118.42	

All speeds are about +/- 1km/s. The error bar for calculating the travel path of the mass and its size in the DOT images is within the realm of 6-12 pixels (480-960 km). For SDO it is about 1-2 pixels (435-870km).

CHAPTER IV

DISCUSSION AND CONCLUSION

Classifying prominences

Prominences can be classified into three types according to their locations. Prominences found inside active regions, where there are many bipolar spots, are considered active region prominences. Prominences located at the border of an active region are considered intermediate prominences and prominences on the quiet sun as well as the polar crown are considered quiescent prominences (Su, 2011). The NE prominence seen between 11:49 UT – 12:49 UT is considered a quiescent prominence as it is not near any active regions. Its shape appears to be a hedgerow prominence when viewed in $H\alpha$. This hedgerow prominence can be broken into smaller prominences each with their own shape. The hedgerow shape is not as clearly identified in the 304 Å images as the prominence appears to look more like a mound with no clear shape of the individual prominences which make it up. The only shape identifiable in 304 Å is an arch prominence as depicted in Figure 43. In both wavelengths there appears to be no evidence of a dip in the magnetic field causing material to pool at the apex. There is however a clear dip of material seen in events 1 and 2 in the 304 Å images where masses of plasma flow quickly downwards and slowly upwards indicating a dip in the magnetic field. Because there is no indication of pooling of material or the continuous siphoning of plasma it can be said these are isolated incidents possibly due to the evolution of the magnetic lines which probably

do not reflect on the over configuration of the prominence. Based on the arch prominence in $H\alpha$, as seen outlined by the green line in Figure 40, and the amount of counter-streaming occurring as well as the arch prominence seen in the 304 \AA , outlined in Figure 43, this prominence provides a strong case for the wire model magnetic field line makeup. There are no dips seen anywhere and all material is in constant motion from one footpoint to the other. A twisted flux rope model for this type of prominence seems unlikely as the material does not appear to be rotating and although the right side of the prominence does have a twisting appearance to it, the viewing angle provides insufficient data to draw any conclusions. The right side of the prominence as seen in $H\alpha$ appears to accumulate material though by the evaporation-condensation method as material is seen always flowing downwards. This method does not appear to apply to the single arch prominence on the left and middle side of the prominence. The likely mass accumulation method is through the footpoint injection model. Mass can be seen moving along the top of the prominence and downward towards a footpoint.

The NW prominence observed between 13:08 – 17:49 UT interacts with and is located very close to an active region, because of this it is considered an intermediate prominence. Because of the narrow field of view in the $H\alpha$ images the prominence is only seen to be a broken arch prominence. When viewed in 304 \AA however, the entire prominence can be seen as a single arch prominence. There is another prominence (West prominence) which forms to the west of the main prominence and eventually reconnects with it through a bridge connection as seen in Figure 62. It is unclear whether this connection has always existed, but there was no material moving from the main prominence up through this connection until it was formed by the west prominences

downward moving material. When the west prominence forms it appears high above the surface of the Sun with no indication of material being propelled up through footpoints. The sudden appearance of this material and the constant down flow provides evidence for the evaporation-condensation model. This model suggests that material is heated near the footpoint of a loop which causes plasma to rise to the top of the prominence and as the density increases it cools allowing the material to drain back down to the chromosphere. When the material of the west prominence forms it appears to provide proof of a dip model magnetic field structure. As seen in Figure 67: This image in 304 Å shows the dip seen in the west prominence formation through the coronal condensation mass accumulation method. The material appears to dip down and pool at the top of the magnetic field, eventually material fills the dip and overflows with cool plasma and moves down barbs into the chromosphere.

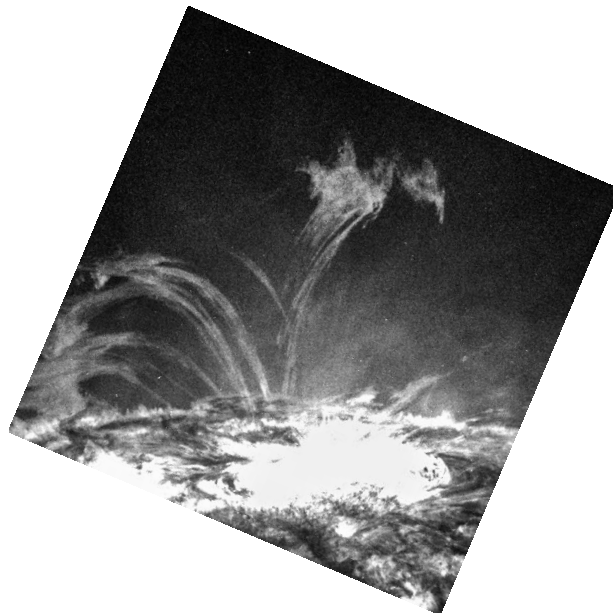


Figure 67: This image in 304 Å shows the dip seen in the west prominence formation through the coronal condensation mass accumulation method.

The dip observed only appears in the west prominence, the rest of the structure including the main arch prominence provides no evidence of a dip model. The main prominence matches a wire model magnetic field structure as it has material moving along its main arch as well as through barbs to minor polarity difference areas. When the bridge is formed between the main prominence and the west prominence there is no evidence of a flux rope model; no dip is formed and material does not appear to rotate. The new arch between the two prominences appears to move in a wire model formation as material continues in a looping flow, counter-streaming occurs, the spine is made from the tops of the arches and barbs come from the spine and extend down towards the surface. However when viewed in H α the main prominence does not appear to resemble the wire model magnetic field structure as there is not a constant looping stream of material. A twisting effect which the material makes once material from the west prominence interacts with the main prominence. This twisting combined with the slow flow of material near the apex could possibly indicate a flux rope model formation, but due to the lack of a large field of view the data is inconclusive.

According to Zirin (1960) prominences can be divided into two kinds: hot and cool. Hot prominences are classified as comprising of flares, surges, loops, and other events related to active regions while cool prominences are classified as quiescent prominences (Zirin, 1960). The **NE** prominence can be classified as cool because it is a quiescent hedgerow prominence not near any active regions. The **NW** prominence however, is considered a hot prominence because it interacts with eruptions, surges and has a footpoint inside of an active region. There is evidence from the observations, that there is a possible

active region on the other side of the limb where another footpoint of this prominence is indicated to be located.

H α vs He II 304 Å

This paper seeks to determine some of the benefits and drawbacks using H α and 304 Å wavelengths to observe prominences on the solar disk. Each wavelength reveals both similar and different prominence morphology and structure at vastly different temperatures. The wavelength 304 Å is used to view prominences at high temperatures where plasma material, mainly He II becomes visible at ~60,000 K, in the upper chromosphere, with a peak of 80,000 K (Waltham, 2012). Images viewed in H α show the cooler lower cores of prominences with temperatures around 6,000 K up to 11,000 K (Wang, 2002).

The northeast prominence is considered a cool prominence and because of this the He II emission line is weaker. Figure 68 shows how the two prominences, the cool NE prominence and the hot northwest prominence, are different in each wavelength. Both prominences show He II surrounding the cool core of the prominence, seen in H α , like a sheath but the size of the sheath is drastically larger in the hot NW prominence than it is in the NE cool one. Material above the main pillar of the NW prominence is barely visible in H α but can be easily seen as a large, dense and bright arch in 304 Å. The 304 Å images show hotter outer material which is very faint or not even seen in H α images. Because the H α line shows strong structure in both cool and hot prominences it can be said that if a prominence is visible in He II is also visible in H α (Wang, 1998).

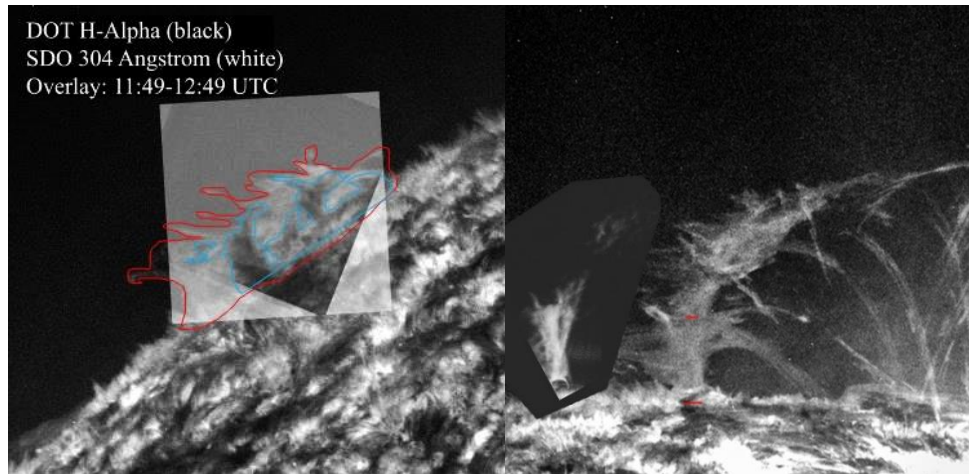


Figure 68: $H\alpha$ vs 304\AA sizes NE & NW. The left image (80a) shows the outlined structure of $H\alpha$ (blue) overlaid onto the He II outlined structure in 304\AA (red). The right (80b) image shows the $H\alpha$ image (left side) next to the 304\AA He II structure (right side).

If there is fast moving material it will be observable in $H\alpha$, but if the material heats up beyond its temperature range from an eruption then that material would just appear to vanish due to Disparition Brusque. Emissions of He II (304\AA) can show areas around the core of a prominence but it is usually difficult to see any type of structure of the core because there is so much material to look through. 304\AA images can see the material in a prominence heat up, rise higher and move faster when $H\alpha$ images cannot because of its narrow emission line. $H\alpha$ images can show much cooler temperatures in a narrow wavelength, there is not as much chromospheric interference at this temperature for the plasma to blend with and therefore plasma structure is easily seen. Figure 69 below shows how prominence structure is different between the two wavelengths. The left image seen in $H\alpha$ shows a very detailed core of the prominence close to the surface. A small arch at the foot of the prominence is clearly seen and the structure is very detailed; in addition, when the frames are played in succession material can be seen counterstreaming. The right image seen in 304\AA shows an outline of the prominence but little detail of its core structure.

The arch seen in $H\alpha$ cannot be seen as it is too low to the surface and when frames are played in succession material appears to be moving only in one direction. Instead, 304 \AA images show the hotter outer regions surrounding the cooler core which is not seen very well in $H\alpha$.

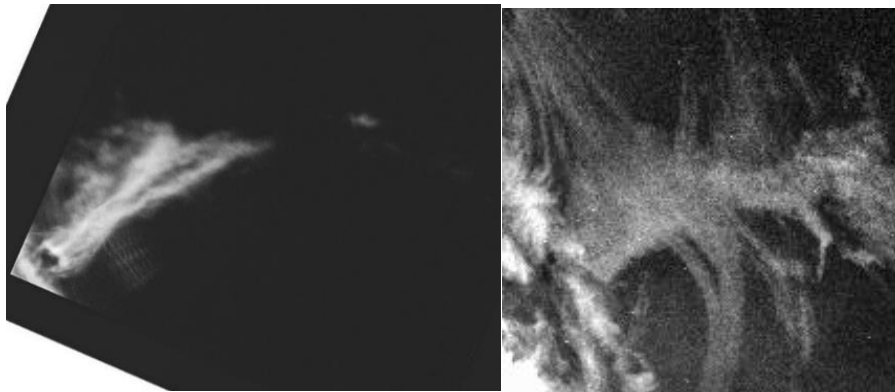


Figure 69: $H\alpha$ vs 304 \AA structure comparison. Left image in $H\alpha$ shows very detailed structure of the prominence's core with an arch at the foot of the pillar. The right image of He II (304 \AA) shows hotter material which can be seen extending its reach further than can be seen in $H\alpha$.

When considering the NE prominence, all events seen in $H\alpha$ were also observed in 304 \AA . This cannot be said the other way around. The prominence extending onto the surface that was seen in 304 \AA could not be identified in $H\alpha$ and the plasma motion seen in the first event that passes back in front of the prominence was not seen either. The heights and widths recorded as well as the speeds observed were all similar and the inconsistencies could have been due to the difference in the viewing angle. The mass flows that were observed in both wavelengths showed similar speeds and distances traveled in both the $H\alpha$ and the 304 \AA Images.

Although the wavelengths seem to show similar morphology in the NE prominence, the NW prominence shows many differences. As the NW prominence becomes more active

the prominence observed in $H\alpha$ does not change much. The heights of the actual prominence and the location and events surrounding this prominence cannot be known just by viewing the $H\alpha$ images. An understanding of what is happening to the prominence only comes from observing the 304 \AA images. The heights and widths measured are drastically different but speeds are quite similar. It is difficult to measure speeds of the main prominence in 304 \AA because of the surrounding material but outgoing and incoming speeds were always similar. The shape of the prominence is different in both wavelengths. In $H\alpha$ it appears to be a broken arch and in 304 \AA it remains a full arch which eventually reconnects into a larger full arch. The appearance and reconnection between the west prominence and the pillar prominence causes material to down flow into the pillar prominence. This is seen in both wavelengths but the material just appears as it draws closer to the surface in the $H\alpha$ images, without viewing the 304 \AA images the source would not have been known. In 304 \AA , once material from the west prominence interacts with material from the main pillar prominence, the outgoing material towards the barbs and foot points is hindered. This is not seen very well in $H\alpha$ as the material only seems to move around the back side of the prominence.

Conclusion

There is a clear benefit to using both filters. The 304 \AA filter is much more flexible in terms of hotter material that appears in the upper chromosphere and the transition region. It is able to see the very fine structure of a prominence at heights where hot material is too faint to be seen in $H\alpha$. The drawback to 304 \AA is the lack of detail able to be captured in the cool cores of prominences as well as seeing anything below the upper chromosphere. Material and mass motions observed in $H\alpha$ has also been identified in 304 \AA . However

material seen moving in 304 Å does not always appear in H α . For example with the NE prominence, material was observed moving to the left in the H α filter but it quickly disappeared due to the increase in temperature. That same event was seen in 304 Å, appearing to move out and come back around and pass in front of the prominence. When this material passed back and in front of the prominence, there was no indication of it at all in the H α images. This could be because the material too hot to be seen in H α or it could have been too far out of the H α band. The resolution of DOT images on a day with good seeing is superior to the resolution of SDO's full disk images even though SDO has no seeing effects. In order to match the resolution of a ground-based telescope, a spacecraft would need a higher resolution telescope which would be larger and cost more to launch.

Speeds calculated for both prominences were very similar in both wavelengths, however heights and widths were very different. The dimensions of the cool NE prominence were relatively the same, but in the NW hot prominence they were drastically different. When modeling the prominences the cool NE one in 304 Å showed very little useful information while in H α it was possible to derive some conclusions. The hot NW prominence however showed, a lot of information about the magnetic field model and mass accumulation. There were some discrepancies between modeling the main pillar prominence in H α and 304 Å, but this could be because of the lack of detail seen in H α . Overall, H α images show the cooler core of a prominence and the fine structure that creates it. Mass motions are also easily identified in H α that would otherwise be difficult to distinguish in 304 Å. On the other hand the 304 Å images show much more detail in the terms of higher hotter material which gives a greater sense to the structure and life of a prominence.

REFERENCES

- Allen, S., & Wells, D. (2005). MIME Sub-type Registrations for Flexible Image Transport System (FITS). FITS Support. Retrieved from <http://fits.gsfc.nasa.gov/>
- Amari, T., Luciani, J., & Linker, J. (1999). Three-dimensional Solutions of Magnetohydrodynamic Equations for Prominence Magnetic Support: Twisted Magnetic Flux Rope. *The Astrophysical Journal*, 518(1), L57-L60.
- Allen, S., & Wells, D. (2005). MIME Sub-type Registrations for Flexible Image Transport System (FITS). FITS Support. Retrieved from <http://fits.gsfc.nasa.gov/>
- Antiochos, S., & Klimchuk, J. (1991). A Model for the formation of solar prominences. *The Astrophysical Journal*, 378, 372-377.
- Antiochos, S. K., MacNeice, P. J., Spicer, D. S., & Klimchuk, J. A. (1999). The Dynamic Formation of Prominence Condensations. *The Astrophysical Journal*, 512, 985-991.
- Antiochos, S. K., MacNeice, P. J., & Spicer, D. S. (2000). The Thermal Nonequilibrium of Prominences. *The Astrophysical Journal*, 536(1), 494-499.
- Aschwanden, M. J. (2006). *Physics of the solar corona an introduction with problems and solutions* (2nd ed.). Berlin: Springer.
- Aulanier, G., Demoulin, P., Mein, N., Driel-Gesztelyi, L. v., Mein, P., & Schmieder, B. (1999). 3-D magnetic configurations supporting prominences. *Astronomy and Astrophysics*, 342, 867-880.

- Aulanier, G., DeVore, C., & Antiochos, S. (2002). Prominence magnetic dips in three-dimensional sheared arcades. *The Astrophysical Journal*, 567, L97-L101.
- Aulanier, G., DeVore, C., & Antiochos, S. (2006). Solar Prominence Merging. *The Astrophysical Journal*, 646, 1349-1357.
- Babcock, H. W. "The Topology of the Sun's Magnetic Field and the 22-YEAR Cycle." *The Astrophysical Journal* 133 (1961): 572. Print.
- Ballegooijen, A. A. Van, and P. C. H. Martens. "Formation and eruption of solar prominences." *The Astrophysical Journal* 343 (1989): 971. Print.
- Ballegooijen, A. A., & Cranmer, S. R. (2010). Tangled Magnetic Fields In Solar Prominences. *The Astrophysical Journal*, 711(1), 164-178.
- Bettonvil, F., Hammerschlag, R., Sutterlin, P., Rutten, R., Jagers, A., & Snik, F. (1999). DOT++: The Dutch Open Telescope with 1.4-m aperture. Astronomical Institute, Utrecht University, 5489.
- Berger, T. E., Suematsu, Y., Hurlburt, N., Slater, G., Shimizu, T., Magara, T., et al. (2010). Quiescent Prominence Dynamics Observed With The Solar Optical Telescope. I. Turbulent Upflow Plumes. *The Astrophysical Journal*, 716(2), 1288-1307.
- Canfield, R., Kazachenko, M., Acton, L., Mackay, D., Son, J., & Freeman, T. (2007). Yohkoh SXT Full-Resolution Observations of Sigmoids: Structure, Formation, and Eruption. *The Astrophysical Journal*, 671, L81-L84.
- Cattaneo, F., Brummell, N. H., & Cline, K. S. (2006). What Is A Flux Tube? On The Magnetic Field Topology of Buoyant Flux Structures. *Monthly Notices of the Royal Astronomical Society*, 365(3), 727-734.

- Chae, J., Ahn, K., Lim, E., Choe, G. S., & Sakurai, T. (2008). Persistent Horizontal Flows and Magnetic Support of Vertical Threads in a Quiescent Prominence. *The Astrophysical Journal*, 689(1), L73-L76.
- Chae, J., Moon, Y., & Park, S. (2003). OBSERVATIONAL TESTS OF CHROMOSPHERIC MAGNETIC. *Journal of the Korean Astronomical Society*, 36, S13-S20.
- Chae, J., Wang, H., Qiu, J., Goode, P., Strous, L., & Yun, H. (2001). The Formation of a Prominence in Active Region NOAA 8668. I. SOHO/MDI Observations of Magnetic Field Evolution. *The Astrophysical Journal*, 560, 476-489.
- Chaisson, E., & McMillan, S. (1993). *Astronomy today*. Englewood Cliffs, NJ: Prentice Hall.
- Demoulin, P., & Priest, E. R. (1989). How to Form a Dip in a Magnetic Field Before the Formation of a Solar Prominence. *Hvar Observatory Bulletin*, 13(1), 261.
- Engvold, O. (1976). The fine structure of prominences. I - Observations - H-alpha filtergrams. *Solar Physics*, 49, 283-295.
- Foukal, P. (1971). H α Fine Structure And The Chromospheric Field. *Solar Physics*, 20(2), 298-309.
- Gaizauskas, V. (1998). Filament Channels: Essential Ingredients for Filament Formation. *New Perspectives on Solar Prominences*, 150, 257.
- Gaizauskas, V., Mackay, D. H., & Harvey, K. L. (2001). Evolution Of Solar Filament Channels Observed During A Major Poleward Surge Of Photospheric Magnetic Flux. *The Astrophysical Journal*, 558(2), 888-902.

- Galsgaard, K., & Longbottom, A. W. (1999). Formation of Solar Prominences by Flux Convergence. *The Astrophysical Journal*, 510, 444-459.
- Galsgaard, K., & Parnell, C. (2004). Fragment Driven Magnetic Reconnection. *Proceedings of the SOHO 15 Workshop*, 575, 351-356.
- Gibson, S. E., Foster, D., Burkepile, J., Toma, G. d., & Stanger, A. (2006). The Calm Before The Storm: The Link Between Quiescent Cavities And Coronal Mass Ejections. *The Astrophysical Journal*, 641(1), 590-605.
- Gibson, S. E., Fan, Y., Török, T., & Kliem, B. (2007). The Evolving Sigmoid: Evidence for Magnetic Flux Ropes in The Corona Before, During, And After CMES. *Space Science Reviews*, 124(1-4), 131-144.
- Gilbert, H. R., Alexander, D., & Liu, R. (2007). Filament Kinking and Its Implications for Eruption and Re-formation. *Solar Physics*, 245(2), 287-309.
- Gilbert, H. R., Hansteen, V. H., & Holzer, T. E. (2002). Neutral Atom Diffusion in a Partially Ionized Prominence Plasma. *The Astrophysical Journal*, 577, 464-474.
- Gosain, S., & Schmieder, B. (2010). Estimation of width and inclination of a filament sheet using He II 304 Å observations by STEREO/EUVI. *Annales Geophysicae*, 28(1), 149-153.
- Heinzl, P., Schmieder, B., & Tziotziou, K. (2001). Why Are Solar Filaments More Extended in Extreme-Ultraviolet Lines than in H α ? *The Astrophysical Journal*, 561(2), L223-L227.
- Helioseismic and Magnetic Imager for SDO. (2010). Stanford Solar Group. Retrieved January 13, 2014, from <http://hmi.stanford.edu/>

- Ignace, R., Nordsieck, K. H., & Cassinelli, J. P. (1997). The Hanle Effect as a Diagnostic of Magnetic Fields in Stellar Envelopes. I. Theoretical Results for Integrated Line Profiles. *The Astrophysical Journal*, 486(1), 550-570.
- Inverarity, G. W., & Priest, E. R. (1999). Magnetic Null Points Due to Multiple Sources of Solar Photospheric Flux. *Solar Physics*, 186, 99-121.
- Joshi, A. D., Srivastava, N., Mathew, S. K., & Martin, S. F. (2013). Rapid Formation and Disappearance of a Filament Barb. *Solar Physics*.
- Karpen, J. T., Antiochos, S. K., Hohensee, M., Klimchuk, J. A., & MacNeice, P. J. (2001). Are Magnetic Dips Necessary for Prominence Formation? *The Astrophysical Journal*, 553(1).
- Khlystova, A. (2013). The Horizontal Component of Photospheric Plasma Flows During the Emergence of Active Regions on the Sun. *Solar Physics*, 284(2), 343-361.
- Kilper, G. K. (2009). *Mass composition and dynamics in quiet sun prominences*. Texas: Proquest Dissertations and Theses.
- Kilper, G., Gilbert, H., & Alexander, D. (2009). Mass Composition in Pre-Eruption Quiet Sun Filaments. *The Astrophysical Journal*, 704(1), 522-530.
- Labrosse, N., Vial, J., & Gouttebroze, P. (2008). Diagnostics of active and eruptive prominences through hydrogen and helium lines modelling. *Annales Geophysicae*, 26(10), 2961-2965.
- Labrosse, N. et al. (2010). Physics of Solar Prominences: I - Spectral Diagnostics and Non-LTE Modeling. *Space Science Reviews*, 151(4), 243-332.

- Lin, Y., Martin, S., & Engvold, O. (2008). Filament Substructures and their Interrelation. *Subsurface and Atmospheric Influences on Solar Activity ASP Conference Series*, 383, 235-242.
- Liu, R., Xu, Y., & Wang, H. (2010). Evolution of Filament Barbs. *Solar and Stellar Astrophysics*, 1-4.
- Lopez, A., Aulanier, G., Schmieder, B., & Dalda, A. (2006). First observation of bald patches in a filament channel and at a barb endpoint. *A&A*, 456(2), 725-735.
- Mackay, D., Gaizauskas, V., Rickard, G. J., & Priest, E. R. (1997). Force-free and Potential Models of a Filament Channel in Which a Filament Forms. *The Astrophysical Journal*, 486, 534-549.
- Mackay, D., Karpen, J., Ballester, J., Schmieder, B., & Aulanier, G. (2010). Physics of Solar Prominences: II - Magnetic Structure and Dynamics. *Space Science Review*, 151, 333-399.
- MacNeice, P., Spicer, D. S., & Antiochos, S. (1999). A Model for Prominence Mass and Dynamics. *8th SOHO Workshop*, 446, 457-459.
- Martens, P., & Zwaan, C. (2001). Origin and Evolution of Filament-Prominence Systems. *The Astrophysical Journal*, 558(2), 872-887.
- Martin, S. (Creator) (2012). Classifying Filaments and Prominences According to Their Dynamics. *Helio Research*. Power Point.
- Marin, S. F. (1990). Conditions for the formation of prominences as inferred from optical observations. *Lecture Notes in Physics*, 363, 1-48.

- Martin, S. F. (1998). Conditions for the Formation and Maintenance of Filaments. *Solar Physics*, 182(1), 107-137.
- Martin, S. F., & Echols, R. (1994). An observational and conceptual model of the magnetic field of a filament. *Solar Surface Magnetism*, 1, 339.
- Martin, S. F., & McAllister, A. (1996). The Skew of X-ray Coronal Loops Overlying H-alpha Filaments. *Magnetodynamic phenomena in the solar atmosphere*, 1, 497.
- Martin, S. F., Panasenco, O., Engvold, O., & Lin, Y. (2008). The Link between CMEs, Filaments and Filament Channels. *Annales Geophysicae*, 26(10), 3061-3066.
- Martin, S., Panasenco, O., Berger, M., Engvold, O., Lin, Y., Pevtsov, A., et al. (2012). The Build-up to Eruptive Solar Events Viewed as the Development of Chiral Systems. *ASP Conference Series*, 463.
- National Aeronautics and Space Administration. (n.d.). National Space Science Data Center. Retrieved November 1, 2013, from <http://nssdc.gsfc.nasa.gov/>
- Pesnell, W. D., Thompson, B. J., & Chamberlin, P. C. (2012). The Solar Dynamics Observatory (SDO). *Solar Physics*, 275(1-2), 3-15.
- Pevtsov, A. (2002). Sinuous Coronal Loops at the Sun. *Elsevier science, COSPAR*, 125.
- Pevtsov, A., Balasubramaniam, K., & Rogers, J. (2003). Chirality of Chromospheric Filaments. *The Astrophysical Journal*, 595, 500-505.
- Pevtsov, A., Canfield, R. C., & Metcalf, T. R. (1995). Latitudinal Variation of Helicity of Photospheric Magnetic Fields. *The Astrophysical Journal*, 440, L109.

- Pevtsov, A., Canfield, R. C., Sakurai, T., & Hagino, M. (2008). On The Solar Cycle Variation of the Hemispheric Helicity Rule. *The Astrophysical Journal*, 677(1), 719-722.
- Poland, A. I., & Mariska, J. T. (1986). A Siphon Mechanism for Supplying Prominence Mass. *Solar Physics*, 104(2), 303-312.
- Priest, E. R., & Forbes, T. (2000). *Eric Priest, Terry Forbes, Magnetic Reconnection*. Cambridge: Cambridge University Press
- Priest, E. R., & Smith, E. A. (1979). The structure of coronal arcades and the formation of solar prominences. *Solar Physics*, 64, 267-286.
- Priest, E. R., & Schrijver, C. J. (1999). Aspects of Three-dimensional Magnetic Reconnection. *Solar Physics*, 190, 1-24.
- Rust, D. M., & Kumar, A. (1994). Helical Magnetic Fields in Filaments. *Solar Physics*, 155(1), 69-97.
- Rust, D. M., & Kumar, A. (1996). Evidence for Helically Kinked Magnetic Flux Ropes in Solar Eruptions. *The Astrophysical Journal*, 464, L199-L202.
- Rutten, R., Hammerschlag, R., Sutterlin, P., Bettonvil, F., & Wijn, A. d. (2001). Dutch Open Telescope & Virtual Solar Observatory. Sterrekundig Institute Utrecht.
- Rutten, R., Bettonvil, F., Hammerschlag, R., Jägers, A. P., Leenaarts, J., Snik, F., et al. (2004). The Dutch Open Telescope on La Palma. Proceedings of the International Astronomical Union, 2004(IAUS223).
- Rutten, R. (2012). Dutch Open Telescope. DOT home page. Retrieved January 13, 2014, from <http://www.staff.science.uu.nl/~rutte101/dot/>

- Saito, K., & Tandberg-Hanssen, E. (1973). The arch systems, cavities and prominences in the helmet streamer observed at the solar eclipse, November 12, 1966. *Solar Physics*, 31(1), 105-121.
- Schindler, K., & Hornig, G. (2001). Magnetic reconnection. Encyclopedia of astronomy and astrophysics. ed. / Paul Murdin. Bristol; London: Institute of Physics Publishing; Nature Publishing Group, 1517-1524.
- Schmieder, B., & Aulanier, G. (2012). New perspectives on solar prominences. EAS Publications Series, 55, 149-161.
- Schmieder, B., & Pariat, E. (2007). Magnetic Flux Emergence. (2007), Scholarpedia, 2(12):4335.
- Schmieder, B., Aulanier, G., Mein, P., & Ariste, A. (2006). Evolving Photospheric Flux Concentrations and Filament Dynamic Changes. *Solar Physics*, 238, 245-259.
- Sheeley, N. R., Hoover, R. B., Brueckner, G. E., Bohlin, J. D., Guire, J. P., Loach, A. C., et al. (1975). Coronal Changes Associated With A Disappearing Filament. *Solar Physics*, 45(2), 377-392.
- Solar Dynamics Observatory. (n.d.). NASA. Retrieved January 13, 2014, from <http://sdo.gsfc.nasa.gov/>
- Solar Physics. (n.d.). NASA/Marshall Solar Physics. Retrieved August 20, 2013, from <http://solarscience.msfc.nasa.gov/>
- Sterling, A. C., Moore, R. L., & Thompson, B. J. (2001). EIT and SXT Observations of a Quiet-Region Filament Ejection: First Eruption, Then Reconnection. *The Astrophysical Journal*, 561, L219-L222.

- Su, Y., Ballegoijen, A., & Golub, L. (2010). Structure and Dynamics of Quiescent Filament Channels Observed by Hinode/XRT and STEREO/EUVI. *The Astrophysical Journal*, 721(1), 901-910.
- Su, Y., Surges, V., Ballegoijen, A. V., Deluca, E., & Golub, L. (2011). Observations And Magnetic Field Modeling of the Flare/coronal Mass Ejection Event On 2010 April 8. *The Astrophysical Journal*, 734(1), 53.
- Tandberg-Hanssen, E. (1974). Solar prominences. *Geophysics and Astrophysics Monographs*, 12, 169.
- Tandberg-Hanssen, E. (1995). *The nature of solar prominences*. Dordrecht: Kluwer.
- Tandberg-Hanssen, E. (1998). The History of Solar Prominence Research: Historical Introduction to IAU Colloquium No. 167 "New Perspectives on Solar Prominences". *New Perspectives on Solar Prominences*, 150, 11-21.
- Tandberg-Hanssen, E. (2011). Solar Prominences - An Intriguing Phenomenon. *Solar Physics*, 269, 237-251.
- Van Ballegoijen, A., Cartledge, N., & Priest, E. (1998). Magnetic Flux Transport and the Formation of Filament Channels on the Sun. *The Astrophysical Journal*, 501, 866-881.
- Van Ballegoijen, A., & Martens, P. C. (1989). Formation and eruption of solar prominences. *The Astrophysical Journal*, 343, 971-984.
- Van Hoven, G. V., Mok, Y., & Drake, J. F. (1992). Prominence condensation and magnetic levitation in a coronal loop. *Solar Physics*, 140(2), 269-287.

- Vernin, J., & Munoz-Tunon, C. (1992). Optical Seeing at La Palma Observatory. *Astronomy and Astrophysics*, 257, 811-816.
- Wade, G. (2004). Stellar magnetic fields: the view from the ground and from space. *Proceedings of the International Astronomical Union, 2004(IAUS224)*, 235-243.
- Waltham, N., Podgorski, W. A., Bush, R. I., Scherrer, P. H., Gummin, M. A., Lang, J., et al. (2012). The Atmospheric Imaging Assembly (AIA) on the Solar Dynamics Observatory (SDO). *Solar Physics*, 275(1-2), 17-40.
- Wang, H., Chae, J., Gurman, J., & Kucera, T. (1998). Comparison of Prominences in Ha and He II 304 Å. *Solar Physics*, 183, 91-96.
- Wang, H. (2002). Solar-terrestrial magnetic activity and space environment proceedings of the COSPAR Colloquium on Solar-Terrestrial Magnetic Activity and Space Environment (STMASE), held in the NAOC in Beijing, China, September 10-12, 2001. Amsterdam: Pergamon.
- Wang, Y., & Muglach, K. (2007). On the Formation of Filament Channels. *The Astrophysical Journal*, 666, 1284-1295.
- Wang, Y., Muglach, K., & Kliem, B. (2009). Endpoint Brightenings in Erupting Filaments. *The Astrophysical Journal*, 699(1), 133-142.
- Welsch, B. T. (2006). Magnetic Flux Cancellation and Coronal Magnetic Energy. *The Astrophysical Journal*, 638(2), 1101-1109.
- Williams, D. R., Baker, D., & Driel-Gesztelyi, L. V. (2013). Mass Estimates of Rapidly Moving Prominence Material from High-Cadence EUV Images. *The Astrophysical Journal*, 764(2), 165.

- Xia, C., Chen, P. F., & Keppens, R. (2012). Simulations of Prominence Formation in the Magnetized Solar Corona by Chromospheric Heating. *The Astrophysical Journal Letters*, 748(L26), 1-16.
- Zirker, J. B., Engvold, O., & Martin, S. F. (1998). Counter-streaming gas flows in solar prominences as evidence for vertical magnetic fields. *Nature*, 396(6710), 440-441.
- Zwaan, C. (1987). Elements and patterns in the solar magnetic field. *Annual Review of Astronomy and Astrophysics*, 25, 83-111.
- Zirin, H., & Tandberg-Hanssen, E. (1960). Physical Conditions in Limb Flares and Active Prominences.IV. Comparison of Active and Quiescent Prominences. *The Astrophysical Journal*, 131, 717.
- Zirin, H. (1988). *Astrophysics of the sun*. Cambridge shire: Cambridge University Press.
- Zwaan, C. (1985). The emergence of magnetic flux. *Solar Physics*, 100, 397-414.